2017

Designing Plasmonic Materials And Optical Metasurfaces For Light Manipulation And Optical Sensing

Wenxiang Chen
University of Pennsylvania, xiang3509@gmail.com

Designing Plasmonic Materials And Optical Metasurfaces For Light Manipulation And Optical Sensing

Abstract
Metamaterials are artificial materials designed to create optical properties that do not exist in nature. They are assemblies of subwavelength structures that are tailored in size, shape, composition, and orientation to realize the desired property. Metamaterials are promising for applications in diverse areas: optical filters, lenses, holography, sensors, photodetectors, photovoltaics, photocatalysts, medical devices, and many more, because of their excellent abilities in bending, absorbing, enhancing and blocking light. However, the practical use of metamaterials is challenged by the lack of plasmonic materials with proper permittivity for different applications and the slow and expensive fabrication methods available to pattern sub-wavelength structures. We have also only touched the surface in exploring the innovative uses of metamaterials to solve world problems.

In this thesis, we study the fundamental optical properties of metamaterial building blocks by designing material permittivity. We continuously tune the interparticle distance in colloidal Au nanocrystal (NC) solids via the partial ligand exchange process. Then we combine top-down nanoimprint lithography with bottom-up assembly of colloidal NCs to develop a large-area, low-cost fabrication method for subwavelength nanostructures. Via this method, we fabricate and characterize nano-antenna arrays of different sizes and demonstrate metasurface quarter wave-plates of different bandwidth, and compare their performances with simulation results.

We also integrate the metasurfaces with chemically- and mechanically-responsive polymers for strong-signal sensing. In the first design, we combine ultrathin plasmonic nanorods with hydrogel to fabricate optical moisture sensors for agricultural use. In the second application, we design mechanically tunable Au grating resonances on a polydimethylsiloxane (PDMS) substrate. The dimensions of Au grating are carefully engineered to achieve a hybridized, ultrasharp, and ultrasensitive resonance peak.

Degree Type
Dissertation

Degree Name
Doctor of Philosophy (PhD)

Graduate Group
Electrical & Systems Engineering

First Advisor
Cherie R. Kagan

Keywords
Metasurface, Nanocrsytal, PDMS, Plasmonics, Sensor

DESIGNING PLASMONIC MATERIALS AND OPTICAL METASURFACES FOR LIGHT MANIPULATION AND OPTICAL SENSING

Wenxiang Chen

A DISSERTATION

in

Electrical and Systems Engineering

Presented to the Faculties of the University of Pennsylvania

in

Partial Fulfillment of the Requirements for the

Degree of Doctor of Philosophy

2017

Supervisor of Dissertation

_____

Cherie R. Kagan

Stephen J. Angello Professor, Electrical and Systems Engineering

Graduate Group Chairperson

_____

Alejandro Ribeiro, Associate Professor, Electrical and Systems Engineering

Dissertation Committee

Dr. Nader Engheta, H. Nedwill Ramsey Professor, Electrical and Systems Engineering

Dr. Shu Yang, Professor, Materials Science and Engineering

Dr. Lee Bassett, Assistant Professor, Electrical and Systems Engineering

DESIGNING PLASMONIC MATERIALS AND OPTICAL METASURFACES FOR LIGHT MANIPULATION AND OPTICAL SENSING

COPYRIGHT

2017

Wenxiang Chen

To My Parents, for Their Love and Support

ACKNOWLEDGMENT

First of all, I would like to express my deepest gratitude to my advisor, Prof. Cherie R. Kagan. She gave me the valuable chance to come overseas to one of the most prestigious schools for study. I am particularly impressed by her creative and extensive thinking and her dedication and patience to helping students, which have been an important source of inspiration and encouragement for me to go through the PhD program. The kind, friendly and communicative academic atmosphere in her lab is extremely impressive and has been a great help for me to fit in the research community. Without her tremendous support, it would not be possible for me to finish this dissertation.

I am also extremely grateful to the Office of Naval Research Multidisciplinary University Research Initiative Award No. ONR-N00014-10-1-0942 and the National Science Foundation Civil, Mechanical and Manufacturing Division Award No. CMMI-1562884 for providing funding to support my Ph.D. study.

I am grateful for Prof. Christopher B. Murray, Prof. Andrea Alù, Prof. Shu Yang, Prof. Nader Engheta, Prof. Jay Kikkawa and Prof. Lee Bassett for their advices and great collaboration work. I would like to say thank you to Dr. Mingliang Zhang, Dr. David Kim, and Nicholas Greybush for providing insightful advices for my research and work. I'd like to thank my previous and current group members: Dr. Soong Ju Oh, Dr. Sung Hoon Hong, Dr. Aaron Fafarman, Dr. Guozhong Xing, Dr. Yuming Lai, Dr. Wenting Li, Dr. Marjan Saboktakin, Dr. Ed Goodwin, Dr. Pil Sung Jo, Eric Wong, Nathaniel Berry, Scott Stinner, Daniel Straus, Tianshuo Zhao, Jiacen Guo, Qinghua Zhao, Steven Neuhaus, Austin Keller, Prashanth Gopalan, Diya Li, Naixin Song, Jordan Howard-Jennings, Yao Yu, Xu He, Jingsong Meng, Fengkai Wu, Derrick Butler, Guannan Liu, Vishal Venkatesh, Carl Hart de Ruijter, Elizabeth Dresselhaus, Francisco Lee, Devika Mehta, Kevin Fritz, Emily Gurniak, William Cheng, and also Murray group members: Dr. Xingchen Ye, Dr. Jun Chen, Dr. Taejong Paik, Dr. Ashley Gaulding, Dr. Ben Diroll, Dr. Vicky Doan-Nguyen, Dr. Haoran Yang, Dr. Sen Zhang, Yaoting Wu. It is fun and pleasure to talk and work with you in the past six years.

Last, I want to thank my dad Kun, and my mom Fengping, for their love and support. They are always there for me whenever or wherever I needed help.

Thank you.

ABSTRACT

DESIGNING PLASMONIC MATERIALS AND OPTICAL METASURFACES FOR LIGHT MANIPULATION AND OPTICAL SENSING

Wenxiang Chen

Prof. Cherie R. Kagan

Metamaterials are artificial materials designed to create optical properties that do not exist in nature. They are assemblies of subwavelength structures that are tailored in size, shape, composition, and orientation to realize the desired property. Metamaterials are promising for applications in diverse areas: optical filters, lenses, holography, sensors, photodetectors, photovoltaics, photocatalysts, medical devices, and many more, because of their excellent abilities in bending, absorbing, enhancing and blocking light. However, the practical use of metamaterials is challenged by the lack of plasmonic materials with proper permittivity for different applications and the slow and expensive fabrication methods available to pattern sub-wavelength structures. We have also only touched the surface in exploring the innovative uses of metamaterials to solve world problems.

In this thesis, we study the fundamental optical properties of metamaterial building blocks by designing material permittivity. We continuously tune the interparticle distance in colloidal Au nanocrystal (NC) solids via the partial ligand exchange process. Then we combine top-down nanoimprint lithography with bottom-up assembly of colloidal NCs to develop a large-area, low-cost fabrication method for subwavelength nanostructures. Via this method, we fabricate and characterize nano-antenna arrays of different sizes and demonstrate metasurface quarter wave-plates of different bandwidth, and compare their performances with simulation results.

We also integrate the metasurfaces with chemically- and mechanically-responsive polymers for strong-signal sensing. In the first design, we combine ultrathin plasmonic nanorods with hydrogel to fabricate optical moisture sensors for agricultural use. In the second application, we design mechanically tunable Au grating resonances on a polydimethylsiloxane (PDMS)

substrate. The dimensions of Au grating are carefully engineered to achieve a hybridized, ultrasharp, and ultrasensitive resonance peak.

TABLE OF CONTENTS

LIST OF TABLES

LIST OF ILLUSTRATIONS

[Reprinted with permission from: *Nano Lett.* **2013**, *13*, 350–357. Copyright {2013} American Chemical Society.]

Figure 2-2 Partial ligand exchange process for colloidal Au NC thin films with SCN ligands. (a) Colloidal Au NC thin films are dipped in 0.01 mg/mL solutions of SCN in acetone for different times ranging from 1 min to 3 min. (b) The percentage of OLA ligands that have been exchanged by SCN ligands is determined by integrating the C-H stretching region (2700 cm^{-1} to 3120 cm^{-1}) in the baseline corrected FTIR spectra before (I_1) and after (I_2) ligand exchange. The percentage of OLA ligands after ligand exchange is defined by $x = I_1/I_2 \times 100(\%)$.

Figure 2-3 The remaining percentage of OLA ligand in Au NC solids as a function of reaction time for the partial ligand exchange process.

Figure 2-4 Transmittance spectra of the partially exchanged colloidal Au NC thin films with x percentage of OLA ligands left.

Figure 2-5 Permittivity of the partially ligand-exchanged colloidal Au NC thin films measured by ellipsometry.

Figure 2-6 SEM images of the colloidal Au nanorods.

Figure 2-7 Partially ligand-exchanged colloidal Au NC nanorods. The partial ligand exchange process is carried out in 0.001 mg/mL SCN in the acetone solution for various time from 2 min to 5 min 30 s.

Figure 2-8 Simulation results for the transmittance (a) and absorption (b) of the bulk Au nanorods and fully ligand-exchanged colloidal Au NC nanorods. The dimensions of the Au nanorod array in the simulation are 1000 nm in length, 250 nm in width and 2500 nm in pitch.

Figure 3-1 SEM image of a representative master template. The nanorods in the template have a length of 816 nm and a width of 242 nm.

cut analysis used to characterize hydrogel thin films with (b, c) 0.64 ± 0.03 μm and (d, e) 2.44 ± 0.02 μm thickness coated on top of a Au NR array.

Figure 4-3 Experimental setup used to characterize the optical response of hydrogel-covered Au NR moisture sensors. The hydrogel-covered Au NR array moisture sensor, a commercial humidity sensor and reservoirs of water are enclosed in a 2.5 L glass chamber. RH in the chamber is adjusted by changing the volume of the water reservoirs.

Figure 4-4 Fourier transform infrared (FTIR) spectroscopy measurements for the hydrogel-covered Au NR array moisture sensor as it dries in air held at a RH = 3% and T = 23 ^{o}C after soaking in water (pH = 6). Time is measured from the moment the sensor is taken out of water.

Figure 4-5 Response dynamics of the hydrogel-covered Au NR optical moisture sensor. (a) Wavelength of the localized surface plasmon resonance and integrated intensity of the water stretch region (2530 cm^{-1} - 3845 cm^{-1}) in FTIR spectra from the hydrogel-covered Au NR optical moisture sensor, as it dries over time from the fully soaked in water (pH = 6) to RH = 3%, T = 23 ^{o}C. (b) Sensor resonance position as a function of drying time from fully soaked in water (PH = 6) to steady state in 30%, 47%, 74% and 80% RH air. (c) Steady state sensor resonance positions in different static RH environments. (d) [top] Sensor recovery time extracted from resonance position curves in (b); [bottom] and the recovery time from fully soaked to 30% RH for sensors with different thickness hydrogel films. (e) Resonance position curves in (b) are converted to concentration of water (dotted lines) based on the calibration curve in (c) and Equation (4). Time-dependent concentration curves are fit to Equation (5) (solid lines). (f) Sensor resonance position for three cycles of soaking in water (pH = 6) and drying in 30% RH measured on three different calendar days.

Figure 4-6 Enlargement of the short time rise of the resonance curves in Figure 4-5 (b), as the sensor dries in air of different RH after soaking in water (pH = 6). Stages I, II, and III are labeled to identify the three stages used to describe the sensor recovery process. The transition stage

from Stage I to Stage II is identified by the change in the slopes of the transients at short times and the grey dashed line is drawn as a guide. Stage II is between the grey and orange dashed lines. The orange dashed line is defined by the wavelength where our mathematic model (Equation (5)) for Stage III starts to deviate from the experiment data. Stage III exists for times beyond the orange dashed line.

Figure 4-7 (a) Time-dependence of the hydrogel-covered Au NR array moisture sensor resonance as the environment RH is suddenly increased from 47% RH to 82% RH at time t=0. The sudden change in RH is realized by quickly transferring the sensor from 47% RH environment into the 82% RH glass chamber in Figure (3-3). (b) The $C(t)$ curve that is converted from the resonance positions in (a) via Equation (1) and Equation (4) [dotted curve] and fitting of the experimental data using Equation (5) [solid line].

Figure 4-8 (a) Resonance variation for the 2.44 ± 0.02 μm thick hydrogel-covered Au NR array moisture sensor as it dries in a 30% RH, T = 23 ^{o}C environment after soaking in water (pH = 6). (b) Resonance variation for the 600 μm thick hydrogel-covered Au NR array moisture sensor as it dries in a 30% RH, T = 23 ^{o}C environment after soaking in water (pH = 6).

Figure 4-9 Wavelength-dependent tuning and performance of hydrogel-covered Au NR optical moisture sensors. (a-c) SEM images of Au NR arrays with diameter 193 ± 4 nm (a), length 362 ± 4 nm / width 238 ± 3 nm (b) and length 640 ± 4 nm / width 217 ± 5 nm (c). (d) Sensor steady state resonance wavelength (λ_{ss}) and resonance variation ($\Delta\lambda'$) over the recovery process as a function of NR length. (e) Sensor frequency variation $\Delta\nu'$ relative to steady state frequency ν_{ss} and FOM as a function of NR length.

Figure 4-10 Transmittance spectra for hydrogel-covered Au NR array moisture sensors fabricated with (a) 193 ± 4 nm nanodot diameter, (b) 362 ± 4 nm NR length and (c) 640 ± 4 nm NR length, as a function of time after being fully soaked in water (pH = 6) and allowed to dry at 30% RH, T=23 ^{o}C. Resonance positions as a function of time extracted from (a-c) and plotted in (d-f),

Chapter 1 Introduction

1-1: Dielectric function of metals and localized surface plasmons

Plasmonics studies the interaction between light and metals. In order to understand the behavior of metals in electromagnetic waves, the Drude model was introduced.[1,2] It describes the response of metals in light as the sea of free electrons creates a plasma that oscillates against the lattice of positive ion cores as a response to an incident electric field $\boldsymbol{E}$.[3] The dynamics of an electron in the plasma sea can be described as:

$$m\ddot{\boldsymbol{x}} + m\gamma\dot{\boldsymbol{x}} = -e\boldsymbol{E} \tag{1.1}$$

where m is the mass of the electron, $\boldsymbol{x}$ is the position of the electron, γ is the collision frequency, and e is the elementary charge. This leads to the dielectric function $\varepsilon(\omega)$ for the plasma of free electrons:

$$\varepsilon(\omega) = 1 - \frac{\omega_p^2}{\omega^2 + i\gamma\omega} \tag{1.2}$$

where $\omega_p = \sqrt{\frac{ne^2}{\varepsilon_0 m}}$ is the plasma frequency of the metal, n is the number of free electrons in a unit volume in the metal, and ε_0 is the vacuum permittivity. Equation (1.2) describes the optical property of ideal metals. Noble metals such as Au and Ag have interband transitions that deviate from the model at visible wavelengths.

The localized surface plasmon describes the interaction between light and sub-wavelength nanoparticles. It can be analyzed by assuming a quasi-static approximation.

For a sub-wavelength metal particle in an external electric field [Figure 1-1], the polarizability α and cross sections for scattering (C_{sca}) and absorption (C_{abs}) can be solved from Maxwell equations as:

$$\alpha = 4\pi a^3 \frac{\varepsilon-\varepsilon_m}{\varepsilon+2\varepsilon_m} \tag{1.3}$$

$$C_{sca} = \frac{8\pi}{3} k^4 a^6 \left|\frac{\varepsilon-\varepsilon_m}{\varepsilon+2\varepsilon_m}\right|^2 \tag{1.4}$$

$$C_{abs} = 4\pi k a^3 \mathrm{Im}\left[\frac{\varepsilon-\varepsilon_m}{\varepsilon+2\varepsilon_m}\right] \tag{1.5}$$

where a is the radius of the metal particle, ε_m is the medium permittivity, and k is the wave vector of the external electromagnetic field.

At the resonance condition (also known as the Frölich condition) where $|\varepsilon + 2\varepsilon_m|$ is a minimum, the scattering and the absorption of the nanoparticle are substantially enhanced. In practice, the quasi-static approximation provides a good description for sub-100 nm spherical or ellipsoidal particles with the incident light in the visible or near-IR wavelength range.[3] For spherical particles with sizes comparable to the wavelength of light, Mie theory can be used to describe the particle scattering. Its solution takes the expression of a series of vector harmonics. In Mie theory, quasi-static approximation results can be recovered by keeping the zero order term of the power series expansion of the scattering coefficient.[3] The first order term of the expansion is usually used as a correction to the quasi-static approximation results. The localized surface plasmon resonance (LSPR) of subwavelength nanopartilces has been widely explored to

manipulate the propagation direction, amplitude, and phase of light for various plasmonic applications.

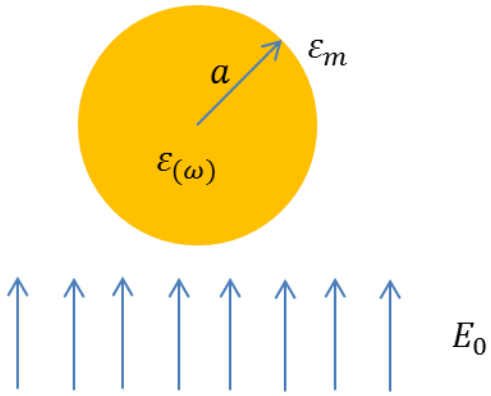

Figure 1-1 A homogeneous sphere placed in an external electric field. Its polarization, internal and external electric fields, cross sections for scattering and absorption can be calculated by assuming a quasi-static approximation.

1-2: Nano-antenna and metasurface

Nanoantennas have LSPRs along their longitudinal and transverse directions, respectively. The longitudinal and transverse resonances are usually in different wavelength regions due to the difference in the nanoantenna length and width dimensions. The longitudinal LSPR of a nanoantenna can be considered as an analog of the half-wave dipole antenna:[4,5]

$$\lambda_{Res} = 2n_{eff}L + C \tag{1.6}$$

n_{eff} indicates the effective refractive index of the media surrounding the nanoantenna, $C = 4Rn_{eff}/m$, and m stands for the order of the resonance.[4] For example Figure 1-2 shows the evolution in the longitudinal LSPR for nanoantennas fabricated from both bulk Au nanoantennas and Au NC-based nanorods. While the width of the nanoantennas is fabricated to be close to 200 nm, the length of the nanoantennas increases from 170 nm to 870 nm. The results show that the longitudinal LSPR increases in an approximately linearly way with the physical length of the nanoantenna.

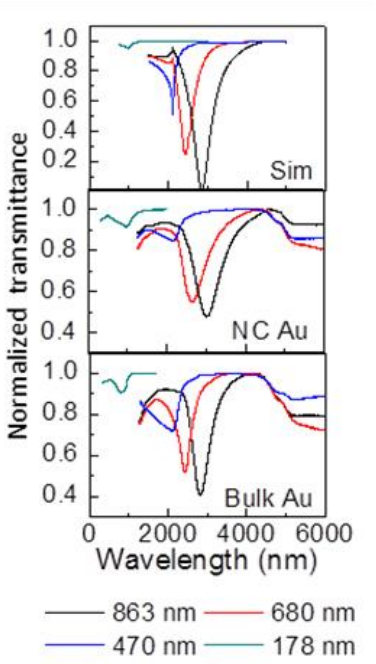

Figure 1-2 Normalized transmittance spectra for Au NC-based nanoantenna arrays from (upper panel) finite difference frequency-domain simulations and (middle panel) FT-IR measurements. Black, red, blue and green curves correspond to the nanoantenna arrays of

863 nm length × 167 nm width, 680 nm length × 178 nm width, 470 nm length × 200 nm width, and 178 nm diameter. (bottom panel) The transmittance spectra for bulk Au nanoantenna arrays of similar sizes: (black) 868 nm × 188 nm, (red) 677 nm × 228 nm, (blue) 492 nm × 250 nm, and (green) 185 nm diameter.[6] [Reprinted with permission from: *Nano Lett.* **2015**, *15*, 5254–5260. Copyright {2015} American Chemical Society.]

Metamaterials are constructed from arrangements of subwavelength, plasmonic building blocks that are tailored in size and shape for the manipulation of electromagnetic waves.[7,8] The nanoantenna is one of the most commonly used plasmonic building blocks. Metasurfaces, known as two-dimensional metamaterials with subwavelength thickness, have drawn a lot of attention for their simpler design, fabrication, and their comparable ability to control light magnitude, phase, and polarization. An example of ultrathin metasurface quarter wave-plates made from nanoantenna arrays of different dimensions are presented in Figure 1-3. Metasurfaces enable a spatially varying optical response that can be designed at will and allows for integration of actively tunable components for their real-time tuning.[9]

While most metasurfaces operate at fixed wavelengths or over a limited wavelength range, reconfigurable metasurfaces can have a large working wavelength variation due to the integration of actively tunable components into the metasurface. These actively tunable materials include electron carrier injection semiconductors,[10,11] phase transition materials[12] and elastomeric substrates.[13,14] An example of a

reconfigurable metasurface is a tunable split ring resonator and bar array that was fabricated on an elastomeric substrate [Figure 1-4].

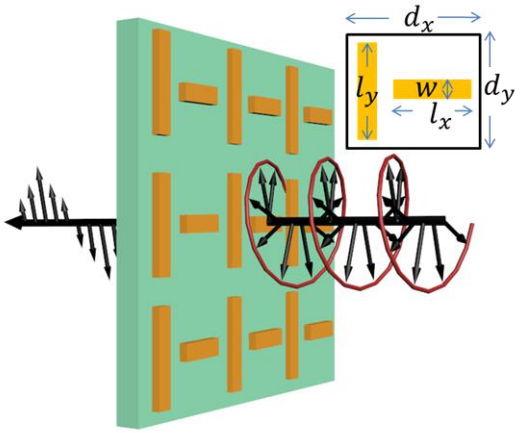

Figure 1-3 An example of metasurface. It is composed of two sets of nanoantennas of different dimensions along the x and y directions. The metasurface works as quarter wave-plate in a wavelength range defined by the resonance wavelengths of the two sets of nanoantennas.[6] [Reprinted with permission from: *Nano Lett.* **2015**, *15*, 5254–5260. Copyright {2015} American Chemical Society.]

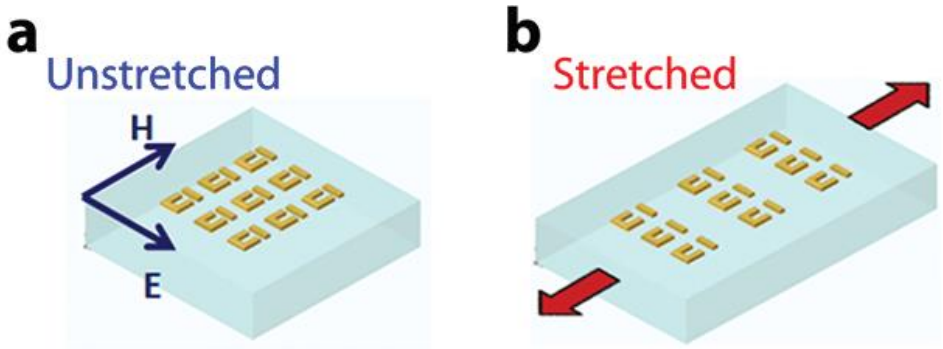

Figure 1-4 An example of reconfigurable metasurface on elastomeric substrate. (a) Split ring resonator and bar arrays fabricated on elastomeric substrate without stretching. With stretching, the distance between the split ring resonator and the bar increases, thus changing the optical response of the metasurface.[13] [Reprinted with permission from: *Nano Lett.* **2010**, *10*, 4222–4227. Copyright {2010} American Chemical Society.]

1-3: Outline of Thesis

The thesis focuses on 1) designing material permittivity by continuously tuning interparticle distance in colloidal Au nanocrystal solids, 2) developing a quick, large-area process using colloidal Au NCs to construct metasurfaces, and 3) fabricating reconfigurable plasmonic sensors for moisture and strain sensing.

Chapter 2 introduces an approach to design the permittivity of colloidal Au NC solids by tuning the interparticle distance. Ligands serve to cap colloidal NCs and different ligands may be introduced by a process known as ligand exchange. By intentionally mixing two ligands with different molecular lengths at different ratios via a

partial ligand exchange process, we show the interparticle distance can be tuned from 0 to 20 Angstroms, resulting in a continuous variation of Au NC solid permittivity. Materials with high imaginary part of the permittivity are found which have potential applications as absorbers and in photo-thermal conversion.

Chapter 3 introduces a fast, large-area, and low-cost nanoscale fabrication method for metasurfaces that combines nanoimprinting and colloidal Au NC solution-based deposition. Using this method, ultrathin metasurface quarter wave-plates are demonstrated. Among them, the extreme bandwidth quarter wave-plate is demonstrated over the wavelength range from 2500 nm to 5000 nm for the first time.

Chapter 4 introduces an optical moisture sensor that is composed of hydrophilic hydrogel films and Au nanorod arrays. It works by transducing the refractive index change of the hydrogel upon exposure to moisture into spectral shifts of the high-reflectivity LSPR of the Au nanorod array. It is designed to meet the needs of large-area, high-resolution remote sensing of soil moisture. The sensor is further improved on two aspects: integration of colloidal Au NC plasmonic building blocks for low-cost, large-area fabrication and removal of the substrate by template-stripping to create free-standing hydrogel/Au nanorod array sensors.

Chapter 5 introduces plasmonic Au gratings on polydimethylsiloxane (PDMS) substrates. An easy and time-efficient fabrication method to create nanoscale structures on PDMS substrates is introduced. Different designs are tested for enhancing the tunability of the grating pitch. The dimensions of the Au grating are designed to achieve a

hybridized, ultrasharp resonance peak. Optical measurements and simulations are being carried out for the demonstration of large resonance wavelength variation. This ultrasharp, large variation Au grating resonance has potential for applications in ultrasensitive sensing and imaging.

Chapter 6 presents future work on low-cost, large-area, multifunctional optical metasurfaces and reconfigurable plasmonic devices, for example, metalenses, high-efficiency absorbers, and multifunctional hydrogel-based plasmonic sensors, and concludes this thesis.

1-4: References

(1) Drude, P. *Ann. Phys.* **1900**, *306*, 566.

(2) Drude, P. *Ann. Phys.* **1900**, *308*, 369.

(3) Maier, S. A. *Plasmonics: Fundamentals and Applications*; 1st ed.; Springer: New York, 2007.

(4) Aksu, S.; Yanik, A. a; Adato, R.; Artar, A.; Huang, M.; Altug, H. *Nano Lett.* **2010**, *10*, 2511–2518.

(5) Cubukcu, E.; Capasso, F. *Appl. Phys. Lett.* **2009**, *95*, 201101.

(6) Chen, W.; Tymchenko, M.; Gopalan, P.; Ye, X.; Wu, Y.; Zhang, M.; Murray, C. B.; Alu, A.; Kagan, C. R. *Nano Lett.* **2015**, *15*, 5254–5260.

(7) Soukoulis, C. M.; Wegener, M. *Nat. Photonics* **2011**, *5*, 523–530.

(8) Shalaev, V. M. *Nat. Photonics* **2007**, *1*, 41–48.

(9) Chen, H.-T.; Taylor, A. J.; Yu, N. *Reports Prog. Phys.* **2016**, *79*, 76401.

(10) Chen, H.-T. In *2010 IEEE Photonics Society Winter Topicals Meeting Series (WTM)*; IEEE, 2010; Vol. 444, pp. 28–29.

(11) Park, J.; Kang, J.-H.; Kim, S. J.; Liu, X.; Brongersma, M. L. *Nano Lett.* **2017**, *17*, 407–413.

(12) Liu, M.; Hwang, H. Y.; Tao, H.; Strikwerda, A. C.; Fan, K.; Keiser, G. R.; Sternbach, A. J.; West, K. G.; Kittiwatanakul, S.; Lu, J.; Wolf, S. a; Omenetto, F. G.; Zhang, X.; Nelson, K. a; Averitt, R. D. *Nature* **2012**, *487*, 345–348.

(13) Pryce, I. M.; Aydin, K.; Kelaita, Y. A.; Briggs, R. M.; Atwater, H. A. *Nano Lett.* **2010**, *10*, 4222–4227.

(14) Huang, F.; Baumberg, J. J. *Nano Lett.* **2010**, *10*, 1787–1792.

Chapter 2 Designing material permittivity by continuously tuning interparticle distance in colloidal Au nanocrystal (NC) solids

Significant components of this chapter will be submitted as "Designing Material Permittivity by Continuously Tuning Interparticle Distance in Colloidal Au Nanocrystal Solids" by Wenxiang Chen, Prashanth Gopalan, Naixin Song, Christopher B. Murray, Cherie R. Kagan.

The permittivity of plasmonic building blocks plays a significant role in the function of metamaterials. Low-loss plasmonic materials are beneficial for the fabrication of light-bending or -scattering metamaterials such as metalenses[1,2], metasurface polarizers[3], optical filters and quarter wave-plates.[4,5] High absorption plasmonic materials, on the other hand, are promising for energy collection for chemical catalysts and photovoltaics,[6,7] surface enhanced Raman scattering sensors[8] and biomedical applications.[9] However, the most commonly used plasmonic materials are limited to metals such as Ag, Au, and Cu with fixed permittivity. Recently, our group reported the design of material permittivity from that characteristic of a dielectric material to that of metal by controlling the interparticle spacing in colloidal Au nanocrystals (NCs) assemblies using different length capping ligands.[10] However, the available permittivities are still too few to satisfy the demands of the plasmonic applications as the range of interparticle spacings becomes "digitally-controlled" by the integer number of atoms in

the selected ligands. Here, we report a method to continuously tune the permittivity of colloidal Au NC thin films across the dielectric to metallic transition by mixing two different length ligands for capping the surface of colloidal Au NCs.

2-1 Colloidal Au NC synthesis and characterization

5 nm colloidal gold NCs are synthesized using a previously reported method[11] with some modifications. 200 mg of hydrogen tetrachloroaurate (III) hydrate, 10 mL of oleylamine (OLA), and 10 mL of tetralin are mixed at room temperature. The mixture is magnetically stirred under a nitrogen flow for 5 min. 1 mmol tert-butylamine–borane (Aldrich) is dissolved in 1 mL OLA and 1 mL tetralin by sonication, and then injected into the precursor solution. The solution changes color to deep red in 5 s. The solution is allowed to react for 1 h at room temperature and then 60 mL acetone is added to precipitate the Au NCs. The Au NCs are collected by centrifugation (8000 rpm, 6 min), washed twice with ethanol and then dispersed in hexanes. The colloidal Au NCs are capped with OLA ligands of 1-2 nm molecular length after synthesis.

The post-deposition exchange of the OLA ligands with more compact alternatives: ethanedithiol (EDT) and ammonium thiocyanate (SCN) is well studied in our group's previous paper [Figure 2-1].[10] TEM images of monolayer Au NCs clearly show the decreased interparticle spacing for EDT and SCN ligands. The DC resistivity of the Au NC film decreases from $10^6\ \Omega \cdot m$ to $5.1 \times 10^{-5}\ \Omega \cdot m$ from OLA ligands to SCN ligands, consistent with a transition from dielectric to metallic behavior.

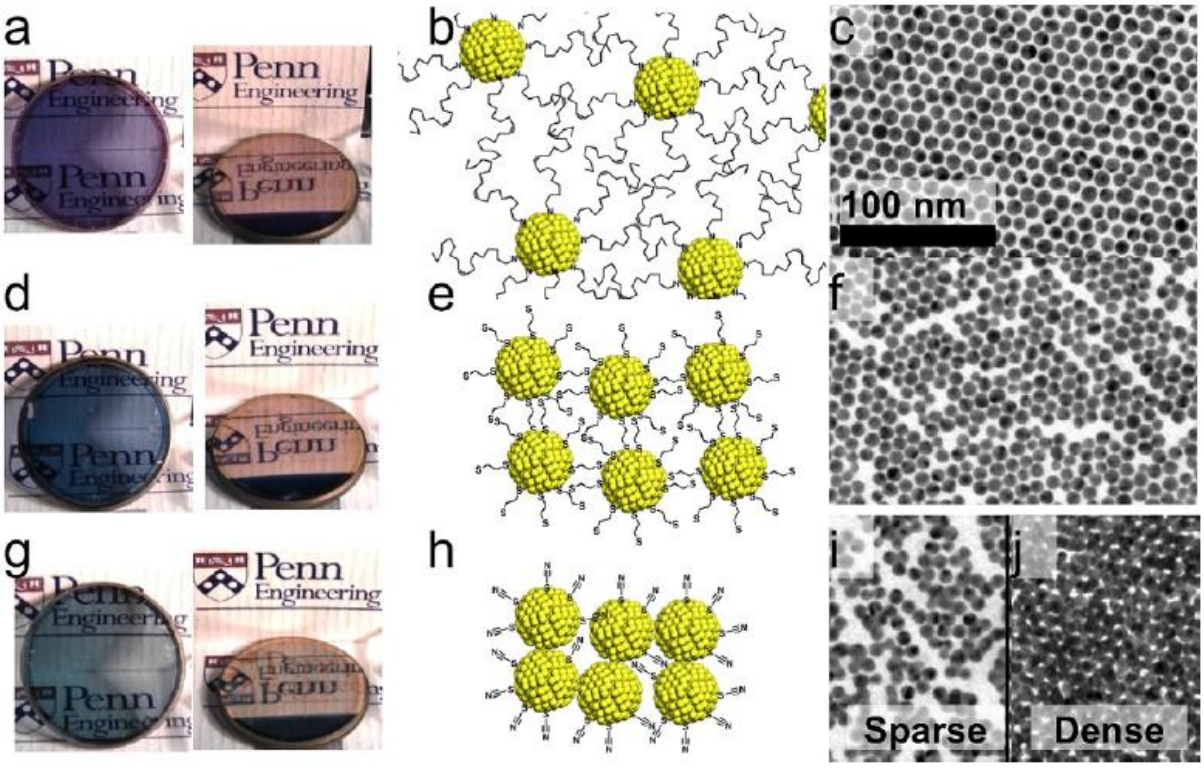

Figure 2-1 Au NCs of different length molecular capping ligands. Photo images of spin-coated Au NC thin films on optical flats, schematics, and TEM images with different molecular capping ligands. (a-c) Oleylamine (OLA). (d-f) Ethanedithiol (EDT). (g-j) Ammonium thiocyanate (SCN).[10] [Reprinted with permission from: *Nano Lett.* **2013**, *13*, 350–357. Copyright {2013} American Chemical Society.]

2-2 Tuning of permittivity of colloidal Au NC films

Different from previously reported ligand exchange process of completely replacing OLA ligands with EDT or SCN alternatives, we introduce a partial ligands exchange process for replacing a varying percentages of the OLA ligands on Au NC

surface with SCN ligands. The advantage of the partial ligand exchange process is that the interparticle spacing of Au NCs can be tuned by carefully controlling how much of the OLA ligands is replaced by SCN ligands in the NC solids. As a chemical reaction, the ligand exchange rate depends on the concentration of the SCN ligands solution. We deliberately use extremely low concentration SCN in acetone solutions (0.01 mg/mL) to decrease the reaction speed and easily control the replacement of OLA ligands. The colloidal Au NCs are spincast on glass substrates and dipped in the SCN solutions for various times ranging from 1 min to 3 min [Figure 2-2 (a)]. Longer reaction time results in more OLA ligands being replaced. FTIR spectra of the colloidal Au NC films before and after ligand exchange are both measured to determine the C-H stretching intensity inside the film. Since only OLA ligands in the Au NC systems contain the C-H group, the percentage of OLA ligands that have been exchanged can be determined from the variation of C-H stretching intensity before and after the partial ligand exchange. To calculate the C-H stretching peak intensity in the FTIR spectra, we integrate the transmittance spectra from 2700 cm^{-1} to 3120 cm^{-1} for Au NC films before (I_1) and after (I_2) ligand exchange [Figure 2-2 (b)]. After different time ligand exchange processes, different amounts of OLA are replaced by SCN ligands, resulting in a C-H stretching peak of smaller intensity in the FTIR spectra. The percentage of OLA that is remained in colloidal Au NC thin films are defined as $x = I_1/I_2 \times 100(\%)$.

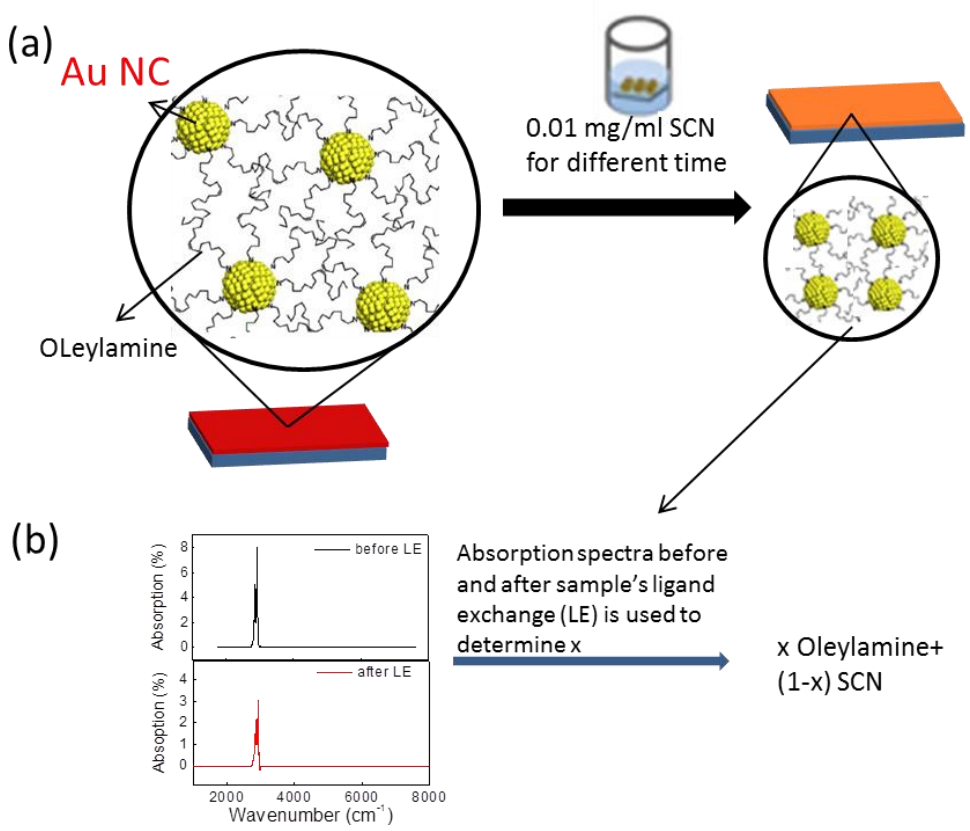

Figure 2-2 Partial ligand exchange process for colloidal Au NC thin films with SCN ligands. (a) Colloidal Au NC thin films are dipped in 0.01 mg/mL solutions of SCN in acetone for different times ranging from 1 min to 3 min. (b) The percentage of OLA ligands that have been exchanged by SCN ligands is determined by integrating the C-H stretching region (2700 cm^{-1} to 3120 cm^{-1}) in the baseline corrected FTIR spectra before (I_1) and after (I_2) ligand exchange. The percentage of OLA ligands after ligand exchange is defined by $x = I_1/I_2 \times 100(\%)$.

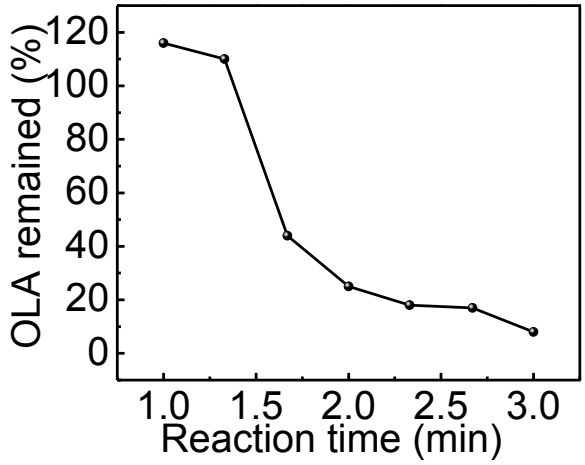

Figure 2-3 The remaining percentage of OLA ligand in Au NC solids as a function of reaction time for the partial ligand exchange process.

As ligand exchange time varies from 1 min to 3 min, the percentage of OLA ligand remaining in colloidal Au NC thin films varies from 116% to 8% [Figure 2-3]. The highest percentage of 116% exceeds that of 100% and is believed to arise from shrinking of the colloidal Au NC thickness after ligand exchange. We are correcting this by measuring thickness variation before and after ligand exchange. The transmittance of the partially ligand-exchanged colloidal Au NC thin films is shown in [Figure 2-4]. For the Au NC solid without any ligand exchange, its transmittance spectrum has a resonance peak at 600 nm due to the localized surface plasmon resonance (LSPR) characteristic of the individual Au NCs in the films. As the OLA ligands are replaced with more SCN ligands in the system, the interparticle spacing decreases and the LSPR resonance at 600 nm gradually vanishes. As the whole Au NC film becomes more metallic, its

transmittance decreases in the wavelength range of 800 nm to 3000 nm. This is consistent with the Drude behavior of metals, which are mainly reflective in this wavelength range since the complex refractive index is predominantly imaginary.[12] At wavelengths shorter than 450 nm, the transmittance of the Au NC film drops quickly due to interband transitions.

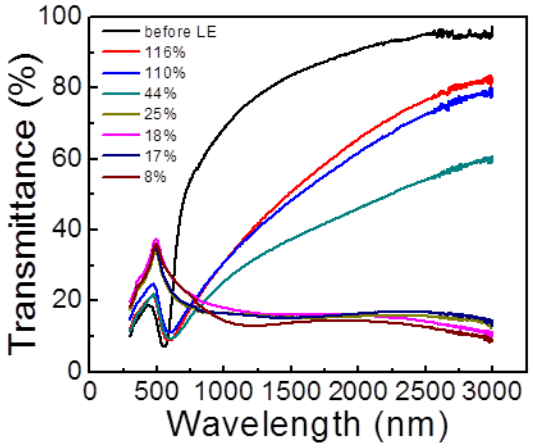

Figure 2-4 Transmittance spectra of the partially exchanged colloidal Au NC thin films with x percentage of OLA ligands left.

The permittivity of the partially ligand-exchanged colloidal Au NC thin films are characterized by ellipsometry within 2 days of the preparation of the samples [Figure 2-5]. For NC films without ligand exchange, the real part of the permittivity is positive over all the measured wavelength range from visible to near infrared (NIR). As more SCN

ligands are introduced into the system, the real part of the permittivity (e_1) for the films decreases gradually from positive to negative values, suggesting a transition from insulating behavior to metallic behavior. On the other hand, the imaginary part of the permittivity (e_2) first increases in the NIR to a maximum value at 8% OLA ligands and then decreases as the film becomes fully SCN ligand exchanged. The permittivity of 18%, 17% and 8% SCN-exchanged Au NC thin films, e_1 is negative and small, suggesting that they are good epsilon-near-zero materials. e_2 is larger than the fully SCN ligand-exchanged samples, suggesting that they can be more absorptive.

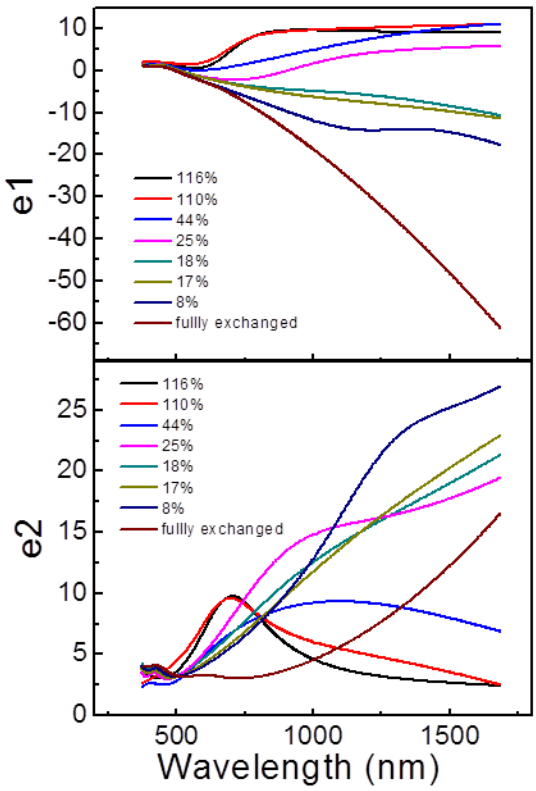

Figure 2-5 Permittivity of the partially ligand-exchanged colloidal Au NC thin films measured by ellipsometry.

2-3 Tuning of permittivity of colloidal Au nanorod

Nanorods are one of the basic building blocks for metamaterials. The permittivity of colloidal Au NC nanorods can be tuned by the same partial ligand exchange method, but with a more diluted concentration of SCN in acetone (0.001 mg/mL) to slow down the ligand exchange rate further. This is because the surface to volume ratio for colloidal Au NC nanorods is higher than that of the colloidal Au NC films. The chemical reaction

rate is thus faster for the colloidal Au NC nanorods during the partial ligand exchange. Colloidal Au NC nanorod arrays with nanorods 1100 nm length, 230 nm width, on a 1500 nm pitch are fabricated by nanoimprinting and solution-based deposition of NCs described in detail in Chapter 3-1 [Figure 2-6].[4] The transmittance spectra of the partially ligand-exchanged colloidal Au NC-based nanorods are shown in Figure 2-7, with linear incident polarization along the longitudinal direction of the nanorods. As ligand exchange time increases, more OLA ligands are replaced by compact SCN ligands, and the interparticle spacing decreases, giving rise to a resonance peak that moves towards longer wavelengths. For the no ligand exchange curve, its resonance position is at 600 nm which is the characteristic of the LSPR of the individual colloidal Au NC. For the fully ligand-exchanged curve, its resonance is at 3000 nm consistent with the LSPR along the longitudinal direction of the nanorods.

While we still need to collect FTIR spectra of the Au NC nanorod array before and after ligand exchange to determine how much OLA ligand is being replaced by SCN ligands, it is interesting to explore the evolution in optically properties of partially exchanged Au nanorods to see if they can make better absorber materials than traditional metals such as Au. A quick finite domain time-difference (FDTD) simulation is carried out to compare the transmittance and absorption of the bulk Au nanorods and fully ligand-exchanged colloidal Au NC nanorods [Figure 2-8] based on ellipsometry data we collected earlier. The fully ligand-exchanged colloidal Au NC nanorods have a smaller transmission resonance amplitude, but a larger absorption from 1000 nm to 5000 nm, compared with bulk Au nanorods of the same size. We plan to apply the simulation to

colloidal Au NC nanorods with other permittivity, and study their absorbing ability at different wavelength range. Right now the challenge is the nanorod resonance is in the mid-IR, while our ellipsometry data stops at 1600 nm. For the simulation in Figure 2-8, the permittivity results are extended to 5000 nm via drude model. We may need to consider study nanorods with smaller dimensions. This project is ongoing.

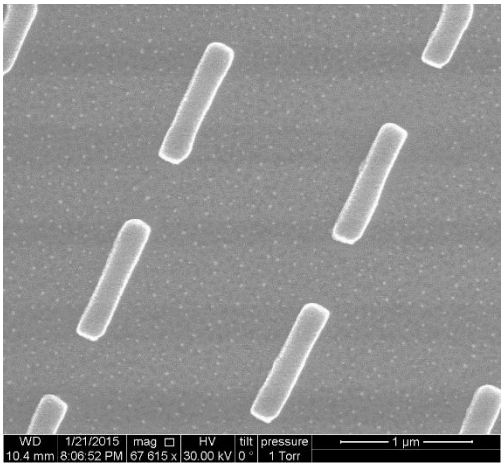

Figure 2-6 SEM images of the colloidal Au nanorods.

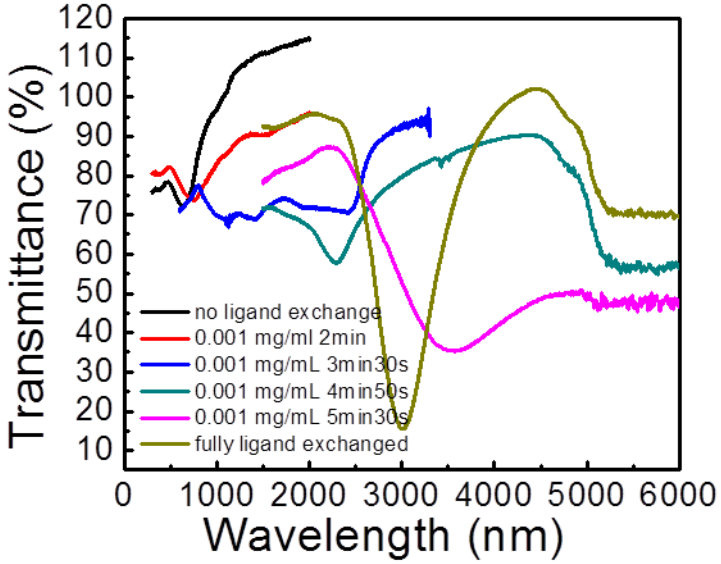

Figure 2-7 Partially ligand-exchanged colloidal Au NC nanorods. The partial ligand exchange process is carried out in 0.001 mg/mL SCN in the acetone solution for various time from 2 min to 5 min 30 s.

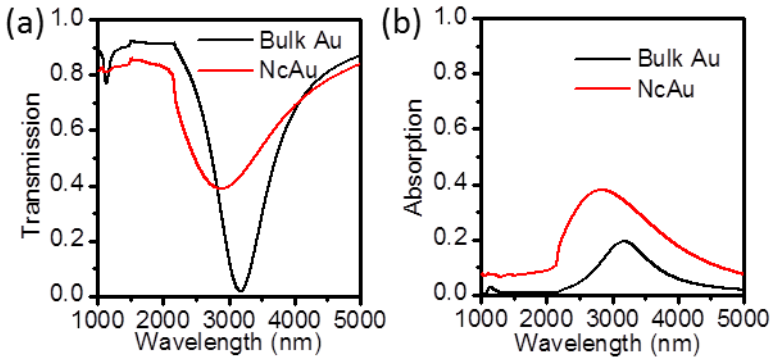

Figure 2-8 Simulation results for the transmittance (a) and absorption (b) of the bulk Au nanorods and fully ligand-exchanged colloidal Au NC nanorods. The dimensions of the

Au nanorod array in the simulation are 1000 nm in length, 250 nm in width and 2500 nm in pitch.

2-4 Reference

(1) Aieta, F.; Genevet, P.; Kats, M. a; Yu, N.; Blanchard, R.; Gaburro, Z.; Capasso, F. *Nano Lett.* **2012**, *12*, 4932–4936.

(2) Chen, X.; Huang, L.; Mühlenbernd, H.; Li, G.; Bai, B.; Tan, Q.; Jin, G.; Qiu, C.-W.; Zhang, S.; Zentgraf, T. *Nat. Commun.* **2012**, *3*, 1198.

(3) Ellenbogen, T.; Seo, K.; Crozier, K. B. *Nano Lett.* **2012**, *12*, 1026–1031.

(4) Chen, W.; Tymchenko, M.; Gopalan, P.; Ye, X.; Wu, Y.; Zhang, M.; Murray, C. B.; Alu, A.; Kagan, C. R. *Nano Lett.* **2015**, *15*, 5254–5260.

(5) Zhao, Y.; Aluì, A. *Nano Lett.* **2013**.

(6) Linic, S.; Christopher, P.; Ingram, D. B. *Nat. Mater.* **2011**, *10*, 911–921.

(7) Atwater, H. a; Polman, A. *Nat. Mater.* **2010**, *9*, 865–865.

(8) Jackson, J. B.; Halas, N. J. *Proc. Natl. Acad. Sci. U. S. A.* **2004**, *101*, 17930–17935.

(9) Jain, P. K.; Huang, X.; El-Sayed, I. H.; El-Sayed, M. A. *Acc. Chem. Res.* **2008**, *41*, 1578–1586.

(10) Fafarman, A. T.; Hong, S.-H.; Caglayan, H.; Ye, X.; Diroll, B. T.; Paik, T.; Engheta, N.; Murray, C. B.; Kagan, C. R. *Nano Lett.* **2013**, *13*, 350–357.

(11) Peng, S.; Lee, Y.; Wang, C.; Yin, H.; Dai, S.; Sun, S. *Nano Res.* **2008**, *1*, 229–234.

(12) Maier, S. A. *Plasmonics: Fundamentals and Applications*; 1st ed.; Springer: New York, 2007.

Chapter 3 Large-area Nanoimprinted Colloidal Au Nanocrystal-based Nano-antennas for Ultrathin Polarizing Plasmonic Metasurfaces[1]

This work was published in Nano Letters, entitled "Large-area Nanoimprinted Colloidal Au Nanocrystal-based Nano-antennas for Ultrathin Polarizing Plasmonic Metasurfaces" Chen, W.; Tymchenko, M.; Gopalan, P.; Ye, X.; Wu, Y.; Zhang, M.; Murray, C. B.; Alu, A.; Kagan, C. R. [Reprinted with permission from: *Nano Lett.* **2015**, *15*, 5254–5260. Copyright {2015} American Chemical Society.][1]

Optical metamaterials are constructed from arrangements of subwavelength, plasmonic building blocks that are tailored in size and shape.[2–4] While three-dimensional metamaterials have been shown to manipulate light propagation in the bulk, with exotic effects in both the near and far fields, two-dimensional metasurfaces have recently drawn a lot of attention as alternatives for their simpler design and fabrication, and for their comparable ability to enhance electromagnetic fields and control light polarization. Metasurfaces consisting of subwavelength plasmonic inclusions arranged in two-dimensional arrays have been demonstrated to manipulate visible and infrared absorption,[5–8] luminescence,[9–11] and scattering[7,12,13] in a variety of devices, such as sensors,[8,14,15] photodetectors and photovoltaics,[16–18] flat plasmonic metalenses,[19–21] quarter-wave plates,[22–25] optical resonator interfaces,[26,27] and holography plates.[28,29] However, to define the nanoscale size, complex shapes, and intricate spatial arrangement

of plasmonic building blocks in most two-dimensional metasurfaces, they have generally been fabricated by electron-beam lithography with subsequent metal evaporation or by focused-ion beam lithography to ion mill deposited thin metal films. These methods are expensive and time-consuming, because they require many consecutive steps and the use of high vacuum during metal deposition, which hinders large-area fabrication.

Nanoimprint lithography provides a low-cost, large-area, high-throughput alternative technique for patterning the subwavelength structures constituting optical metasurfaces.[30–33] Colloidal metal nanocrystals (NCs) behave like inks that allow solution-based deposition of metal nanostructures over large areas, promising to drive down the cost of production.[34–36] In recent reports, direct nanoimprint lithography of templates into Au NC dispersions deposited on substrates were shown to produce arrays of subwavelength, plasmonic nanopillars of simple shape.[34,37] However, these simple Au NC-based nanopillar arrays were large in size and/or pitch, had significant non-uniformities in edge roughness and shape, and were of limited thickness. Most metasurface devices require more complex, anisotropic plasmonic inclusions that are uniform in shape, tailored in height, and closely spaced to locally control the intensity, the phase, and the polarization of transmitted light,[8,9,19–24,26–29,38] than those accessible by direct nanoimprinting. Here we demonstrate that thermal nanoimprint lithography and solution-based deposition of colloidal Au NCs can be successfully combined to fabricate metasurfaces consisting of plasmonic nanorods of various size, shape, and spacing. By engineering the dimensions of the nanorods, we are able to tune the frequency of their plasmonic resonance and the magnitude and phase of their polarization.

3-1 Imprinting template fabrication

Master template fabrication method is as following: a 1.5 cm by 1.5 cm device grade silicon wafer with 250 nm thermal silicon oxide (SiO_2) is cleaned by an O_2 plasma (75 mTorr, 150 W) for 10 min. The electron-beam lithography resist poly(methyl methacrylate) (PMMA) 495 A4 (diluted to A2 in anisole) is deposited by spin-coating at 3000 rpm for 1 min, is prebaked at 180 ^oC for 2 min, and is allowed to cool to room temperature for 2 min. A second resist layer of PMMA 950 A2 is then deposited following the same procedure. The total resist thickness is about 120 nm. The pattern is then exposed in an Elionix electron-beam lithography system operating at a 50 kV accelerating voltage. After exposure, the sample is developed in a 1:3 solution of mythyl isobutyl ketone (MIBK) and isopropanol (IPA) for 90 s. Residual resist is removed by descumming in an O_2 plasma (75 mTorr, 70 W) for 6 s. A 12 nm chromium mask is deposited onto the sample using electron-beam evaporation at 0.3 Å/s and then the sample is soaked in remover PG at 75 ^oC for 8 h to complete the lift off process. Reactive ion etching is used to etch 200 nm into the SiO_2 layer to define the nano-antenna master templates, 250 nm into the SiO_2 layer for the mid-IR quarter-wave plate master template, and 250 nm into the SiO_2 layer and then 60 nm into the Si substrate for the extreme bandwidth quarter-wave plate master template. These etching depths are optimized to yield the best nanoimprinting results. The chromium mask is removed by soaking the sample in etchant for 2 min and then rinsed with deionized (DI) water twice. The sample is then treated with an oxygen (O_2) plasma (75 mTorr, 150 W) for 10 min and then

soaked in a 1:1000 n-octadecyltrichlorosilane solution in hexane for 10 min. The template is subsequently rinsed in hexane and DI water [Figure 3-1].

Nano-antenna arrays and metasurface quarter-wave plates are fabricated by thermal imprinting and solution-based colloidal Au nanocrystal deposition [Figure 3-2 (a-d)]. The substrate is cleaned with acetone and IPA. NXR-1000 thermal imprint resist is deposited by spin-coating onto the substrate at 3000 rpm for 1 min and is prebaked at 155 ^{o}C for 5 min. The master template consisting of either nano-antenna arrays or the quarter-wave plate pattern is placed on top of the substrate. The master template, thermal resist, and substrate stack is heated to 133 ^{o}C and compressed at 350 psi for 5 min 30 s, and then cooled to room temperature in a Nanonex NX-2600 nanoimprint tool. The template is then carefully detached from the substrate by hand. An oxygen plasma descum process (75 mTorr, 70 W, 6 s) is performed to remove the residual layer in the imprinted area. The Au NC dispersion (concentration varying from 10 mg/mL to 20 mg/mL) is deposited by spin-coating on the resist patterned substrate at 1000 rpm for 30 s. The resist is lifted off in acetone with mild sonication for 30 s. Finally ligand exchange is carried out by immersing samples into 1% NH_4SCN in acetone for 2 min, followed by rinsing twice in clean acetone for 2 min to remove unbound ligand. A representative NC-based nano-antenna array fabricated by this method is shown in Figure 3-2 (e).

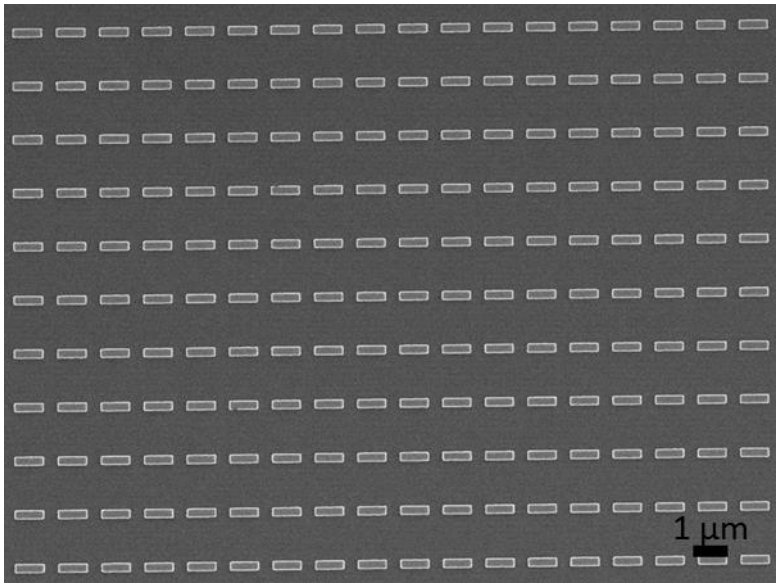

Figure 3-1 SEM image of a representative master template. The nanorods in the template have a length of 816 nm and a width of 242 nm.

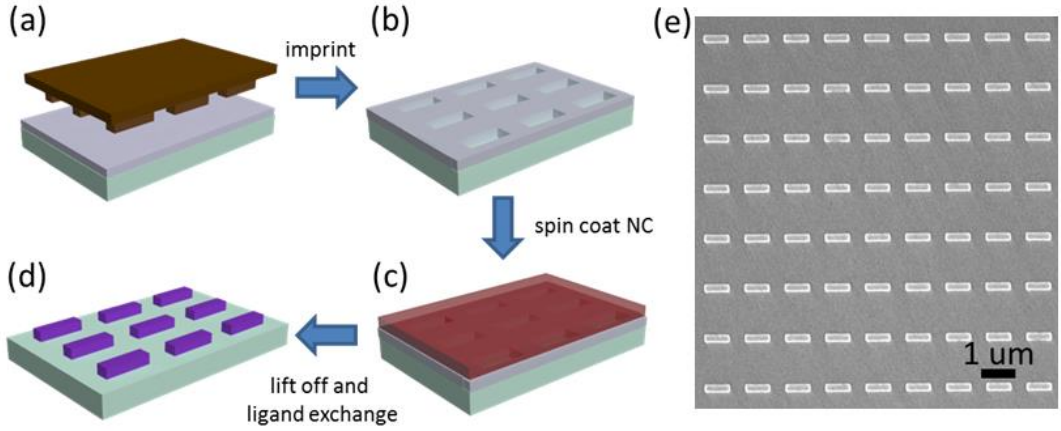

Figure 3-2. Nano-antenna fabrication by (a) thermal nanoimprint lithography to (b) transfer the master pattern into the resist, followed by (c) spin-coating of colloidal Au

NCs and (d) ligand exchange and resist lift-off. (e) SEM image of a representative NC-based nano-antenna array fabricated by the nanoimprinting method.

3-2 Nano-antennas based on colloidal Au NCs

Figure 3-2 (e) shows a representative scanning electron micrograph (SEM) of a Au NC-based nanorod array. SEM images are taken from different regions of the sample to determine the uniformity in the nanorod dimensions across the array [Figure 3-3]. Across the 1.44 mm^2 sample area, the size and size variation in the nano-antenna length is 749 nm +/- 13 nm and width is 229 nm +/- 5 nm. The line edge roughness (LER) for the NC-based nano-antennas is 2.9 nm and the misalignment, defined as the standard deviation in the orientation of the nanorods, is 0.4° [Table 3-1]. The dimensions of the imprinted nano-antennas are 5%-20% smaller than the features in the master template due to shrinkage of the NC-based nanostructures as the long OAm ligands used to synthesize and disperse the Au NCs in solution are replaced by the compact SCN ligands. The degree of shrinkage depends on the amount of OAm ligands in the NC dispersion and may be reduced by removing excess ligands by washing, but not too much such that the NC dispersion becomes unstable and unusuable. We note that the LER and misalignment of the nanoimprinted nano-antennas are similar to that for a Au NC nanorod array patterned by e-beam lithography [Figure 3-4 and Table 3-1].

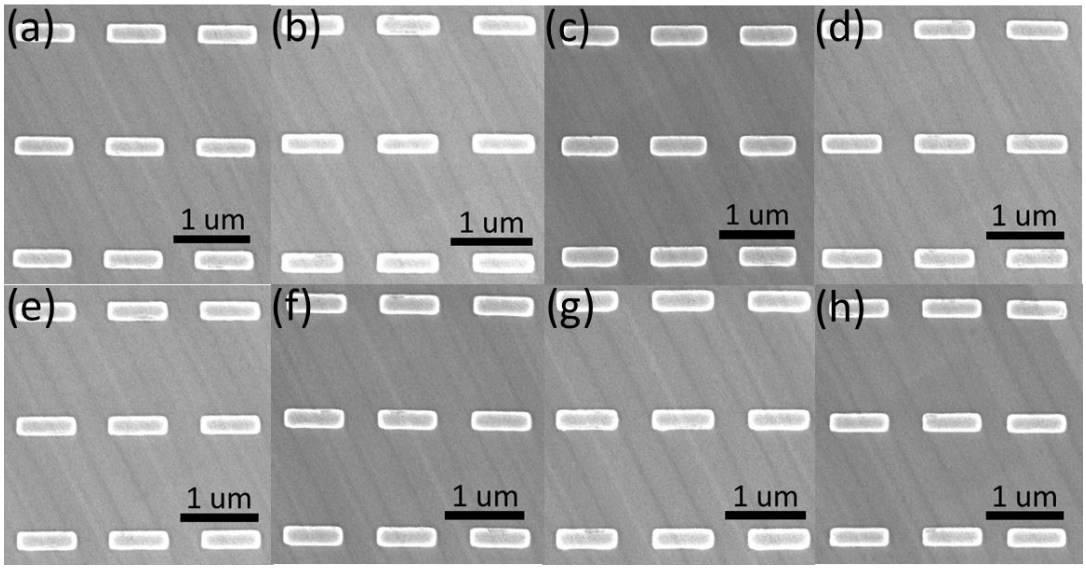

Figure 3-3 SEM images taken from 8 different areas across a NC-based nano-antenna array [the same sample as in Figure 3-2 (e)] to determine the length and width and their variations.

	Figure 3-3	QWP Figure 3-10		Extreme bandwidth QWP Figure 3-14		Au NC nanorod array fabricated by e-beam lithography
Nanorod direction	Horizontal	Vertical	Horizontal	Vertical	Horizontal	Horizontal
Number of nanorods analyzed	8	8	8	4	16	12
Average edge roughness	2.9 nm	2.9 nm	2.9 nm	7 nm	4.5 nm	5.9
Misalignment	0.4°	0.2°	0.2°	0.1°	0.6°	1.5°

Table 3-1 Line-edge roughness (LER) and misalignment of nanoimprinted, colloidal Au NC metasurfaces.

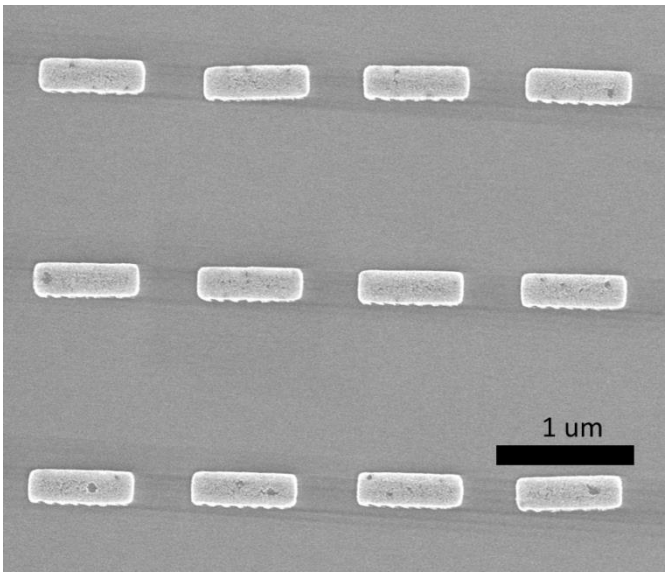

Figure 3-4 SEM image of a Au NC nanorod array patterned by e-beam lithography.

We also investigate the uniformity in nanorod height. Nano-antenna arrays with heights ranging from 71 to 119 nm are fabricated by controlling the concentration of the Au NC dispersions used in spin-coating from 10 mg/mL to 20 mg/mL. Variations in height across the nanorods are evident by the contrast in atomic force microscopy images and by the line cuts shown in Figure 3-5 (a-d). The nanorods are taller at their edges akin to a "rabbit ear" effect that may arise from (1) incomplete filling of the Au NCs, (2) greater adhesion between the Au NCs and the resist layer, and/or (3) lift-off.[40,41] The height difference between the nanorod edge and the nanorod center is reduced for the thicker 119 nm NC films [Figure 3-5 (d)], allowing the fabrication of more uniform nanorods. As the height of the nano-antenna arrays increases, the plasmon resonance extinction increases and blue shifts [Figure 3-5 (e)]. The increased extinction is caused by the larger amount of plasmonic material in each nanorod. The increased height also weakens the hybridization of the surface plasmons located at the top and bottom surfaces of the nanorod, leading to a blue shift in the resonance,[42] a counterintuitive effect for nanostructures, since it leads to a blue shift despite the increase in volume.[43] It is worth noting that the resonance shift is nonlinear. For thinner films approaching the 30 nm skin depth of Au, the shift becomes much more significant than that for the thicker films studied here.[32]

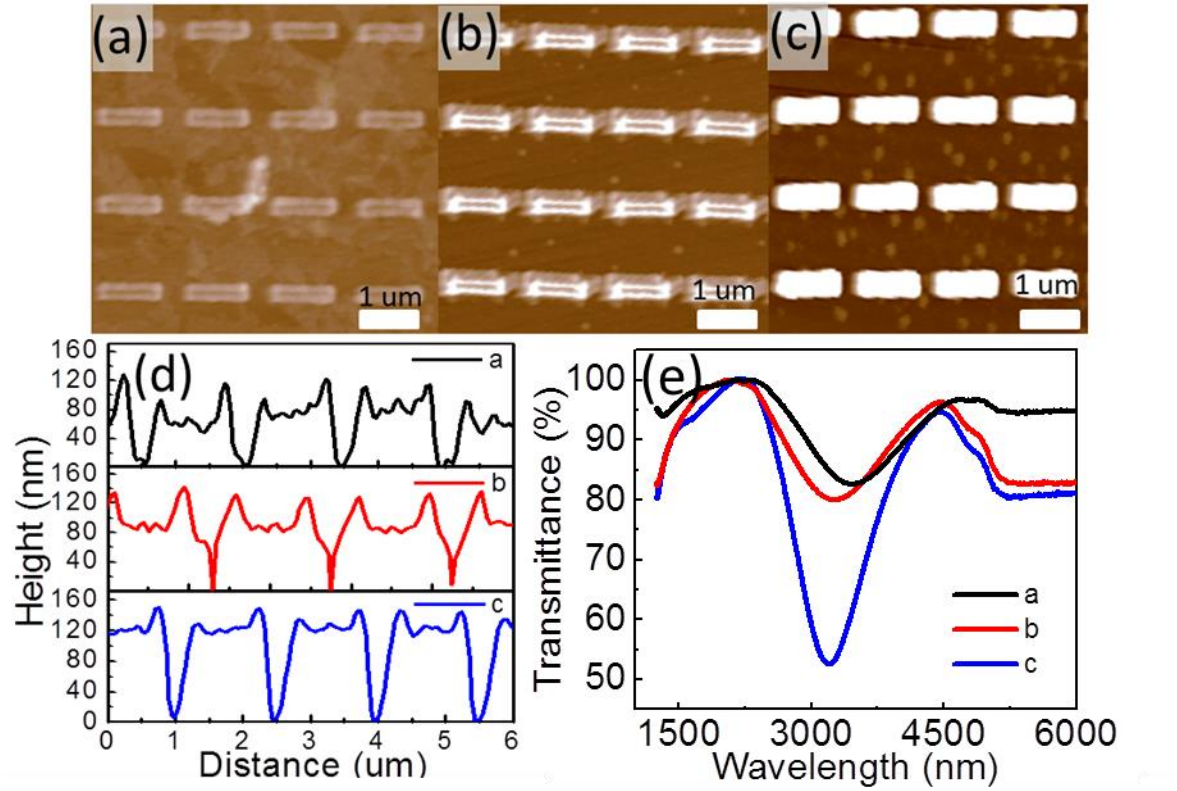

Figure 3-5 Atomic Force Microscopy images of nanocrystal-based nano-antennas fabricated with heights of (a) 71 nm, (b) 81 nm and (c) 119 nm. (d) Line cuts of the AFM images and (e) transmittance measurements for the nanorod samples shown in (a-c).

Using nanoimprint lithography we fabricate arrays of nanorods tailored in size to have lengths and widths of (a) 863 nm x 167 nm, (b) 680 nm x 178 nm, (c) 470 nm x 200 nm, and (d) 178 nm x 178 nm [Figure 3-6 (a-d)]. Their horizontal [0 degree direction in the inset in Figure 3-6 (a)] and vertical [90 degree direction] pitches are (a) 1.5 μm x 1.5 μm, (b) 1.2 μm x 1.5 μm, (c) 0.9 μm x 1.5 μm, and (d) 0.63 μm x 0.63 μm. As the

pitches are different among these four samples, in the following transmittance spectra, we normalize the magnitude of the transmittance to the density of nanorods.

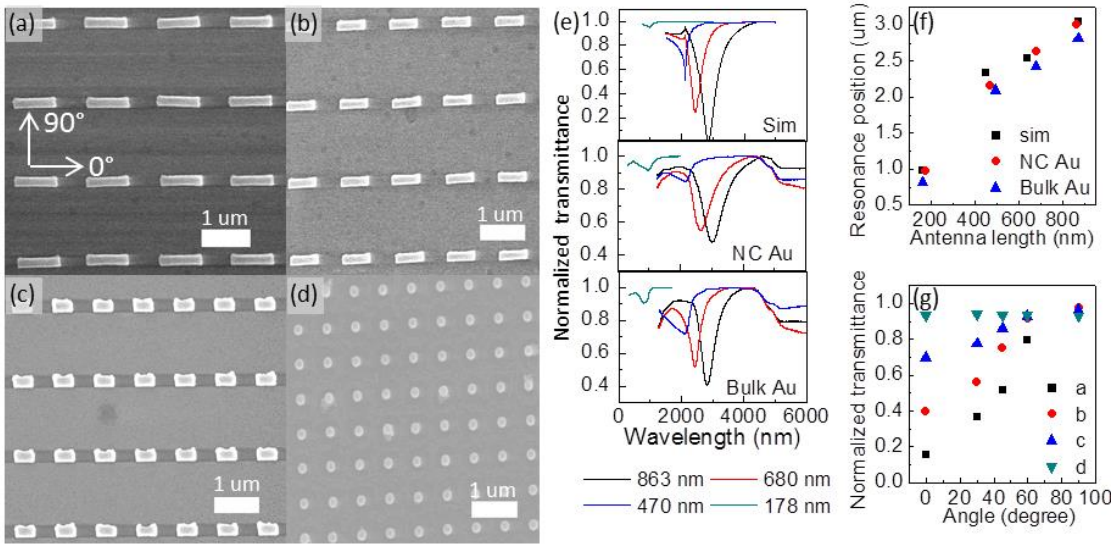

Figure 3-6 SEM images of Au NC-based nano-antenna arrays with length x width of (a) 863 nm x 167 nm, (b) 680 nm x 178 nm, (c) 470 nm x 200 nm, and (d) 178 nm x 178 nm. (e) Normalized transmittance spectra for these Au NC-based nano-antenna arrays from (upper panel) finite-difference frequency-domain simulations and (middle panel) FT-IR measurements. Black, red, blue and green curves correspond to the nano-antenna arrays shown in (a-d). (bottom panel) Comparison to the transmittance spectra for bulk Au nano-antenna arrays of similar sizes: (a) 868 nm x 188 nm, (b) 677 nm x 228 nm, (c) 492 nm x 250 nm, and (d) 185 nm x 185 nm. (f) Resonance position as a function of nano-antenna length for simulated (black) and experimental (red) Au NC-based nano-antenna arrays in comparison to experimental resonances for bulk Au (blue) nano-antenna arrays.

(g) Normalized transmittance at resonance as a function of the angle of linearly polarized incident light for the nano-antenna arrays shown in (a-d).

The nano-antenna length is a major factor in controlling its dipole plasmonic resonance. We apply finite-difference frequency-domain simulations to predict the transmittance spectra for these four samples [Figure 3-6 (e), upper panel]. The dielectric function of SCN-exchanged Au NC thin films is characterized by spectroscopic ellipsometry and used in the simulations [Figure 3-7]. Experimental transmittance spectra of these four samples are collected by Fourier transform infrared (FT-IR) spectroscopy [Figure 3-6 (e), middle panel]. As the nano-antenna length increases from 178 nm to 863 nm, the measured resonance wavelength shifts from 962 nm to 3010 nm, closely matching the simulations. For comparison, bulk gold nano-antenna arrays of similar dimensions are fabricated by electron-beam lithography and thermal evaporation of Au. Their transmittance spectra [Figure 3-6 (e), bottom panel] show resonances varying from 816 nm to 2818 nm. Figure 3-6 (f) plots all the resonance positions as a function of nano-antenna length from simulations and from fabricated Au NC-based and bulk Au nano-antenna arrays. The optical properties of Au NC-based nano-antennas, like bulk Au nano-antennas, red-shift with increasing nanorod length. However, for the same nanorod length, the resonance of Au NC-based nano-antennas are 150 to 190 nm red-shifted and broader compared with those for bulk Au nano-antennas, which arises from the different permittivity associated with the NC-based metal compared to the bulk material.[34]

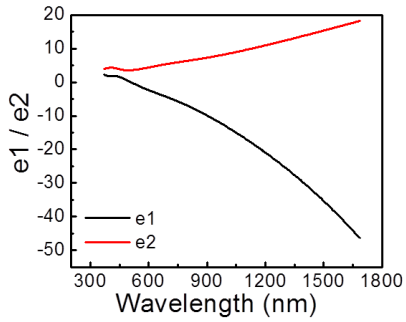

Figure 3-7 The permittivity of a SCN-exchanged Au NC thin film.

Since we fabricate anisotropic nanostructures as building blocks for metasurfaces, we probe their polarization control of incident light. The polarization-dependent transmittance spectra for the four samples in Figure 3-6 (a-d) are shown as a function of the angle of linearly polarized incident light in Figure 3-8. The polarization angle is defined as the angle between the polarization direction and the longitudinal direction of the nanorods [as defined in the inset in Figure 3-6 (a)]. For the anisotropic nanorods [in Figure 3-6 (a-c)], the magnitude of the transmittance at resonance increases and ultimately reaches approximately 100% as the polarization angle of the incident light is rotated from 0 to 90 degrees [Figure 3-6 (g), black, red, and blue symbols]. As expected, there is no polarization dependence [Figure 3-6 (g), green symbol] for the isotropic 178 nm nanopillars [Figure 3-6 (d)]. The magnitude of the polarization sensitivity increases as the aspect ratio of the nanorods is increased. For example, the normalized transmittance varies from 0 for isotropic nanostructures (d), to 25% for (c), 60% for (b), and 80% for

(a) as the aspect ratio of the nanorods increases. This is consistent with the response of similar size nanorods made of bulk Au [Figure 3-9], for which the normalized transmittance increases from 0 to 30%, 70%, and 90% with increasing aspect ratio. We note that, unlike bulk Au nanorods that must be fabricated using a metal adhesion layer, known to deleteriously affect the optical properties,[44,45] NC-based nanorods are advantageously fabricated with ~90% yield without an adhesion layer. Functionalizing the substrate surface with a self-assembled monolayer may provide a route to reduce even further the defect density and increase the polarization conversion efficiency in Au NC-based nanorods.

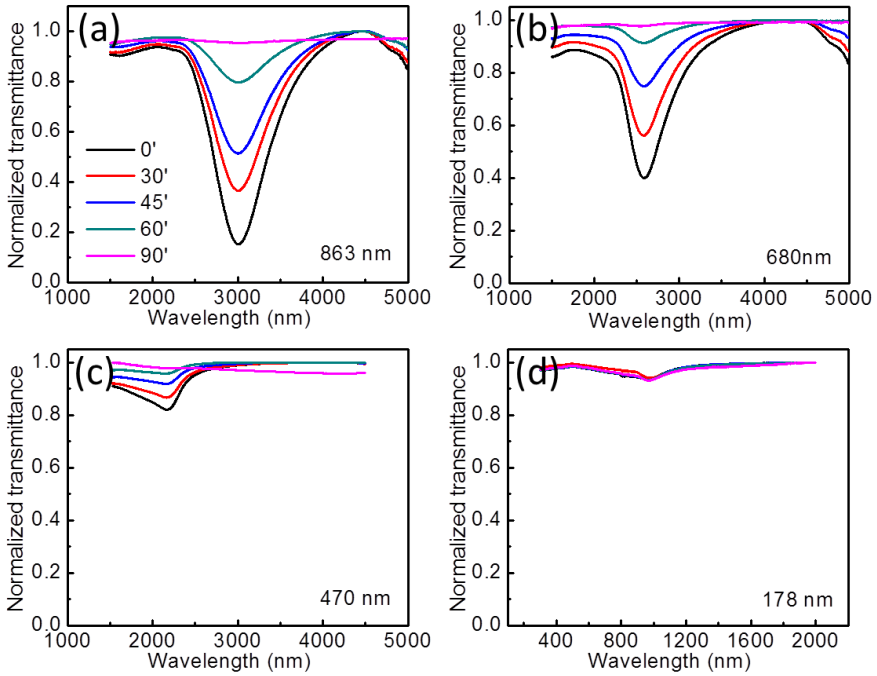

Figure 3-8 Transmittance spectra for linearly polarized illumination of nano-antenna arrays with nanorods of (a) 863 nm, (b) 680 nm, (c) 470 nm and (d) 178 nm lengths. The nano-antenna length is oriented horizontally at zero degrees.

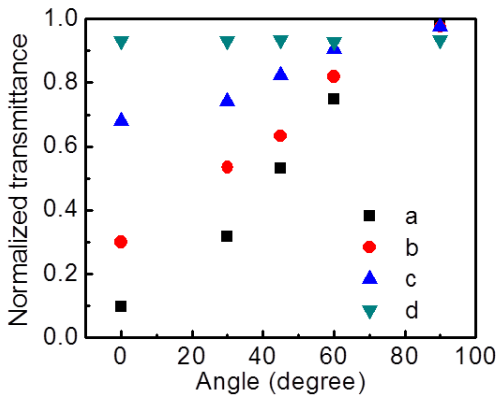

Figure 3-9 Normalized transmittance at resonance as a function of the angle of linearly polarized incident light for the bulk Au nano-antennas with dimensions: (a) 868 nm x 188 nm, (b) 677 nm x 228 nm, (c) 492 nm x 250 nm, and (d) 185 nm x 185 nm.

3-3 Ultrathin metasurface quarter-wave plate

Since Au NC-based nano-antennas can control the polarization of light as do their bulk Au analogs, we exploit Au NC-based nano-anntennas as building blocks of achromatic QWPs [Figure 3-10 (a)] that operate at normal incidence in the near-to-mid-infrared region of the electromagnetic spectrum. To do so, we combine arrays of two different length Au NC-based nanorods and interleave them in an orthogonal fashion on a single substrate.[22] The QWP functionality is achieved as the nanorods along the two orthogonal directions mainly interact with the incident polarization along their longitudinal axis, thus realizing a localized birefringence. The phase difference between the 0 and 90 degree polarized transmitted waves is tailored to be 90 degrees at the desired

wavelength range of operation by controlling the length and thickness of the nanorods as well as the gap between them.

The first design we implemented is a metasurface QWP designed to operate in the mid-IR [Figure 3-10 (a)]. The length (l_i), width (w_i), and period (d_i) of the nanorods oriented in the i=x- and y-directions are: l_x = 800 nm, w_x = 200 nm, and d_x = 1400 nm and l_y = 1000 nm, w_y = 200 nm, and d_y = 1200 nm. All nanorods are 150 nm thick and the gaps between nanorods are 200 nm. Full-wave numerical simulations of the transmittance spectra and phase for linearly polarized light at 0 degrees (along *x*-oriented nanorods) and at 90 degrees (along *y*-oriented nanorods), are shown in Figure 3-10 (b). The corresponding experimental transmittance spectra are shown in Figure 3-11. Simulations show a phase difference close to 90 degrees between the transmitted polarizations [black and red dashed curves in Figure 3-10 (b)], in a wavelength range spanning 2729 nm to 3094 nm. Within this bandwidth of operation, the ratio of transmittance amplitudes for 0 and 90 degree polarization varies, suggesting that the effective fast and slow axes of this QWP rotate as the wavelength changes. Therefore, for incident circularly polarized excitation, the transmitted light will be linearly polarized, but with a polarization angle that depends on the wavelength.

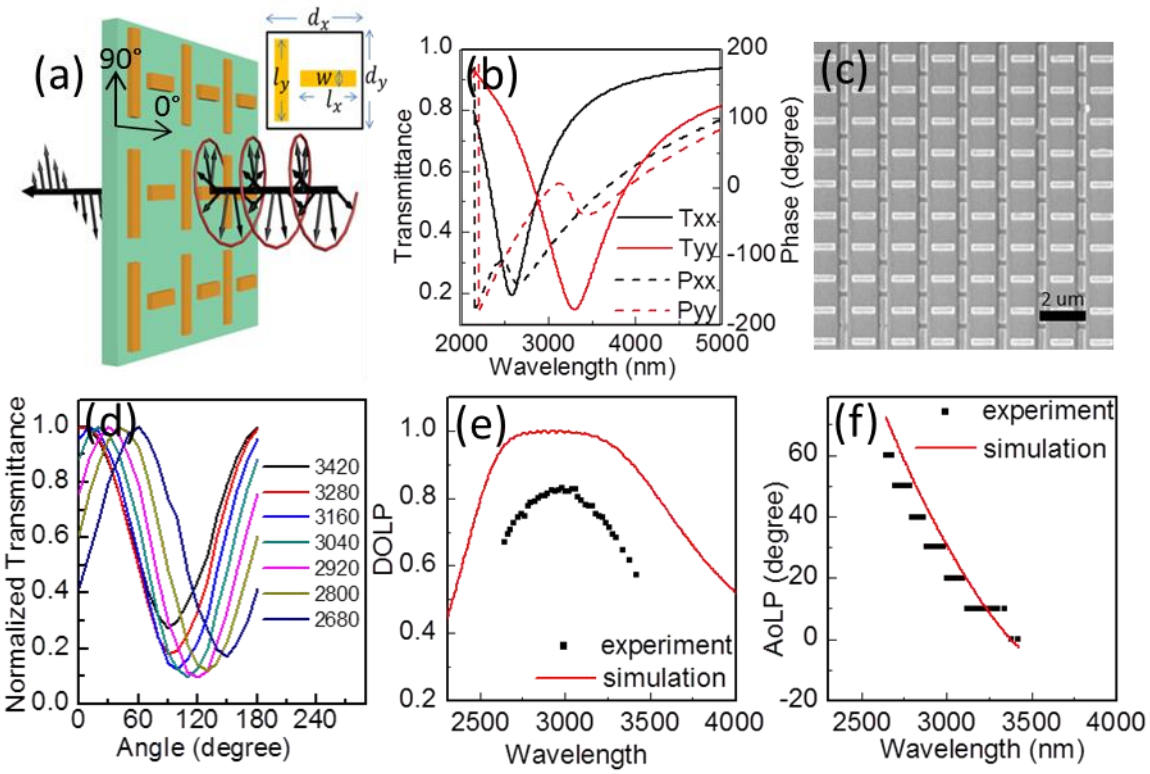

Figure 3-10 (a) Schematic of the design and optical characterization of a metasurface QWP constructed from an orthogonal array of two different size nanorods with length (l_i), width (w_i), and period (d_i) in the i=x- and y-directions. (b) Full wave simulations of the transmittance (solid curve) and phase (dashed curve) for the QWP upon excitation by light linearly polarized at 0 and 90 degrees, along the longitudinal axes of the x-oriented nanorods (black) with l_x = 800 nm, w_x = 200 nm, and d_x = 1400 nm and the y-oriented nanorods (red) with l_y = 1000 nm, w_y = 200 nm, and d_y = 1200 nm. The nanorod thickness is 150 nm; all gaps between nanorods are 200 nm. (c) SEM image of a nanoimprinted, colloidal Au NC-based orthogonal nanorod array fabricated on a glass substrate. (d) Normalized transmitted light intensity as a function of the angle of the second polarizer for different wavelengths of circularly polarized input light. (e) Degree of linear

polarization (DoLP) and (f) angle of linear polarization (AoLP) for circularly polarized input light: simulation (red curve) and experiment result (black dots). The AoLP is collected at a minimum step of 10 degrees.

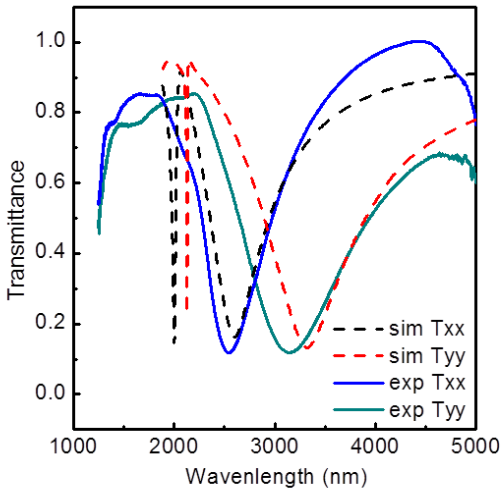

Figure 3-11 Transmittance spectra for the Au NC-based quarter-wave plate excited by light linearly polarized along the x and y directions. Dashed curves: Full wave simulation results; Solid curves: experiment results.

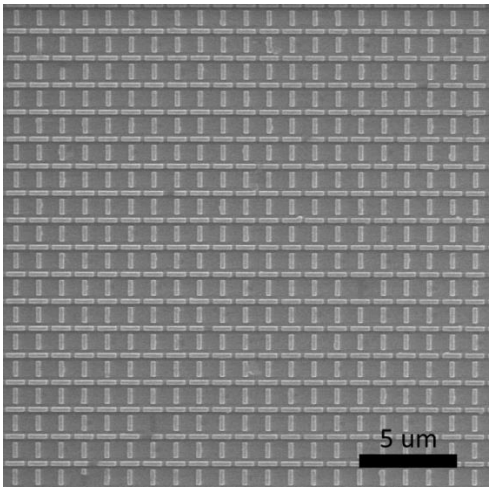

Figure 3-12 An SEM image showing a larger area of the nanoimprinted, colloidal Au NC-based mid-IR quarter-wave plate fabricated on a glass substrate.

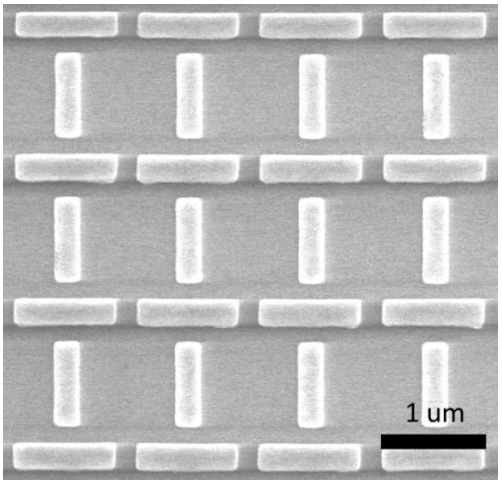

Figure 3-13 A higher resolution SEM image showing the nanoimprinted, colloidal Au NC-based mid-IR quarter-wave plate fabricated on a glass substrate.

To fabricate this mid-IR QWP metasurface by nanoimprinting NC-based nanostructures, we design a master template with orthogonal arrays of interleaved nanorods whose dimensions are: l_x = 970 nm, w_x = 250 nm, and d_x = 1400 nm and l_y = 1130 nm, w_y = 270 nm, and d_y = 1200 nm. As described above, we deposit the Au NCs by spin-coating, then lift off the imprint resist in acetone, and immerse the patterned NC thin film in an acetone solution of thiocyanate. The dimensions of the template are designed to be larger than those of the desired final structures to compensate for shrinkage of the NC-based nanostructures upon ligand exchange. We fabricate the metasurface QWP over a 1.2 mm x 1.2 mm area on a glass substrate. Figure 3-10 (c) shows a SEM image of a nanoimprinted NC-based QWP. Larger-area and higher resolution images of the QWP are shown in Figure 3-12 and Figure 3-13. The dimensions of the fabricated nanorods are measured from SEM images taken from nine different areas of this QWP. The average dimensions of the nanorods are: l_x = 821 nm, w_x = 241 nm, and d_x = 1400 nm and l_y = 964 nm, w_y = 261 nm, and d_y = 1200 nm. Across the large area of the QWP the variations in the dimensions are within 2 - 6%. For nanorods oriented in the *x*- and *y*-direction of the QWP, the LER is 2.9 nm and the misalignment is 0.2° [Table 3-1]. The height of the nanorods is 109 nm, thinner than that in the design, but within tolerance to allow the successful operation and high polarization conversion efficiency of the QWP.

To characterize the optical properties of the Au NC-based QWP, we excite the sample with monochromatic, circularly polarized light generated by passing light from an FT-IR spectrometer through a linear polarizer and then a commercial mid-IR (2800 nm) QWP. A second linear polarizer is placed between the sample and the detector and

rotated from 0 to 180 degrees in steps of 10 degrees to analyze the angular-dependence of the transmitted light at each wavelength. Figure 3-10 (d) shows the normalized transmittance as a function of the angle of the second polarizer. The sinusoidal shape of the angular-dependence of the transmitted light suggests that the output light is linearly polarized to a large degree. The troughs in the sinusoid should be ideally zero, however non-idealities in the dimensions of the nanorod arrays from the designed structure and the less than perfect polarization ability of the commercial mid-IR QWP likely give rise to residual transmittance.

We extract the degree of linear polarization (DoLP) from the measured NC-based QWP optical properties shown in Figure 3-10 (d). The DoLP is defined as $I(\lambda)_{max} - I(\lambda)_{min} \Big/ I(\lambda)_{max} + I(\lambda)_{min}$, where $I(\lambda)_{max}$ and $I(\lambda)_{min}$ are the maximum and minimum in the transmitted light intensity at specific polarization angles for a given wavelength λ. The wavelength-dependent DoLP for the circularly polarized light incident on the fabricated QWP is shown in Figure 3-10 (e) [black dots]. The measurements are in good agreement with simulations of the DoLP for the designed plate [red curve]. The DoLP of the NC-based QWP is sufficiently large (> 0.8) over a wavelength range of 2840 – 3080 nm, which is comparable to that of previously reported QWPs fabricated by electron-beam lithography and metal evaporation.[22] The angle of linear polarization (AoLP) is defined as the polarization angle of the transmitted linearly polarized light for this mid-IR QWP. The wavelength-dependence of the AoLP is extracted from Figure 3-10 (d), and plotted in Figure 3-10 (f) [black dots]. The experimental AoLP is clustered in

lines, limited by the resolution with which we collected the output angle, but closely matches the simulation [red curve].

To broaden the operational wavelength range of the QWP, an extreme bandwidth design is explored [Figure 3-14 (a)], in which vertically-oriented nanorods are extended to form a continuous line with a width of 700 nm, while the horizontally-oriented nanorods are reduced to 500 nm in length.[22,46] The continuous, vertical line effectively moves the nanorod resonance into the far-IR, thus eliminating unwanted phase dispersion from the vertical nanorods in the mid-IR.[22] The short horizontal nanorods introduce phase dispersion in the near-IR and a constant 90 degree difference with respect to the vertically-oriented line at lower wavelengths in the near-to-mid infrared, as shown in Figure 3-14 (b). Without the horizontal nanorods the continuous, vertical metal lines would create a linear polarizer. The ratio of the transmittances for light polarized along the *y*-oriented nanolines to that for light polarized along the *x*-oriented nanorods vary from 1.5 to 0.5, and reaches 1 at 2700 nm, which implies that the effective optical axes overlap at this wavelength. Using the same fabrication methods described above, we fabricate the extreme bandwidth QWP by nanoimprinting of colloidal Au NCs on a glass substrate. Figure 3-14 (c) and Figure 3-15 show SEM images of the fabricated waveplate. The dimensions of the nanorods oriented in the *x*-direction are: l_x = 469 nm; w_x = 178 nm, and d_x = 1600 nm and of the nanoline in the *y*-direction are: w_y = 641. The gap between nanorods is 245 nm and their thickness is 80 nm. The LER and misalignment are 4.5 nm and 0.6° for the *x*-oriented nanorods and are 7 nm and 0.1° for the *y*-oriented nanolines

[Table 3-1]. This is the first experimental realization of an extreme bandwidth metasurface QWP based on our orthogonal nanorod design.

To characterize the mid-IR waveplate in Figure 3, we generate circularly polarized light using a commercial QWP and analyze the linearly polarized transmitted light through our sample. However, there are no available commercial mid-IR QWPs that have the extreme bandwidths realized by our design in Figure 3-14 to provide circularly polarized incident light. Therefore, in order to characterize the optical properties of the extreme bandwidth QWP, we excite the sample with light linearly polarized along angles varying from 0 to 90 degrees in steps of 5 degrees. This is achieved by placing and rotating a broadband linear polarizer between the source and the sample. A second linear polarizer is positioned behind the sample and before the detector to record the angular-dependence of the amplitude of the transmitted light. In theory, if linearly polarized incident light has the same components on the effective fast and slow axes of the sample, the transmitted light will be circularly polarized. Since we do not know where the effective fast and slow axes are for each wavelength, we test all possible angles for the incident light, and then pick out the transmitted light with the smallest DoLP at each wavelength. The intensity of transmitted light with the smallest DoLP at different wavelengths is plotted in Figure 3-14 (d) as a function of the angle of the second polarizer. The DoLP for these spectra are plotted in Figure 4 (e) [black dots]. There is an extreme, broad wavelength range (2500 – 4700 nm) over which the DoLP is remarkably small. This working wavelength range agrees well with the full-wave simulation [red curve] where a near zero DoLP starts at 2500 nm and extends to 5000 nm. The difference

in the DoLPs between experiment and simulation likely arises from variations in the nanorod dimensions. For the extreme bandwidth QWP, the corresponding AoLP is defined as the angle of the 1st polarizer for which the DoLP is minimum [Figure 3-14 (f)]. Simulations [red curve] and experiments [black dots] agree well, and highlight the expected dispersion of the fast and slow axes over the bandwidth of operation for this extreme bandwidth QWP.

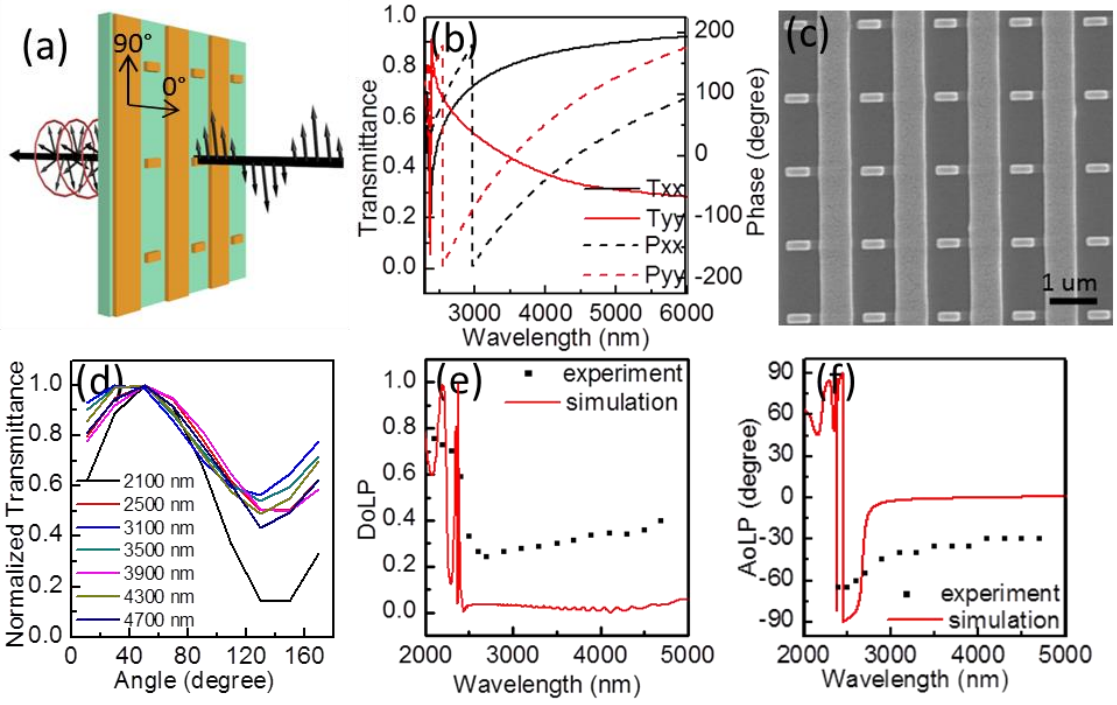

Figure 3-14 (a) Schematic of the design and optical characterization of an extreme bandwidth, metasurface QWP constructed from a short nanorod and a continuous line. (b) Full wave simulations of the transmittance (solid curve) and phase (dashed curve) for the extreme bandwidth, QWP upon excitation by light linearly polarized at 0 and 90 degrees,

along the longitudinal axes of the short, *x*-oriented nanorod (black) with l_x = 500 nm, w_x = 200 nm, and d_x = 1600 nm and the *y*-oriented nanoline (red) with w_y = 700 nm. The thickness is 150 nm; all gaps between *x*-oriented nanorod and *y*-oriented nanoline are 200 nm. (c) SEM image of a nanoimprinted, colloidal Au NC-based extreme bandwidth QWP on glass substrate. (d) Normalized transmitted light as a function of the angle of the second polarizer for different wavelengths of linearly polarized input light. (e) Degree of linear polarization (DoLP) and (f) angle of linear polarization (AoLP) for linearly polarized input light: simulation (red curve) and experiment (black dots).

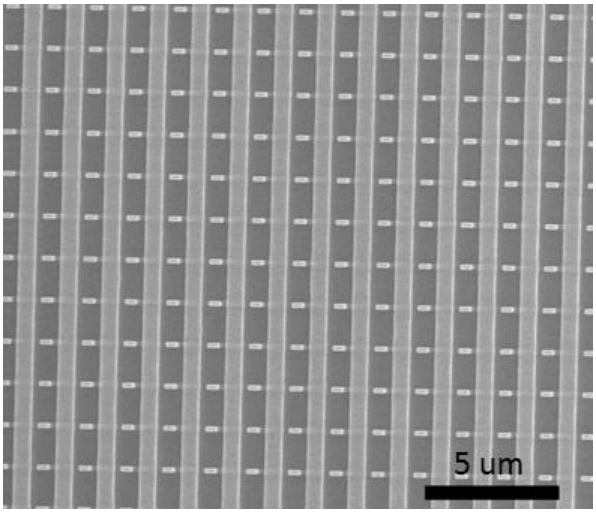

Figure 3-15 An SEM image showing a larger area of the nanoimprinted colloidal Au NC-based extreme bandwidth quarter-wave plate fabricated on a glass substrate.

3-4 Conclusions

In summary, we have demonstrated a fast, large-area, solution-based fabrication method for size-tunable nanocrystal-based nanoantennas and exploited their plasmonic resonance and their polarization sensitivity to fabricate ultrathin metasurfaces that operate as near-to-mid infrared QWPs. The fabrication of Au NC-based plasmonic nanostructures provides a promising route to scalable manufacturing of more complex, optical metamaterial devices, such as plasmonic biosensors, meta-lenses, holography plates, and optical nanocircuits.

3-5 References

(1) Chen, W.; Tymchenko, M.; Gopalan, P.; Ye, X.; Wu, Y.; Zhang, M.; Murray, C. B.; Alu, A.; Kagan, C. R. *Nano Lett.* **2015**, *15*, 5254–5260.

(2) Soukoulis, C. M.; Wegener, M. *Nat. Photonics* **2011**, *5*, 523–530.

(3) Shalaev, V. M. *Nat. Photonics* **2007**, *1*, 41–48.

(4) Zheludev, N. I.; Kivshar, Y. S. *Nat. Mater.* **2012**, *11*, 917–924.

(5) Haug, F. J.; Söderström, T.; Cubero, O.; Terrazzoni-Daudrix, V.; Ballif, C. *J. Appl. Phys.* **2008**, *104*.

(6) Shen, H.; Bienstman, P.; Maes, B. *J. Appl. Phys.* **2009**, *106*.

(7) Le, F.; Brandl, D. W.; Urzhumov, Y. a.; Wang, H.; Kundu, J.; Halas, N. J.;

Aizpurua, J.; Nordlander, P. *ACS Nano* **2008**, *2*, 707–718.

(8) Adato, R.; Yanik, A. a; Amsden, J. J.; Kaplan, D. L.; Omenetto, F. G.; Hong, M. K.; Erramilli, S.; Altug, H. *Proc. Natl. Acad. Sci. U. S. A.* **2009**, *106*, 19227–19232.

(9) Bakker, R. M.; Yuan, H. K.; Liu, Z.; Drachev, V. P.; Kildishev, A. V.; Shalaev, V. M.; Pedersen, R. H.; Gresillon, S.; Boltasseva, A. *Appl. Phys. Lett.* **2008**, *92*.

(10) Zhang, Y.; Aslan, K.; Previte, M. J. R.; Malyn, S. N.; Geddes, C. D. *J. Phys. Chem. B* **2006**, *110*, 25108–25114.

(11) Saboktakin, M.; Ye, X.; Chettiar, U. K.; Engheta, N.; Murray, C. B.; Kagan, C. R. *ACS Nano* **2013**, *7*, 7186–7192.

(12) Li, J.; Fattal, D.; Li, Z. *Appl. Phys. Lett.* **2009**, *94*, 2007–2010.

(13) Shen, C.; Hui, C.; Yang, T.; Xiao, C.; Tian, J.; Bao, L.; Chen, S.; Ding, H.; Gao, H. *Chem. Mater.* **2008**, *20*, 6939–6944.

(14) Stewart, M. E.; Anderton, C. R.; Thompson, L. B.; Maria, J.; Gray, S. K.; Rogers, J. a.; Nuzzo, R. G. *Chem. Rev.* **2008**, *108*, 494–521.

(15) Lu, H.; Liu, X.; Mao, D.; Wang, G. *Opt. Lett.* **2012**, *37*, 3780–3782.

(16) Knight, M. W.; Sobhani, H.; Nordlander, P.; Halas, N. J. *Science* **2011**, *332*, 702–704.

(17) Atwater, H. a; Polman, A. *Nat. Mater.* **2010**, *9*, 205–213.

(18) Bai, W.; Gan, Q.; Song, G.; Chen, L.; Kafafi, Z.; Bartoli, F. *Opt. Express* **2010**, *18*, A620–A630.

(19) Ni, X.; Ishii, S.; Kildishev, A. V; Shalaev, V. M. *Light Sci. Appl.* **2013**, *2*, e72.

(20) Chen, X.; Huang, L.; Mühlenbernd, H.; Li, G.; Bai, B.; Tan, Q.; Jin, G.; Qiu, C.-W.; Zhang, S.; Zentgraf, T. *Nat. Commun.* **2012**, *3*, 1198.

(21) Aieta, F.; Genevet, P.; Kats, M. a; Yu, N.; Blanchard, R.; Gaburro, Z.; Capasso, F. *Nano Lett.* **2012**, *12*, 4932–4936.

(22) Zhao, Y.; Aluì, A. *Nano Lett.* **2013**.

(23) Yu, N.; Aieta, F.; Genevet, P.; Kats, M. a; Gaburro, Z.; Capasso, F. *Nano Lett.* **2012**, *12*, 6328–6333.

(24) Ellenbogen, T.; Seo, K.; Crozier, K. B. *Nano Lett.* **2012**, *12*, 1026–1031.

(25) Jiang, Z. H.; Lin, L.; Ma, D.; Yun, S.; Werner, D. H.; Liu, Z.; Mayer, T. S. *Sci. Rep.* **2014**, *4*, 7511.

(26) Yu, N.; Genevet, P.; Kats, M. a; Aieta, F.; Tetienne, J.-P.; Capasso, F.; Gaburro, Z. *Science* **2011**, *334*, 333–337.

(27) Huang, L.; Chen, X.; Mühlenbernd, H.; Li, G.; Bai, B.; Tan, Q.; Jin, G.; Zentgraf, T.; Zhang, S. *Nano Lett.* **2012**.

(28) Huang, L.; Chen, X.; Mühlenbernd, H.; Zhang, H.; Chen, S.; Bai, B.; Tan, Q.; Jin, G.; Cheah, K.-W.; Qiu, C.-W.; Li, J.; Zentgraf, T.; Zhang, S. *Nat. Commun.* **2013**,

4, 2808.

(29) Ni, X.; Kildishev, A. V.; Shalaev, V. M. *Nat. Commun.* **2013**, *4*, 1–6.

(30) Chou, S. Y.; Krauss, P. R.; Renstrom, P. J. *Science (80-.).* **1996**, *272*, 85–87.

(31) Boltasseva, A. *J. Opt. A Pure Appl. Opt.* **2009**, *11*, 114001.

(32) Lucas, B. D.; Kim, J.-S.; Chin, C.; Guo, L. J. *Adv. Mater.* **2008**, *20*, 1129–1134.

(33) Henzie, J.; Lee, M. H.; Odom, T. W. *Nat. Nanotechnol.* **2007**, *2*, 549–554.

(34) Fafarman, A. T.; Hong, S.-H.; Caglayan, H.; Ye, X.; Diroll, B. T.; Paik, T.; Engheta, N.; Murray, C. B.; Kagan, C. R. *Nano Lett.* **2013**, *13*, 350–357.

(35) Fafarman, A. T.; Hong, S. H.; Oh, S. J.; Caglayan, H.; Ye, X.; Diroll, B. T.; Engheta, N.; Murray, C. B.; Kagan, C. R. *ACS Nano* **2014**, *8*, 2746–2754.

(36) Ahn, S. H.; Guo, L. J. *Adv. Mater.* **2008**, *20*, 2044–2049.

(37) Liang, C.-C.; Liao, M.-Y.; Chen, W.-Y.; Cheng, T.-C.; Chang, W.-H.; Lin, C.-H. *Opt. Express* **2011**, *19*, 4768–4776.

(38) You, E. A.; Zhou, W.; Suh, J. Y.; Huntington, M. D.; Odom, T. W. *ACS Nano* **2012**, *6*, 1786–1794.

(39) Peng, S.; Lee, Y.; Wang, C.; Yin, H.; Dai, S.; Sun, S. *Nano Res.* **2008**, *1*, 229–234.

(40) Jung, G. Y.; Wu, W.; Ganapathiappan, S.; Ohlberg, D. A. A.; Saif Islam, M.; Li, X.; Olynick, D. L.; Lee, H.; Chen, Y.; Wang, S. Y.; Tong, W. M.; Williams, R. S.

Appl. Phys. A **2005**, *81*, 1331–1335.

(41) Ko, S. H.; Park, I.; Pan, H.; Grigoropoulos, C. P.; Pisano, A. P.; Luscombe, C. K.; Fréchet, J. M. J. *Nano Lett.* **2007**.

(42) Maier, S. A. *Plasmonics: Fundamentals and Applications*; 1st ed.; Springer: New York, 2007.

(43) Alù, A.; Engheta, N. *Phys. Rev. Lett.* **2008**, *101*, 1–4.

(44) Habteyes, T. G.; Dhuey, S.; Wood, E.; Gargas, D.; Cabrini, S.; Schuck, P. J.; Alivisatos, a. P.; Leone, S. R. *ACS Nano* **2012**, *6*, 5702–5709.

(45) Zhao, Y.; Belkin, M. a.; Alù, A. Twisted optical metamaterials for planarized ultrathin broadband circular polarizers. *Nature Communications*, 2012, *3*, 870.

(46) Zhao, Y.; Alù, A. *Phys. Rev. B* **2011**, *84*, 205428.

Chapter 4 Hydrogel-covered Au nanorod array optical moisture sensor for agricultural use

Significant components of this chapter will be submitted as "Hydrogel-Covered Au Nanorod Array Optical Moisture Sensor for Agricultural Use" by Wenxiang Chen, Gaoxiang Wu, Mingliang Zhang, Nicholas J. Greybush, Jordan P. Howard-Jennings, Naixin Song, Shu Yang, Cherie R. Kagan.

Growing water scarcity is one of the world's leading challenges to sustainable food production, according to the United Nations Food and Agriculture Organization [1]. Agricultural water withdrawal accounts for 70% of the global sum of all water use [2]. To manage water use through efficient irrigation scheduling, agricultural professionals and scientists have developed different methods for gathering soil moisture information. Point detection methods include time domain reflectometry [3,4], time domain transmission (TDT) sensors [5,6], capacitance sensors [7] and wireless sensor networks (usually composed of capacitance sensors and TDT sensors) [6,8,9]. However, they provide limited spatial coverage [10,11], since measurements at a large number of locations are laborious and installing networks across the large area of fields is expensive. On a regional scale (a few square kilometers or more), methods such as passive microwave remote sensing [12,13] and airborne and spaceborne active microwave remote sensing are used [14–17]. However, these techniques are usually expensive, undersample the landscape, have low signal to noise,

and the accuracy of microwave methods is significantly influenced by soil roughness [10,15].

In recent years, the fast development of unmanned aerial vehicles (UAVs) is providing farmers with low-cost agriculture drones which are excellent at imaging fields in the visible and near infrared (NIR) with resolutions up to a few centimeters [18]. An environmentally friendly, unpowered optical moisture sensor that can cooperate with drones to report soil moisture remotely is highly desirable to enable intelligent farming practices. Hydrophilic polymers such as hydrogels have been structured to build photonic crystals for optical humidity sensing, but their open frameworks make them mechanically fragile and they require the fabrication of multiple layers to create high reflectivity [19–26]. Plasmon resonance-based humidity sensors, on the other hand, are more robust and have greater reflectivity and therefore increased signal/noise ratios. Various humidity-sensitive materials, such as carbon, hydrogel fiber, mercaptopoly(ethylene glycol) (mercaptoPEG) and myoglobin, have been ligated to or physically mixed with plasmonic nanoparticles such that upon exposure to humidity there is a change in the interparticle spacing and/or the effective dielectric constant of the surroundings, leading to a shift in the plasmonic resonance peak [27–30]. But these sensors suffer from problems including large variations in spectral shifts due to the irregular arrangement of the nanoparticles, small measurement areas, large hysteresis, and limited operation conditions that require high relative humidity (RH) (RH > 80%). So far, none of these sensors have been studied for soil moisture monitoring.

Here, we report a low-cost, high reflectivity optical sensor, which is suitable for large-area soil moisture monitoring. The sensor is created by coating hydrogel films on top of an ultrathin, plasmonic Au nanorod (NR) array taking advantage of the high-reflectivity, localized surface plasmon resonance (LSPR) of the Au NR array [31–33]. It operates by transducing refractive index changes of the hydrogel upon exposure to moisture into spectral shifts [34,35], as large as 93 nm. We show the sensor operates across a wide range of RH from 24% to 87%. Fast recovery time, within minutes, is achieved by decreasing the hydrogel film thickness to 0.64 μm. The operational wavelength of the sensor, defined by the size of the Au NR array, is tuned from the near to mid-IR to match the transparency window of water. We define a figure of merit (FOM) for sensor performance that describes the magnitude of the LSPR resonance shift in comparison to its bandwidth and use the FOM to characterize sensors designed to operate at different wavelengths. We demonstrate robust sensor operation on the surface of soil and show that tilting the sensor to simulate soil roughness leads to a small variation in resonance wavelength (± 1 nm). These hydrogel-covered Au NR array optical sensors pave the way to distributed sensors for high-spatial and temporal resolution, remote monitoring of soil moisture across the large acreage of fields using drone technology.

4-1 Fabrication of hydrogel-covered Au nanorod array optical moisture sensor

The fabrication of the hydrogel-covered, Au NR array optical moisture sensor is shown in Figure 4-1 (a). To prepare the hydrogel precursor, 200 μL acrylic acid, 2 mL 2-

hydroxyethyl methacrylate, and 30 μL of the photoinitiator 2-hydroxy-2-methylpropiophenone are mixed in a glass vial. The mixture is then exposed to UV light (365 nm, 97435 Oriel Flood Exposure Source, Newport Corp.) three times at a dosage of 500 mJ/cm^2 each time to partially polymerize the monomers. An additional 20 μL 2-hydroxy-2-methylpropiophenone and 40 μL of the crosslinker, ethylene glycol dimethacrylate, are added into the mixture to form the hydrogel precursor.

We choose electron-beam lithography and Au thermal evaporation to prototype different sensor designs. Figure 4-1 (b) shows a scanning electron microscope (SEM) image of an example array of Au NRs that are 362 ± 4 nm in length, 238 ± 3 nm in width, and 32 ± 1 nm in thickness. The corresponding transmittance spectrum of the pristine Au NR array, before spin coating of hydrogel, has an LSPR at 1532 nm (Figure 4-2 (a)).

Hydrogel precursor is spin-coated onto the Au NR array to form thin films (thickness of 0.64 μm and 2.46 μm) and by drop-casting between glass plates separated by a spacer to form a thick film (600 μm). Then it is kept in a transparent plastic container filled with N_2 and exposed to 2000 mJ/cm^2 of UV light (365 nm, 97435 Oriel Flood Exposure Source, Newport Corp.). The hydrogel film thicknesses of 0.64 μm and 2.46 μm are measured by atomic force microscope (AFM) as shown in Figure 4-2 (b - e), and the film of 600 μm thickness is measured with calipers. The cured hydrogel-covered Au NR moisture sensor is soaked in DI water (pH = 6) for 12 h to dissolve any remaining acid and un-crosslinked hydrogel monomers. pH = 6 buffer is dissolved in DI water to a 60 mg/mL concentration to keep the same ionic strength for all sensors.

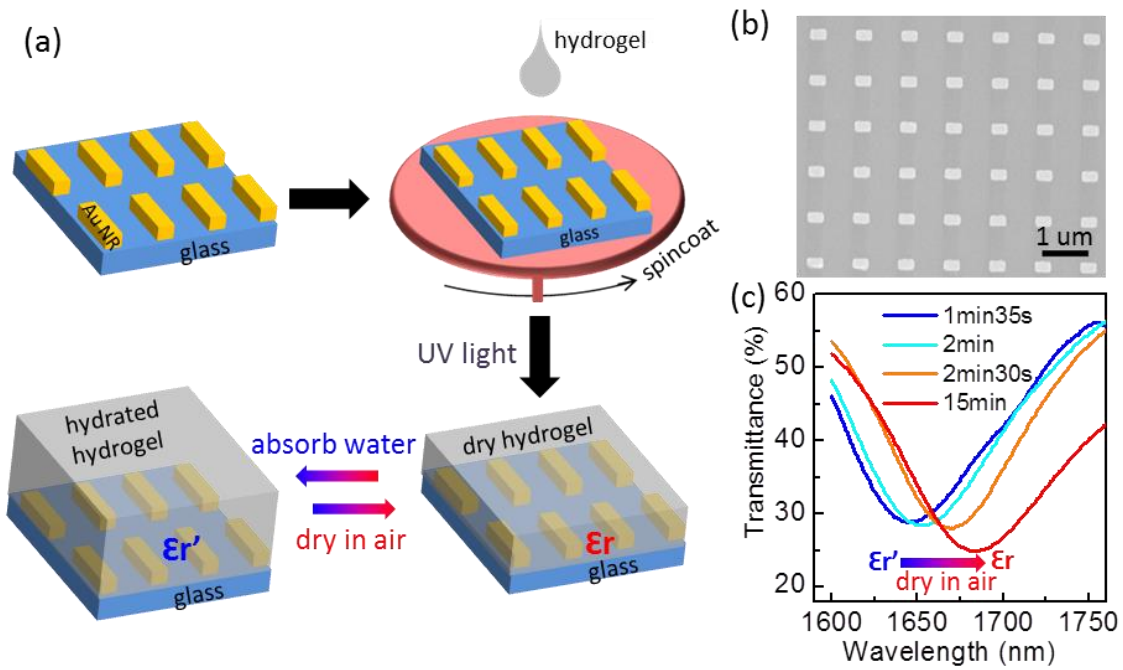

Figure 4-1 Fabrication and characterization of hydrogel-covered Au NR array optical moisture sensor. (a) Schematic of the hydrogel-covered Au NR array optical moisture sensor fabrication process. (b) SEM image of a Au NR array where each NR has a length of 362 ± 4 nm, width of 238 ± 3 nm, and thickness of 32 ± 1 nm (standard deviation). (c) Transmittance spectra for a hydrogel-covered Au NR array optical moisture sensor as a function of time after it is removed from water (pH = 6) and placed in air (RH = 30% and T = 23 ^{o}C).

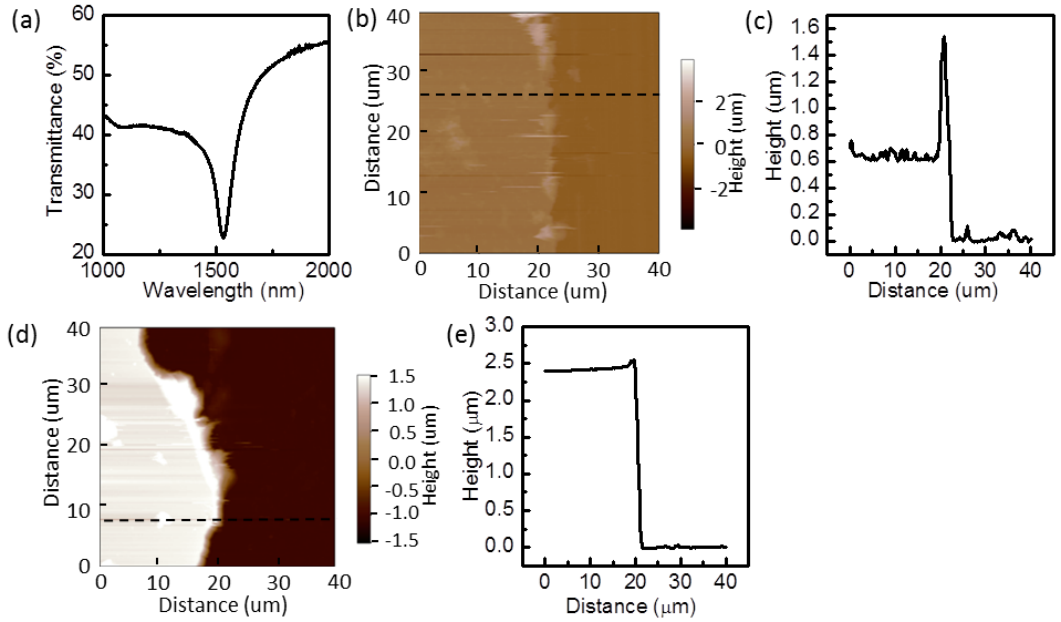

Figure 4-2 (a) Transmittance spectrum for a Au NR array on a glass substrate without any hydrogel coating. The dimensions of the Au NRs in the array are 362 ± 4 nm in length, 238 ± 3 nm in width, and 32 ± 1 nm in thickness. (b, d) Atomic force microscopy (AFM) images and line cut analysis used to characterize hydrogel thin films with (b, c) 0.64 ± 0.03 μm and (d, e) 2.44 ± 0.02 μm thickness coated on top of a Au NR array.

4-2 Characterization of the sensor response in air of different relative humidity and its recovery and response times

To characterize the optical response of the sensors as a function of their water content, we soak the sensors in water at pH = 6, and take them out and measure their transmittance as a function of time as the water evaporates in air at a constant RH and temperature (T). Air RH is measured by a commercial humidity sensor integrated in the

measurement setup (Figure 4-3). Figure 4-1 (c) shows the optical responses of a typical Au NR array covered with a 0.64 μm thick hydrogel film as the water in the hydrogel evaporates at RH = 30% and T = 23 ^{o}C. Since water has a lower refractive index (RI, n = 1.33) than pure hydrogel (n = 1.45), the RI of the hydrogel increases as water evaporates, resulting in a red-shift in the LSPR of the Au NR array from 1646 nm to 1685 nm. From fully soaked to dry (30% RH air), the sensor resonance maintains a transmittance amplitude of 33.5% ± 2.1% and a full width at half-maximum (FWHM) of 118 ± 25 nm.

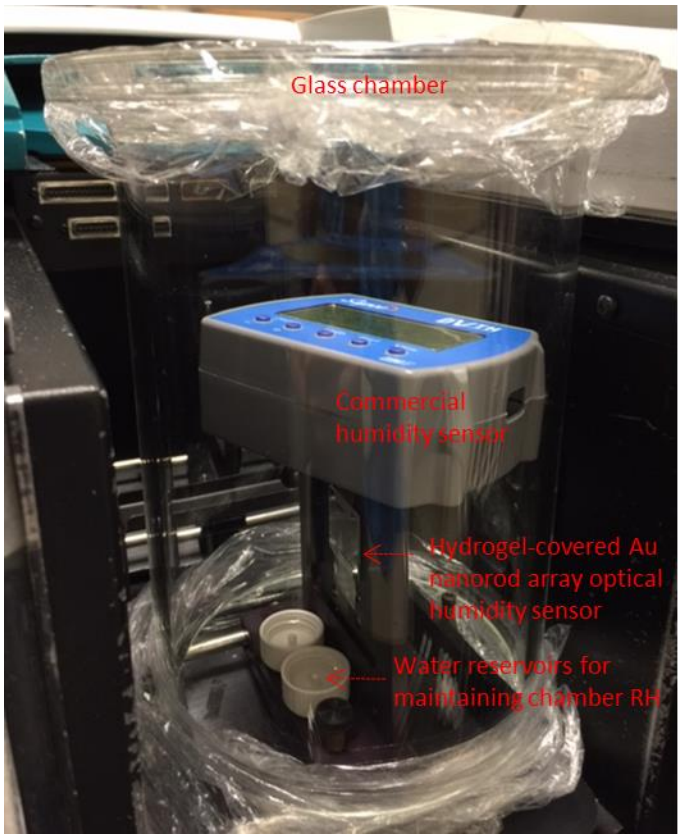

Figure 4-3 Experimental setup used to characterize the optical response of hydrogel-covered Au NR moisture sensors. The hydrogel-covered Au NR array moisture sensor, a commercial humidity sensor and reservoirs of water are enclosed in a 2.5 L glass chamber. RH in the chamber is adjusted by changing the volume of the water reservoirs.

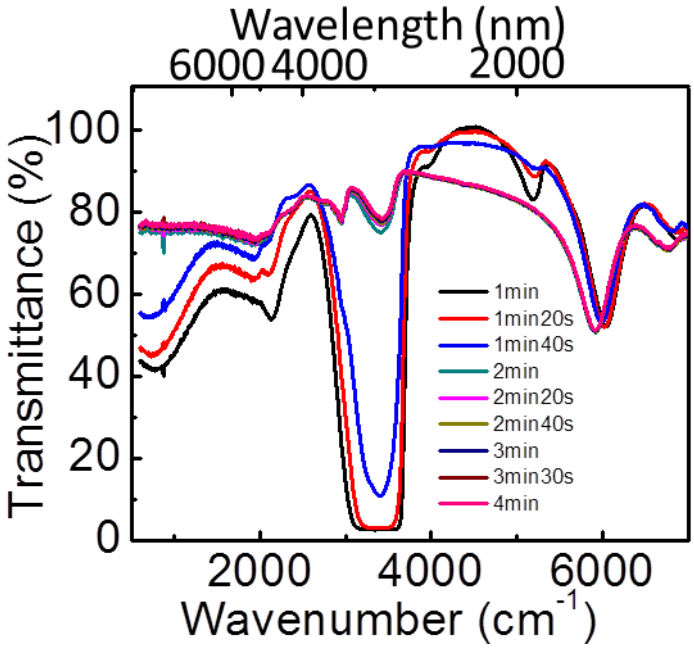

Figure 4-4 Fourier transform infrared (FTIR) spectroscopy measurements for the hydrogel-covered Au NR array moisture sensor as it dries in air held at a RH = 3% and T = 23 ^{o}C after soaking in water (pH = 6). Time is measured from the moment the sensor is taken out of water.

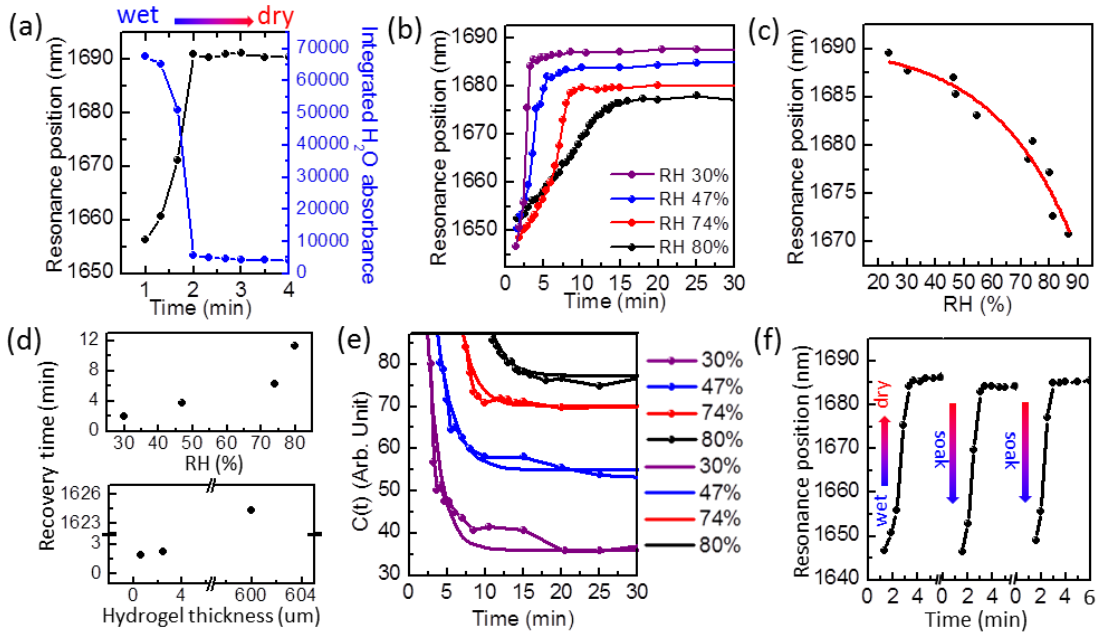

Figure 4-5 Response dynamics of the hydrogel-covered Au NR optical moisture sensor. (a) Wavelength of the localized surface plasmon resonance and integrated intensity of the water stretch region (2530 cm^{-1} - 3845 cm^{-1}) in FTIR spectra from the hydrogel-covered Au NR optical moisture sensor, as it dries over time from the fully soaked in water (pH = 6) to RH = 3%, T = 23 ^{o}C. (b) Sensor resonance position as a function of drying time from fully soaked in water (PH = 6) to steady state in 30%, 47%, 74% and 80% RH air. (c) Steady state sensor resonance positions in different static RH environments. (d) [top] Sensor recovery time extracted from resonance position curves in (b); [bottom] and the recovery time from fully soaked to 30% RH for sensors with different thickness hydrogel films. (e) Resonance position curves in (b) are converted to concentration of water (dotted lines) based on the calibration curve in (c) and Equation (4). Time-dependent concentration curves are fit to Equation (5) (solid lines). (f) Sensor

resonance position for three cycles of soaking in water (pH = 6) and drying in 30% RH measured on three different calendar days.

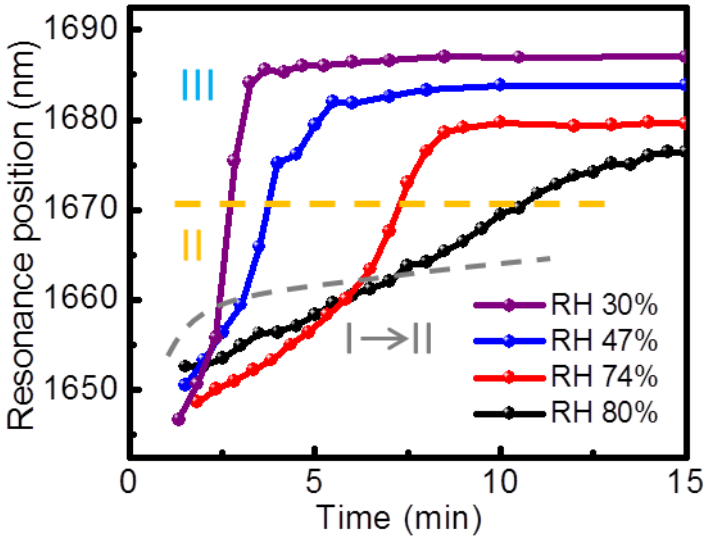

Figure 4-6 Enlargement of the short time rise of the resonance curves in Figure 4-5 (b), as the sensor dries in air of different RH after soaking in water (pH = 6). Stages I, II, and III are labeled to identify the three stages used to describe the sensor recovery process. The transition stage from Stage I to Stage II is identified by the change in the slopes of the transients at short times and the grey dashed line is drawn as a guide. Stage II is between the grey and orange dashed lines. The orange dashed line is defined by the wavelength where our mathematic model (Equation (5)) for Stage III starts to deviate from the experiment data. Stage III exists for times beyond the orange dashed line.

To confirm the working mechanism of the sensor, we correlate the spectral shift of the LSPR of the Au NR array with the water content in the hydrogel. The water content is characterized by integrating the water fingerprint regions (2530 cm^{-1} - 3845 cm^{-1}) in transmittance spectra of the sensor collected using Fourier transform infrared (FTIR) spectroscopy (Figure 4-4). The red-shift in the LSPR of the sensor maps the decrease in water content (Figure 4-5 (a)), confirming the basis of sensor operation.

RH describes the moisture content in air. In experiment a fully soaked sensor is held in air of different RH and its LSPR is monitored as water evaporates until it reaches steady state (Figure 4-5 (b)). The steady state resonance position (λ_{ss}) as a function of RH is plotted in Figure 4-5 (c) (black dots). As RH increases from 24% to 87%, the sensor λ_{ss} shifts from 1688.7 ± 2.3 nm to 1670.9 ± 2.3 nm. We fit the λ_{ss} dependence on RH by an empirical function

$$\lambda_{ss} = \lambda_{dry} - \Delta\lambda \exp\left(-\frac{1-RH}{B}\right) \quad (1)$$

where B = 0.27 is a constant related to both the moisture absorbing ability of the hydrogel and the NRs' sensitivity to the environmental RI change, λ_{dry} = 1690.6 nm is the resonance wavelength at approximately RH = 0 (since $\lambda_{dry} \gg \Delta\lambda \exp\left(-\frac{1}{B}\right)$), and $\Delta\lambda$ = 31.8 nm is approximately the resonance variation from RH = 0 to 100%. $\Delta\lambda$ is consistent with theoretical predictions of the LSPR resonance shift with similar variation in the RI of the surroundings for Au nanobar arrays [36]. The standard deviation in λ_{ss} is 4.5% RH, noting the commercial humidity reference sensor RH accuracy is 2% and experimentally limits the RH determination of the hydrogel-covered Au NR array moisture sensor. The

sensor sensitivity is described in terms of frequency by $\Delta\nu/\nu_{dry} \approx \Delta\lambda/(\lambda_{dry} - \Delta\lambda)$ = 0.019, where $\Delta\nu$ is the sensor LSPR frequency variation from RH = 100% to 0% and ν_{dry} is the sensor LSPR frequency at RH = 0.

The recovery time, defined as the time needed for a fully soaked sensor to reach 90% of λ_{ss}, is calculated from Figure 4-5 (b) and increases from 1.9 min to 11.3 min as the air RH increases from 30% to 80% (upper panel of Figure 4-5 (d)). A three stage model is used to explain the recovery process (Figure 4-5 (b) is enlarged in Figure 4-6 to highlight each stage). In Stage I, water at the hydrogel surface evaporates. In this stage, the sensor resonance does not change. We typically do not capture this stage as we are limited by the time it takes to setup the sensor for measurement. In Stage II, water inside the hydrogel evaporates into air, the hydrogel shrinks, and the resonance begins to shift toward longer wavelengths. In Stage III, the water remaining inside the hydrogel becomes a minority component and the hydrogel thickness remains unchanged. The water concentration inside the hydrogel and therefore the resonance position gradually approach steady state depending on the RH of the environment. Since water in higher RH environments evaporates more slowly, the slope of the resonance curve for higher RH is smaller, analogous to the RH-dependent rate of transpiration in plants [37,38].

In Stage III, the water remaining inside the hydrogel becomes a minority component and the hydrogel thickness, h, remains unchanged. The diffusion coefficient for water in hydrogel is $D = 5.5 \times 10^{-10}\ m^2/s$ [39], and the time needed for water to diffuse through the thickness of hydrogel is $h^2/4D$. For $h = 0.64\ \mu m$, $h^2/4D = 1.9 \times 10^{-4}\ s$, which is much smaller than the time scale of the recovery

process. As a result, water exchange between the hydrogel surface and the hydrogel bulk is much faster than that between the hydrogel surface and the air, and the water concentration inside the hydrogel in Stage III can be approximated as uniformly distributed. We assume that water adsorption and desorption processes only occur within a small distance d of the hydrogel surface. We use the two-dimensional Langmuir adsorption model to describe the water exchange kinetics at the hydrogel surface and scale the surface water concentration by the thickness of hydrogel, consistent with the fast diffusion and approximately uniform distribution of water in the hydrogel. Since water is a minority component in the hydrogel through Stage III, the concentration of empty sites at the hydrogel surface is approximately constant. The rate equation describing the change in water concentration in the hydrogel can be written as:

$$\frac{dC(t)}{dt}h = k_{ad} \cdot RH \cdot p_{sat} \cdot C_e - k_d \cdot C(t) \cdot d \qquad (2)$$

where $C(t)$ is the time-dependent concentration of water in the hydrogel per unit volume, k_{ad} and k_d are the water adsorption and desorption rate constants at the hydrogel-air interface in a unit area, p_{sat} is the water saturation pressure in air at T = 23 ^{o}C, and C_e is the concentration of empty sites at the hydrogel surface. It is important to identify the units of different parameters: $C(t)$ is expressed in mol/m^{-3}, C_e is expressed in mol/m^{-2}, h and d are in unit of m, and p_{sat} is expressed in Pa. As a result, k_{ad} and k_d have the units of $(s \cdot Pa)^{-1}$ and s^{-1}, respectively. For convenience, we define two new parameters $k_{on} = k_{ad} \cdot p_{sat} \cdot C_e$ and $k_{off} = k_d \cdot d$ that represent the constants in the equation:

$$\frac{dC(t)}{dt}h = k_{on}RH - k_{off}C(t) \quad (3)$$

At steady state, the adsorption rate of water equals the evaporation rate of water:

$$k_{on}RH = k_{off}C_{ss} \quad (4)$$

where constant C_{ss} represents the concentration of water in hydrogel at steady state. Since h is a constant in the Stage III, Equation (4) can be solved as:

$$C(t) = C_{ss} + (C_0 - C_{ss})exp(-\frac{k_{off}}{h}t) \quad (5)$$

where constant C_0 is the concentration of water found by extrapolating the curve to $t = 0$.

We relate the resonance position of the optical sensor to the concentration of water via Equation (1) [above 1671nm] and (4). The time-dependent concentration of water (dotted curves in Figure 4-5 (e)) is fit to Equation (5) (solid curves in Figure 4-5 (e)), by the following method: C_{ss} is a known parameter and can be calculated by averaging the $C(t \geq 20\ min)$, which are 77.1 ± 1.7, 69.9 ± 0.4, 54.2 ± 1.2 and 36.4 ± 1.0 (all in arb. unit) for 80%, 74%, 47% and 30% RH, respectively. k_{off} and C_0 are fit parameters. For 80%, 74%, 47% and 30% RH, the fitting results of k_{off} is: $0.42\ \mu m \cdot s^{-1}$, $0.27\ \mu m \cdot s^{-1}$, $0.36\ \mu m \cdot s^{-1}$ and $0.32\ \mu m \cdot s^{-1}$; C_0 is: 2281.8, 816.5, 196.6 and 266.0 (all in arb. unit); the fitting error $adj.R^2$ are: 0.88, 0.80, 0.95 and 0.84.

The standard error of k_{off} is $k_{off} = (0.34 \pm 0.06)\ \mu m \cdot s^{-1}$ for RH between 30% and 80%. The small variation in k_{off} supports the robustness of the model.

The response time characterizes the sensor's reaction to a sudden increase in RH, and is usually different from the recovery time [40–42]. The sensor response to a sudden increase of RH from 47% to 82% reveals a time of 17.1 min (Figure 4-7), longer than the recovery time. C_{ss} is calculated by averaging $C(t)$ after 30 min (since the response time is longer than the recovery time), which is 83.2 ± 0.4 (arb. unit). The fitting result is shown as the solid curve in Figure 4-7 (b), with $k_{off} = 0.40\ \mu m \cdot s^{-1}$, $C_0 = 53.9$ (arb. unit) and $adj.R^2 = 0.82$. The $k_{off} = 0.40\ \mu m \cdot s^{-1}$ matches those obtained from characterization of the recovery processes, suggesting that both moisture adsorption and desorption processes obey the same kinetics.

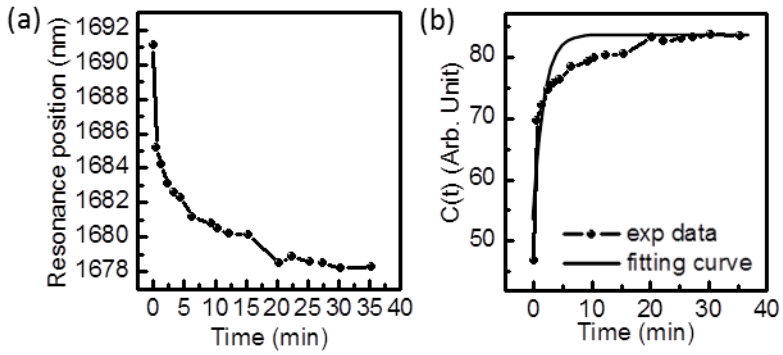

Figure 4-7 (a) Time-dependence of the hydrogel-covered Au NR array moisture sensor resonance as the environment RH is suddenly increased from 47% RH to 82% RH at time t=0. The sudden change in RH is realized by quickly transferring the sensor from 47% RH environment into the 82% RH glass chamber in Figure (3-3). (b) The $C(t)$ curve that is converted from the resonance positions in (a) via Equation (1) and Equation (4) [dotted curve] and fitting of the experimental data using Equation (5) [solid line].

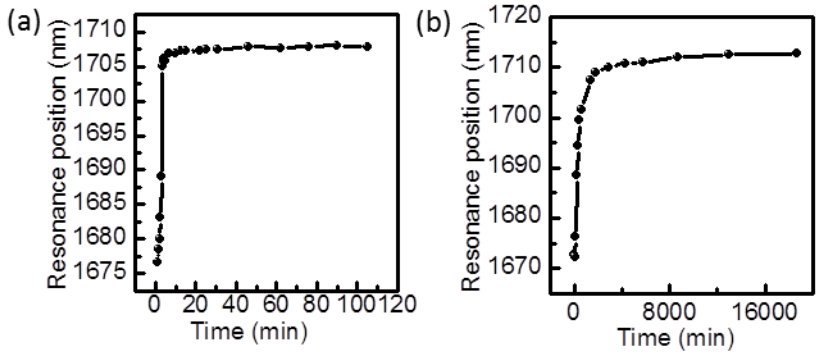

Figure 4-8 (a) Resonance variation for the 2.44 ± 0.02 μm thick hydrogel-covered Au NR array moisture sensor as it dries in a 30% RH, T = 23 ^{o}C environment after soaking in water (pH = 6). (b) Resonance variation for the 600 μm thick hydrogel-covered Au NR array moisture sensor as it dries in a 30% RH, T = 23 ^{o}C environment after soaking in water (pH = 6).

We also constructed optical sensors with varying hydrogel film thickness from 0.64 μm to 600 μm. The sensors show a similar steady-state resonance amplitude of 44.8% ± 12.1% and shift of 38 ± 6 nm. However, the recovery time for a fully soaked sensor to reach steady state in 30% RH air increases from 1.9 min to 1,624 min as the hydrogel thickness increases (Figure 4-5 (d) bottom panel and Figure 4-8). Thicker hydrogel film significantly increases the migration distance of water molecules and the amount of water that can be contained inside the hydrogel, which contributes to a longer recovery time [43].

The repeatability of the optical moisture sensor response is tested by cyclically soaking the sensor in water (pH=6) and allowing it to reach steady state in air of 30% RH three times on three different calendar days. In each cycle, the dynamic resonance shift during which the sensors are stabilized in air is recorded (Figure 4-5 (f)). The three measurements have similar fully soaked and steady state resonance positions, supporting the reproducibility of the sensor. There is a 1.4 nm variation in the measured fully soaked wavelength, which is due to different amounts of water in the hydrogel when the measurements started.

4-3 Operation wavelength tunability of the sensor and the corresponding resonance variation and change of bandwidth

We tune the operational wavelength and the resonance variation of the sensor by fabricating Au nanostructures with three different dimensions [44]: 193 ± 4 nm diameter nanodots, 362 ± 4 nm length / 238 ± 3 nm width NRs, and 640 ± 4 nm length / 217 ± 5 nm width NRs (Figure 4-9 (a-c)). The sensor's steady state resonance position λ_{ss} (in 30% RH air) increases from 885 nm to 2460 nm as the Au NR length increases. The resonance variation is characterized by $\Delta\lambda'$, which is defined as the sensor's resonance shift between being fully soaked and at steady state in 30% RH air. In this set of experiments we characterize the resonance wavelength of fully soaked sensors instead of at steady state in 100% RH air to capture the sensor's response to water/moisture appropriate to its application in agriculture. $\Delta\lambda'$ increases from 17 nm to 93 nm, and the

sensitivity $\Delta\nu'/\nu_{ss}$ increases from 0.019 to 0.039 ($\Delta\nu'$ is the frequency variation corresponding to $\Delta\lambda'$), as the Au NR length increases (Figure 4-9 (d, e) and Figure 4-10). Although the resonance variation and sensitivity increase substantially for longer NR lengths, the FWHM of the resonance also becomes larger. To better compare the response of sensors with different Au NR lengths, we define a FOM as the resonance variation $\Delta\nu'$ divided by the FWHM of the resonance peak at steady state in the frequency domain, which is equal to the product of the sensor sensitivity and quality factor Q. The FOM varies between 0.09 and 0.36 for the different sensor designs and reaches a maximum for that with the 362 ± 4 nm NR length (Figure 4-9 (e) blue dots).

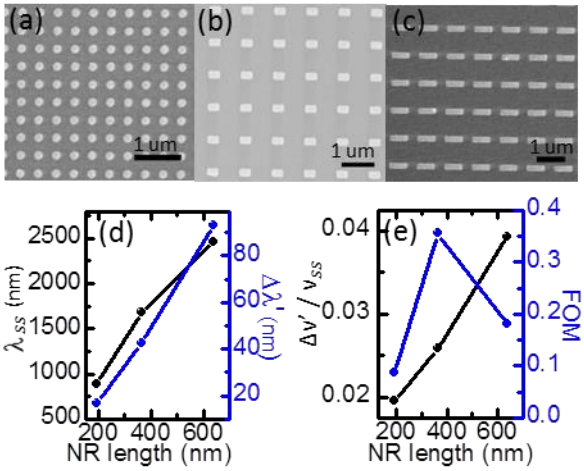

Figure 4-9 Wavelength-dependent tuning and performance of hydrogel-covered Au NR optical moisture sensors. (a-c) SEM images of Au NR arrays with diameter 193 ± 4 nm (a), length 362 ± 4 nm / width 238 ± 3 nm (b) and length 640 ± 4 nm / width 217 ± 5 nm

(c). (d) Sensor steady state resonance wavelength (λ_{ss}) and resonance variation ($\Delta\lambda'$) over the recovery process as a function of NR length. (e) Sensor frequency variation $\Delta\nu'$ relative to steady state frequency ν_{ss} and FOM as a function of NR length.

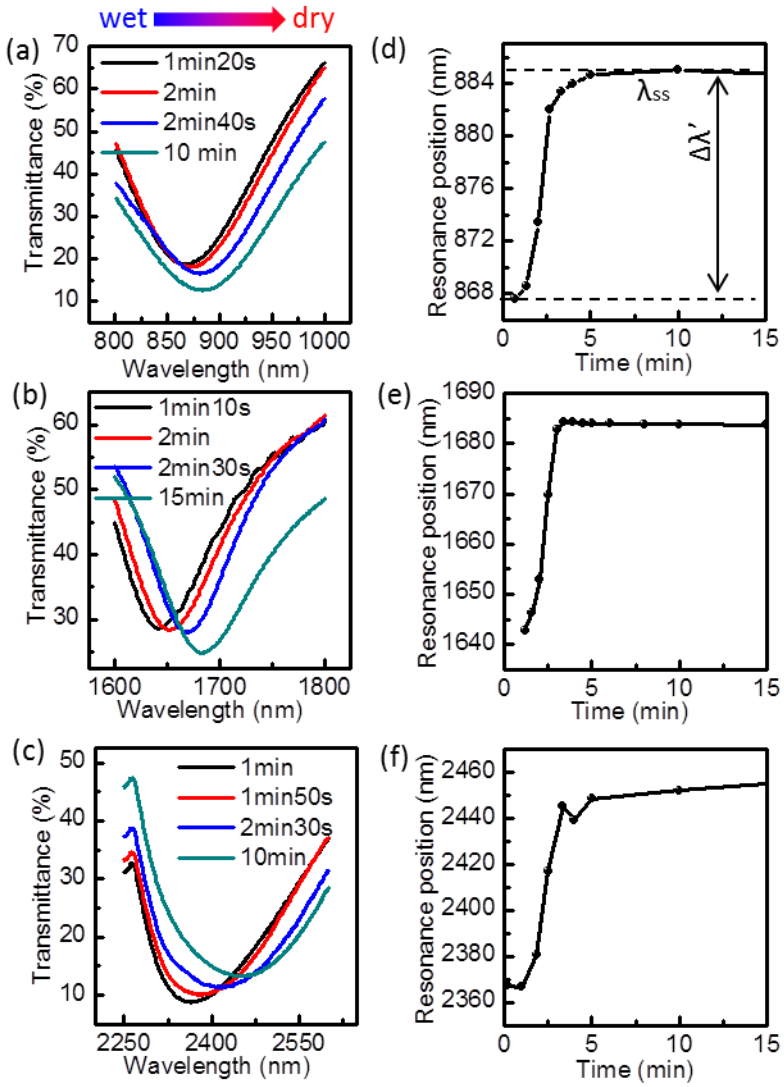

Figure 4-10 Transmittance spectra for hydrogel-covered Au NR array moisture sensors fabricated with (a) 193 ± 4 nm nanodot diameter, (b) 362 ± 4 nm NR length and (c) 640 ±

4 nm NR length, as a function of time after being fully soaked in water (pH = 6) and allowed to dry at 30% RH, T=23 ^{o}C. Resonance positions as a function of time extracted from (a-c) and plotted in (d-f), respectively. $\Delta\lambda'$ is the resonance variation range from the beginning of the recovery process to steady state. λ_{ss} is the steady state resonance position.

4-4 Test of sensor performance on real soil samples of different moisture weight percentage

A hydrogel-covered Au NR array sensor is chosen to demonstrate its suitability for remote monitoring of soil wetness. Considering the 1600 nm long-wavelength limit of our reflectance spectrometer, we select Au nanodots that are 193 ± 4 nm in diameter. Soil samples containing 56%, 27% and 10% weight percentage of water are tested (Figure 4-11 (a-c)), with the sensor turned upside down on the soil surface to facilitate moisture detection. Considering the sensor response and recovery times, the sensor is kept in contact with each soil sample for 1 h to ensure steady state is reached. Then reflectance spectra for the sensor on top of the soil surface are collected (Figure 4-11 (d) and Figure 4-12). The resonance position (black dots in Figure 4-11 (e)) of the sensor shifts from 868 ± 2 nm to 887 ± 2 nm as the weight percent of water in soil decreases from 56% to 10%. The reflectance spectra and the resonance shift are in good agreement with transmittance measurements (Figure 4-9 (d) and Figure 4-10 (a, d)). The reflectance peak amplitude is 27.6% ± 2.1% (red dots in Figure 4-11 (e), full reflectance spectra shown in Figure 4-13),

much stronger than that of a single layer photonic crystal structure [21]. The FWHM of the resonance for the sensor in 10% soil moisture is 65 THz, yielding a FOM of 0.11, which is consistent with its FOM of 0.09 in transmittance. In practice, the soil surface is rough and may cause sensors to be tilted approximately 7 to 15 degrees away from normal [17]. We tilted the sensor at different angles relative to the horizontal plane to test for any variation in the reflectance spectrum (Figure 4-11 (f)). As the tilt angle increases from 0 to 13 degrees, the resonance position remains unchanged at 889 ± 1 nm and its amplitude varies between 29.7% ± 2.3%, an 8% maximum variation.

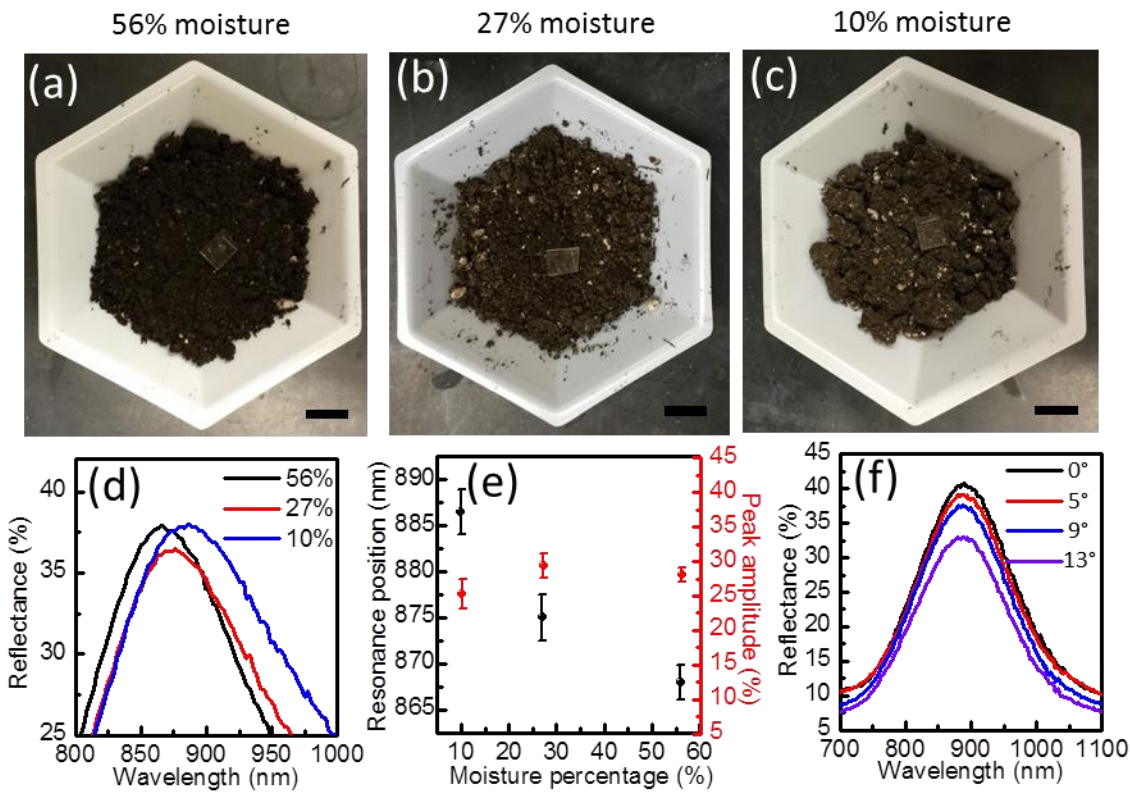

Figure 4-11 Sensor operation on surface of soil. Photographs of a hydrogel-covered Au NR optical moisture sensor placed in contact with soil samples with 56 wt% (a), 27 wt% (b) and 10 wt% (c) moisture, respectively. Scale bar = 1 cm. (d) Average reflectance spectra from three measurements of the sensor on top of each soil sample. (e) Position (black dots) and reflectivity (red dots) of the LSPR from the averaged spectra. (f) Reflectance spectra for a sensor as it is tilted at 0° (black), 5° (red), 9° (blue), and 13° (purple) to the horizontal plane.

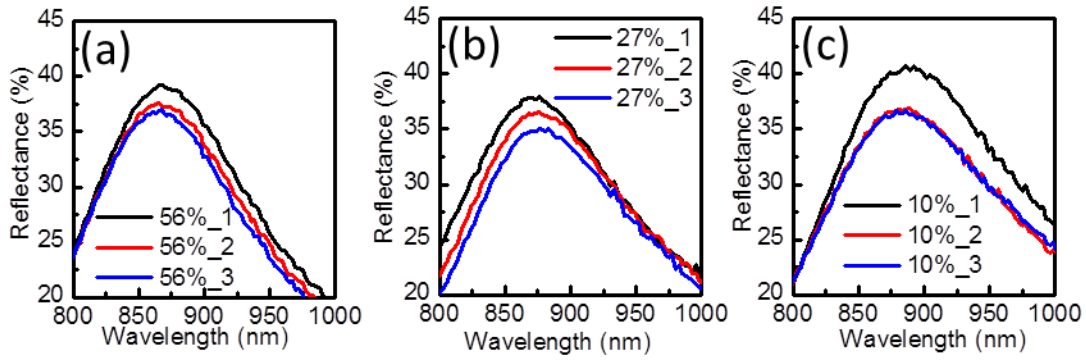

Figure 4-12 Sensor reflectance measurements on soil samples. Three measurements of the reflectance spectra for sensors on top of soil samples with 56% (a), 27% (b) and 10% (c) weight percentage of moisture. The average of the three spectra for each soil sample is presented in Figure 4-11 (d).

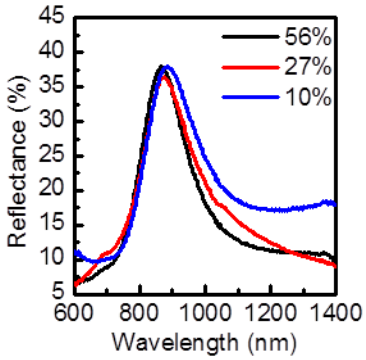

Figure 4-13 Reflectance spectra in Figure 4-11 (d) plotted over a larger spectral range.

4-5 Free standing hydrogel-colloidal Au NC nanorod array moisture sensors

In agriculture and gardening, hydrogel particles are commonly mixed with soil to help retain water. Therefore, it is of practical meaning to integrate Au nanorods into hydrogel films and thus to make the hydrogel multifunctional to both retain soil water and to monitor soil moisture levels. Here, we report the fabrication of free standing hydrogel-colloidal Au NC nanorod array moisture sensors via a method similar to template stripping nanofabrication technique,[45] as shown in Figure 4-14. Nanoimprint lithography and the solution-based deposition of colloidal Au nanocrystals are chosen to fabricate the plasmonic Au nanorod array, instead of electron-beam lithography and thermal evaporation of Au, to realize quick, large-area, low-cost fabrication. The colloidal Au NC-based nanorod array is first fabricated on a glass substrate. It is then transferred to the surface of a hydrogel film by pouring hydrogel precursor on top of the nanorod array, covering it with a glass slide which is separated by a 600 μm spacer from the colloidal Au nanorod array substrate, curing it by exposure to UV light, and finally soaking it in DI water and peeling off the hydrogel film.

The colloidal Au NC-based nanorod array on the surface of hydrogel film is characterized by SEM imaging for hydrogel films containing different weight percentages of water [Figure 4-14]. For the hydrogel with 10% w/w, the pitch of the colloidal Au nanorod array in longitudinal and transverse directions are 500 nm and 245 nm, respectively [Figure 4-15 (a)]. As the hydrogel film absorbs more water and the water weight percentage increases to 60%, the bulk of the hydrogel swells, and the pitch

of the colloidal Au NC-based nanorod array increases to 635 nm and 315 nm for the longitudinal and transverse directions [Figure 4-15 (b)].

The sensor is encapsulated by another 600 μm hydrogel layer on top of colloidal Au NC nanorod array by applying the hydrogel precursor between spacers and curing in UV light, in order to eliminate any change in contact area between the colloidal Au NC-based nanorods and the hydrogel as the sensor swells upon exposure to water. The sensor is characterized optically by transmittance measurements at different weight percentages of water [Figure 4-15 (a)]. We first soak the sensor in DI water, and take it out and measure its transmittance spectrum and weight as a function of time as the water evaporates in air. The weight of the sensor is used later to calculate the weight percentage of water in hydrogel. The resonance position of the colloidal Au nanocrystal-based nanorod array shifts from 948 nm to 982 nm as the weight percentage of water decreases from 65% to 6%. The reflectance of the sensor is also collected at 6% w/w, and the average resonance position for the three reflectance measurement is at 1071 ± 7 nm. The difference between the reflectance and transmittance resonance position at 6% w/w is 89 nm, which is probably due to the influence of the encapsulation layer on top of colloidal Au nanocrystal nanorod array. In transmittance measurements the baseline is collected from a blank hydrogel substrate, which can cancel the extinction of the encapsulation layer when doing the baseline correction, while in reflectance measurement the baseline is the lamp spectrum, so the final reflectance spectrum includes the scattering and reflectance from the encapsulation layer.

As we put the free standing hydrogel-colloidal Au nanocrystal nanorod array on top of soil samples of different moisture content, the sensor absorbs different amount of moisture according to the soil wetness [Figure 4-17]. For the wettest soil sample of 40% of moisture weight percentage, the hydrogel absorbs the most water and becomes very soft. We are still working on collecting the reflectance measurements of the sensor on top of soil samples.

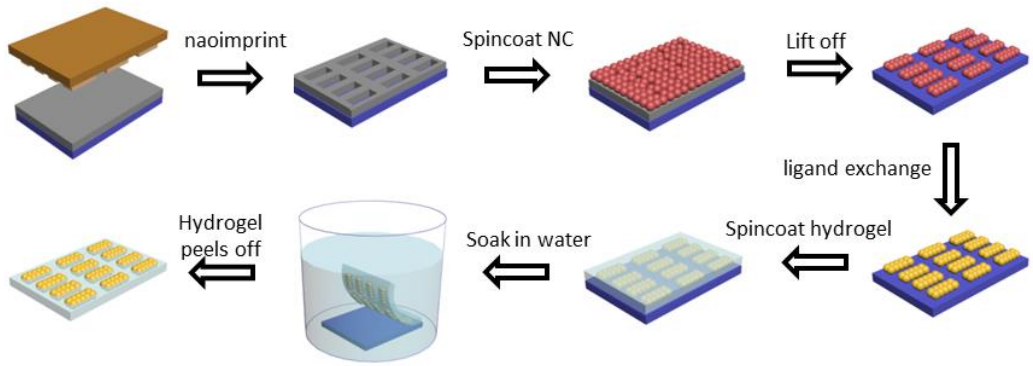

Figure 4-14 Fabrication method for free standing hydrogel-colloidal Au NC-based moisture sensor.

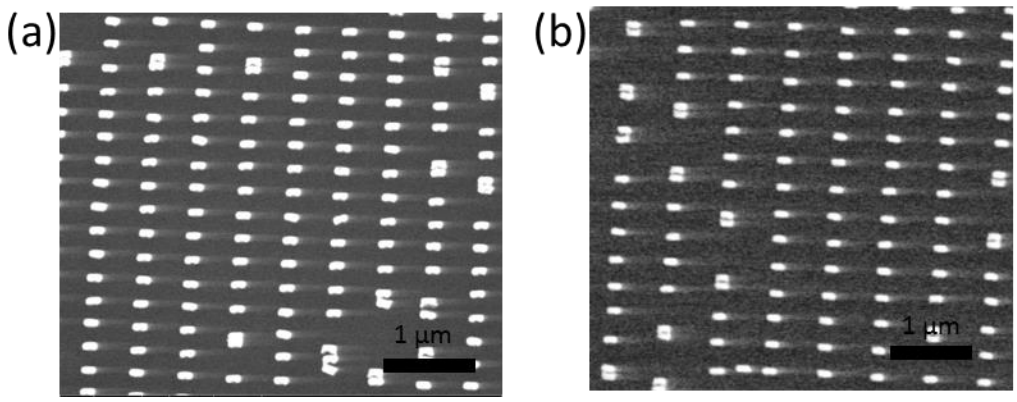

Figure 4-15 SEM images of the colloidal Au NC-based nanorod array on the surface of a hydrogel film which has different weight percentages of water: 10% (a) and 60% (b). The pitch of the colloidal Au NC-based nanorod array in the longitudinal and transverse directions are 500 nm and 245 nm for (a) and 635 nm and 315 nm for (b).

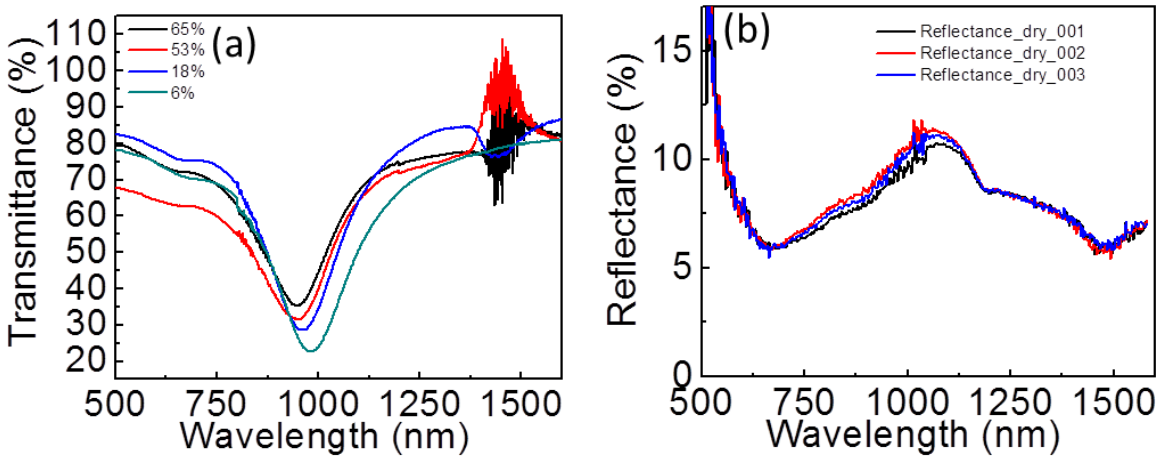

Figure 4-16 Optical characterization of the hydrogel-colloidal Au NC-based nanorod array moisture sensor. (a) Transmittance spectra of the sensor at different weight

percentages of water in hydrogel. (b) Reflectance spectrum of the sensor at room environment (RH = 30% T = 23 C°).

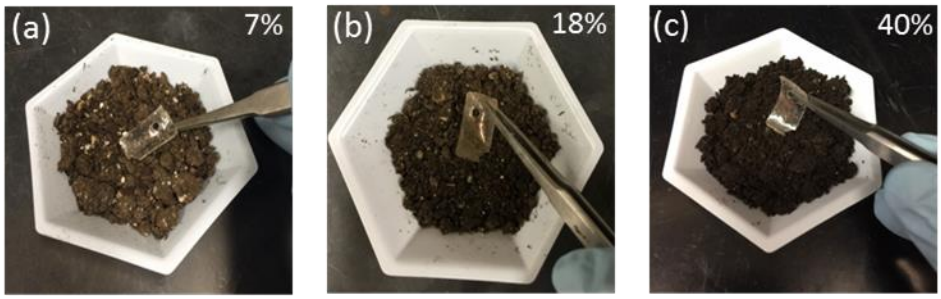

Figure 4-17 Free standing hydrogel-colloidal Au nanocrystal nanorod array moisture sensor on top of soil samples of 7% (a), 18% (b), and 40% (c) weight percentage of moisture.

4-6 Conclusions

In conclusion, we demonstrate a simple, unpowered, and environmentally-friendly optical moisture sensor for agricultural use. The sensor is based on ultrathin Au NR arrays in combination with hydrogel films to provide a high-reflectivity, spectrally-tailorable, and fast optical response to measure water content in soil. Large-area, low-cost fabrication methods such as roll-to-roll nanoimprinting and solution-based deposition of colloidal Au nanocrystals provide a route to scalable nanomanufacturing of sensors.[46–50] Combining Au NR arrays with polymers responsive to species such as soil pH, organic matter, minerals, and pathogens promises a general optical sensor platform for

environmental sensing. With agriculture drones providing high resolution IR images as frequently as every day, the optical sensor holds much potential for high spatial and temporal resolution remote monitoring of soil conditions across the large acreage of fields.

4-7 References

(1) *Coping with water scarcity An action framework for agriculture and food security*; 2012.

(2) *Water withdrawal by sector , around 2010*; 2016.

(3) Topp, G. C.; Davis, J. L.; Annan, A. P. *Water Resour. Res.* **1980**, *16*, 574–582.

(4) Robinson, D. a.; Jones, S. B.; Wraith, J. M.; Or, D.; Friedman, S. P. *Vadose Zo. J.* **2003**, *2*, 444.

(5) Blonquist Jr., J. M.; Jones, S. B.; Robinson, D. A. *J. Hydrol.* **2005**, *314*, 235–245.

(6) Qu, W.; Bogena, H. R.; Huisman, J. A.; Vereecken, H. *Vadose Zo. J.* **2013**, *12*, 1–37.

(7) Muñoz-Carpena, R.; Shukla, S.; Morgan, K. *Field devices for monitoring soil water content*; 2004; Vol. 343.

(8) Yu, X.; Wu, P.; Han, W.; Zhang, Z. *Comput. Stand. Interfaces* **2013**, *35*, 59–64.

(9) Ruiz-Garcia, L.; Lunadei, L.; Barreiro, P.; Robla, I. *Sensors* **2009**, *9*, 4728–4750.

(10) Vereecken, H.; Huisman, J. A.; Pachepsky, Y.; Montzka, C.; van der Kruk, J.; Bogena, H.; Weihermüller, L.; Herbst, M.; Martinez, G.; Vanderborght, J. *J. Hydrol.* **2014**, *516*, 76–96.

(11) Wang, N.; Zhang, N.; Wang, M. *Comput. Electron. Agric.* **2006**, *50*, 1–14.

(12) Hong, S.; Shin, I. *J. Hydrol.* **2011**, *405*, 24–30.

(13) Saleh, K.; Wigneron, J.-P.; Waldteufel, P.; de Rosnay, P.; Schwank, M.; Calvet, J.-C.; Kerr, Y. H. *Remote Sens. Environ.* **2007**, *109*, 42–53.

(14) Ulaby, F. T.; Dubois, P. C.; van Zyl, J. *J. Hydrol.* **1996**, *184*, 57–84.

(15) Altese, E.; Bolognani, O.; Mancini, M.; Troch, P. A. *Water Resour. Res.* **1996**, *32*, 653–661.

(16) Reigber, A.; Scheiber, R.; Jager, M.; Prats-Iraola, P.; Hajnsek, I.; Jagdhuber, T.; Papathanassiou, K. P.; Nannini, M.; Aguilera, E.; Baumgartner, S.; Horn, R.; Nottensteiner, A.; Moreira, A. *Proc. IEEE* **2013**, *101*, 759–783.

(17) Baghdadi, N.; Aubert, M.; Cerdan, O.; Franchistéguy, L.; Viel, C.; Eric, M.; Zribi, M.; Desprats, J. F. *Sensors* **2007**, *7*, 2458–2483.

(18) Colomina, I.; Molina, P. *ISPRS J. Photogramm. Remote Sens.* **2014**, *92*, 79–97.

(19) Barry, R. A.; Wiltzius, P. *Langmuir* **2006**, *22*, 1369–1374.

(20) Yin, S.-N.; Wang, C.-F.; Liu, S.-S.; Chen, S. *J. Mater. Chem. C* **2013**, *1*, 4685.

(21) Tian, E.; Wang, J.; Zheng, Y.; Song, Y.; Jiang, L.; Zhu, D. *J. Mater. Chem.* **2008**,

18, 1116.

(22) Islam, M. R.; Xie, S.; Huang, D.; Smyth, K.; Serpe, M. J. *Anal. Chim. Acta* **2015**, *898*, 101–108.

(23) Shi, J.; Hsiao, V. K. S.; Walker, T. R.; Huang, T. J. *Sensors Actuators B Chem.* **2008**, *129*, 391–396.

(24) Wang, L.; Liu, Y.; Zhang, M.; Tu, D.; Mao, X.; Liao, Y. *Meas. Sci. Technol.* **2007**, *18*, 3131–3134.

(25) Xuan, R.; Wu, Q.; Yin, Y.; Ge, J. *J. Mater. Chem.* **2011**, *21*, 3672.

(26) Hu, H.; Chen, Q.-W.; Cheng, K.; Tang, J. *J. Mater. Chem.* **2012**, *22*, 1021–1027.

(27) Luechinger, N. a; Loher, S.; Athanassiou, E. K.; Grass, R. N.; Stark, W. J. *Langmuir* **2007**, *23*, 3473–3477.

(28) Qi, Z.; Honma, I.; Zhou, H. *Opt. Lett.* **2006**, *31*, 1854.

(29) Wang, P.; Zhang, L.; Xia, Y.; Tong, L.; Xu, X.; Ying, Y. *Nano Lett.* **2012**, *12*, 3145–3150.

(30) Kunstmann-Olsen, C.; Belić, D.; Bradley, D. F.; Grzelczak, M. P.; Brust, M. *Chem. Mater.* **2016**, *28*, 2970–2980.

(31) Payne, E. K.; Shuford, K. L.; Park, S.; Schatz, G. C.; Mirkin, C. A. *J. Phys. Chem. B* **2006**, *110*, 2150–2154.

(32) Sönnichsen, C.; Alivisatos, P. A. *Nano Lett.* **2005**, *5*, 301–304.

(33) DeSantis, C. J.; Huang, D.; Zhang, H.; Hogan, N. J.; Zhao, H.; Zhang, Y.; Manjavacas, A.; Zhang, Y.; Chang, W.-S.; Nordlander, P.; Link, S.; Halas, N. J. *J. Phys. Chem. C* **2016**, *120*, 20518–20524.

(34) Abadeer, N. S.; Fülöp, G.; Chen, S.; Käll, M.; Murphy, C. J. *ACS Appl. Mater. Interfaces* **2015**, *7*, 24915–24925.

(35) Mesch, M.; Zhang, C.; Braun, P. V.; Giessen, H. *ACS Photonics* **2015**, *2*, 475–480.

(36) Ye, J.; Van Dorpe, P. *Plasmonics* **2011**, *6*, 665–671.

(37) Sinha, R. K. *Modern Plant Physiology*; Alpha Science International Ltd., 2004.

(38) Mahajan, P. V.; Oliveira, F. A. R.; Macedo, I. *J. Food Eng.* **2008**, *84*, 281–288.

(39) Ghi, P. Y.; Hill, D. J. T.; Whittaker, A. K. *Biomacromolecules* **2002**, *3*, 554–559.

(40) Bi, H.; Yin, K.; Xie, X.; Ji, J.; Wan, S.; Sun, L.; Terrones, M.; Dresselhaus, M. S. *Sci. Rep.* **2013**, *3*, 2714.

(41) Zambov, L. M.; Popov, C.; Abedinov, N.; Plass, M. F.; Kulisch, W.; Gotszalk, T.; Grabiec, P.; Rangelow, I. W.; Kassing, R. *Adv. Mater.* **2000**, *12*, 656–660.

(42) Bedoya, M.; Díez, M. T.; Moreno-Bondi, M. C.; Orellana, G. *Sensors Actuators B Chem.* **2006**, *113*, 573–581.

(43) Li, Y.; Tanaka, T. *J. Chem. Phys.* **1990**, *92*, 1365–1371.

(44) Lee, K.; El-Sayed, M. A. *J. Phys. Chem. B* **2006**, *110*, 19220–19225.

(45) Zhou, W.; Odom, T. W. *Nat. Nanotechnol.* **2011**, *6*, 423–427.

(46) Chen, W.; Tymchenko, M.; Gopalan, P.; Ye, X.; Wu, Y.; Zhang, M.; Murray, C. B.; Alu, A.; Kagan, C. R. *Nano Lett.* **2015**, *15*, 5254–5260.

(47) Fafarman, A. T.; Hong, S.-H.; Caglayan, H.; Ye, X.; Diroll, B. T.; Paik, T.; Engheta, N.; Murray, C. B.; Kagan, C. R. *Nano Lett.* **2013**, *13*, 350–357.

(48) Zhang, M.; Bechstein, D. J. B.; Wilson, R. J.; Wang, S. X. *Nano Lett.* **2014**, *14*, 333–338.

(49) Ahn, S. H.; Guo, L. J. *Adv. Mater.* **2008**, *20*, 2044–2049.

(50) Henzie, J.; Lee, M. H.; Odom, T. W. *Nat. Nanotechnol.* **2007**, *2*, 549–554.

Chapter 5 Mechanically-tunable hybridized Au grating resonances on elastomeric substrates

Significant components of this chapter will be submitted as "Mechanically-Tunable Hybridized Au Grating Resonances on Elastomeric Substrates" by Wenxiang Chen, Wenjing Liu, Yijie Jiang, Naixin Song, Mingliang Zhang, Nicholas J. Greybush, Jiacen Guo, Kevin T. Turner, Ritesh Agarwal, Cherie R. Kagan.

Metamaterials are artificially designed materials with unique optical properties,[1–3] which have important applications in sensors,[4–6] photodetectors and photovoltaics,[7–9] metalenses,[10–12] waveplates,[13–16] and holography.[17] Most metamaterials operate at a single wavelength or within a limited bandwidth because of the fixed size of the nanoscale components and the unchangeable optical properties of the plasmonic materials. Actively tunable metamaterials, which can be achieved by integrating dynamically tunable components, such as semiconductors, phase-changing materials and elastomers in metamaterials, have been extensively explored in recent years.[18–22] Among different dynamically tunable components, the elastomeric substrate provides an excellent way to tune the operation wavelength of the metamaterials over a wide wavelength range by changing the distance between coupled plasmonic structures.[20,23] Experiments have reported nanoparticle dimers and closely placed double split ring resonators on elastomeric substrates, where the coupling distance tunes the coupled surface plasmon

resonance wavelength by applying strain on the substrates. However, the coupled surface plasmonic resonances tend to have broad linewidth and low intensity because of the fast radiative decay of the plasmons. Plasmonic resonances with narrow line-width and high-amplitude are needed for actively tunable devices.

Nanostructure lattice arrays are excellent candidates for ultra-narrow and high-amplitude resonances because the radiated energy from each single nanostructure can be collected by the nearby nanostructures, resulting in a prolonged plasmon lifetime.[24–27] Strong coupling effects and Fano resonances with sharp optical features have been demonstrated in surface lattice resonances, mostly at fixed pitch sizes.[24,28]

Here we report a high-amplitude, small line-width surface lattice resonance which can be linearly tuned by the strain on the PDMS substrate. In contrast to previous work in which the diffraction orders are strongly coupled with the surface plasmonic resonances and deviate from the linear relationship with the grating pitch, we design Au gratings for a weakly coupled surface lattice resonance which follows a linear variation with the grating pitch. The weak coupling gives the Au grating diffraction peaks a uniformly high amplitude and narrow line-width during the pitch tuning. For the fabrication of these nanostructures, we develop a process to pattern the nanostructures using electron-beam lithography (EBL) directly on the PDMS substrate. The process allows the fabrication of lattice structures for a variety of materials, and it is much simpler than methods which commonly use pattern transfer. To greatly enhance the mechanical tunability of the Au lattice grating pitch, we also design a structure using two nanobars sandwiching the Au grating to focus the strain.

5-1 Fabrication of Au gratings on PDMS substrate

Well-established methods for fabrication of nanostructures on elastomeric substrates include pattern transfer,[19,29] nanostencil lithography,[30] and Si wafer etching.[20] These methods all involve multiple steps to transfer the pattern or in fabricating masks. Here, we demonstrate an alternative fabrication method which uses electron beam lithography directly on the PDMS substrates [Figure 5-1]. A charge-release layer made of 12 nm Au is deposited by thermal evaporation on the resist (PMMA 495 A4 and PMMA 950 A2) on the PDMS substrate before patterning by electron beam lithography. After exposure to the electron beam (50 pA), the Au layer is removed by wet etching, and the resist is developed in an MIBK solution (MIBK : IPA = 1 : 3) for 90 s. Different kinds of materials are deposited onto the developed substrate by e-beam evaporation. The patterns are defined by a subsequent lift-off process in acetone at 60 °C for 6 hours to dissolve remaining resist. Using this method, we successfully fabricated nanoscale structures in the shapes of squares, gratings and nanorods from a variety of materials, such as Au, Ge and SiO_2 [Figure 5-2 (a-e)]. Nanostructures based on colloidal Au nanocrystals can also be fabricated by replacing the e-beam evaporation step with spin-coating of colloidal Au nanocrystals. However, it must be noted: the yield of the nanocrystal structures on PDMS substrate is below 30% due to the weak adhesion between colloidal Au nanocrystals and the PDMS substrate. Further surface treatment or ligand modification to the nanocrystals is needed to improve the adhesion.

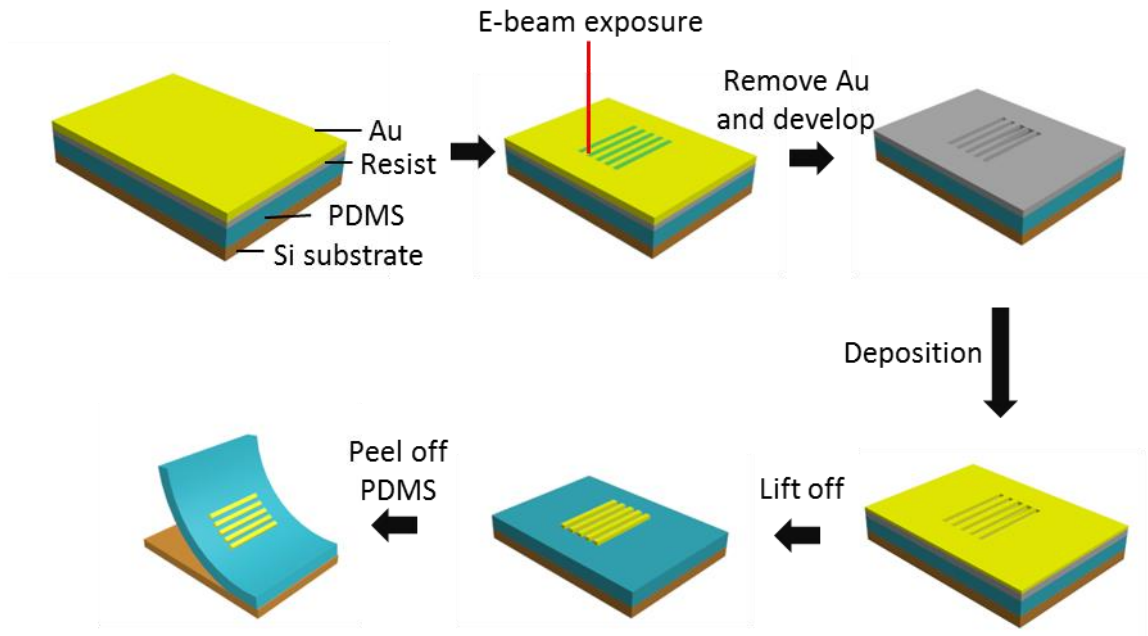

Figure 5-1 Fabrication method for nanostructures on a PDMS substrate. The PDMS substrate is supported by a Si substrate to reduce its deformation during the fabrication process. A 12 nm Au film is deposited on the resist on the PDMS substrate as a charge releasing layer for the subsequent electron beam lithography. Electron beam lithography is used to create different kinds of nanoscale patterns, and then the Au layer is removed by wet etching and the resist is developed. Different types of materials are deposited onto the patterned sample by e-beam evaporation. With a lift-off process, nanostructures are created on the PDMS substrate and the PDMS substrate is ready to be peeled off from the Si wafer.

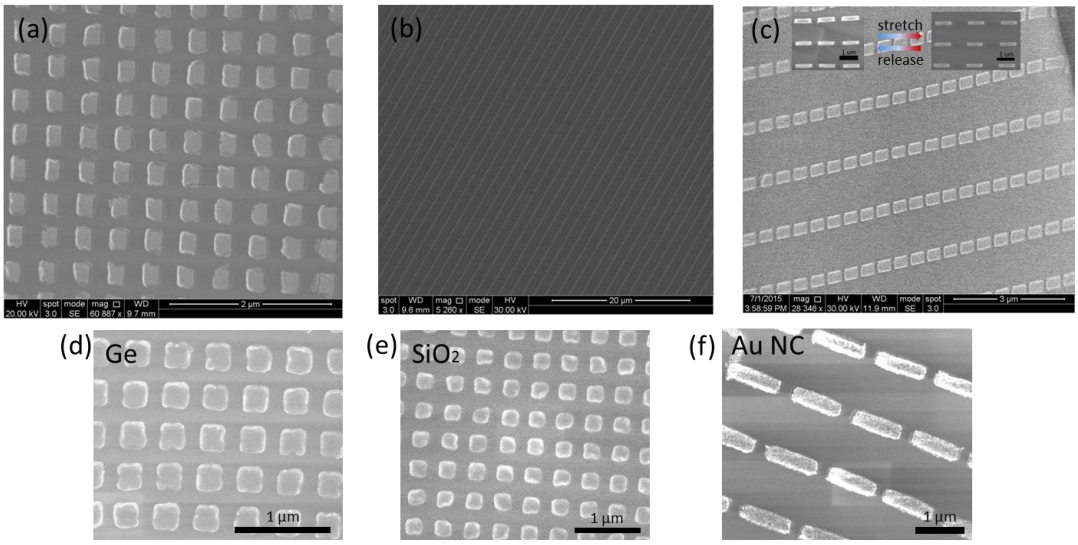

Figure 5-2 Nanoscale structures fabricated by direct electron beam lithography patterning. (a) Au squares of 250 nm length. (b) Au gratings. (c) Au nanorod array. The inset shows that stretching along the longitudinal direction of the nanorod increases the pitch of the Au nanorod array in the same direction. (d) Ge and (e) SiO_2 squares of 250 nm length. (f) Colloidal Au nanocrystal-based nanorod arrays fabricated on PDMS substrates by spin coating of Au nanocrystal dispersions.

5-2 Enhancing the mechanical tunability of Au grating pitch

We introduce a mechanical design of a "sandwich" structure to enhance the tunability of the grating pitch. Two nanobars are placed on opposite sides of the Au grating, as shown in the schematics in Figure 5-3. The dimensions of a single nanoline in the grating structure are 12 μm in length, 230 nm in width, and 20 nm in thickness, and the pitch of the grating is designed to be 490 nm [Figure 5-4 (a-d)]. The nanobar is 12 μm

by 80 μm in size and 20 nm in thickness. “D” is defined as the distance between the edge of the grating to the closest side of the nanobar. It is an important parameter that determines how large the strain is amplified in the gap region between two nanobars.

We explore how much the strain is amplified in the gap region between the two nanobars for different distance “D” [Figure 5-4]. 30% strain is applied on the PDMS substrate along the direction vertical to the nanolines in the grating. For the Au grating without nanobars (D = ∞), the pitch of the Au grating does not increase [Figure 5-4 (a,e)]. On the contrary, it decreases by 8%. We hypothesize that since the Au grating structure is quite small (12 μm in length), the vertical strain goes around the grating and the resulted tangential strain decreases the grating pitch. As the nanobar is placed at D = 50 μm, 30 μm, and 20 μm from the Au grating [Figure 5-4 (b-d)], the increase of the pitch at 30% strain are 21%, 28% and 32%, respectively [Figure 5-4 (f-h)]. As the nanobar is positioned closer to the Au grating, the enhancement of the grating pitch tunability is more prominent. Large-area SEM images containing both the nanobar structures and the Au grating before and after applying strain are shown in Figure 5-5 and are used to understand the movement of the nanobar structures during stretching.

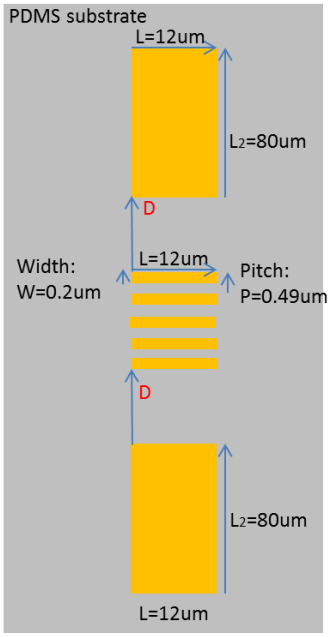

Figure 5-3 Design and dimensions of the Au grating and nanobar structures.

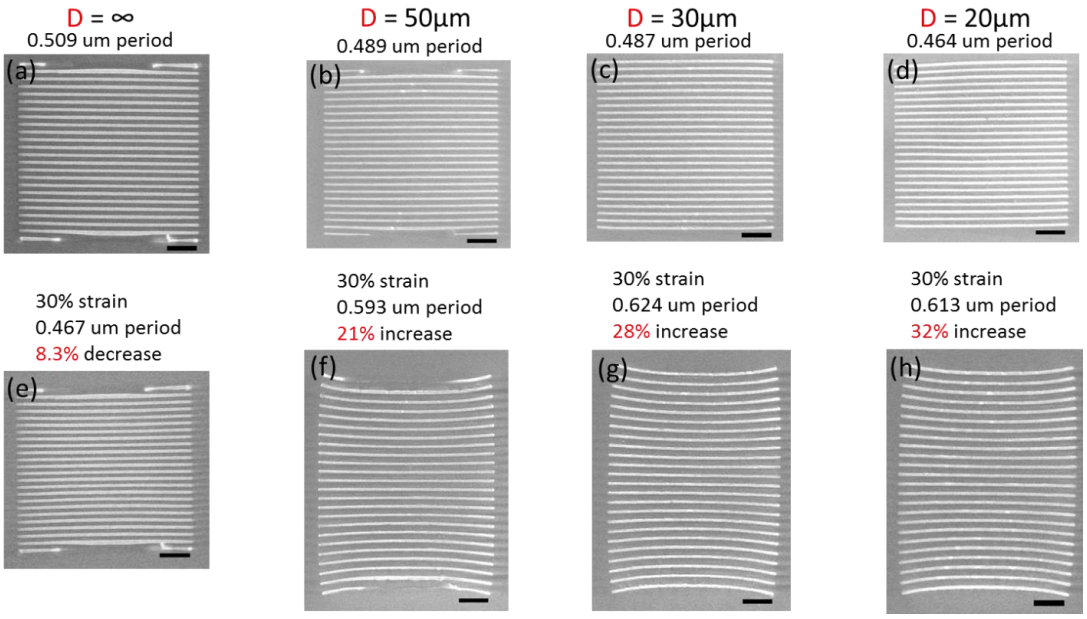

Figure 5-4 Au gratings with nanobars at different distance D: (a, e) D = ∞, which means there is no nanobar; (b,f) D = 50 μm; (c,g) D = 30 μm; and (d,h) D = 20 μm. (a-d) There is no strain applied to the PDMS substrate. (e-h) There are 30% (or 40% for D = ∞) applied on the PDMS substrate.

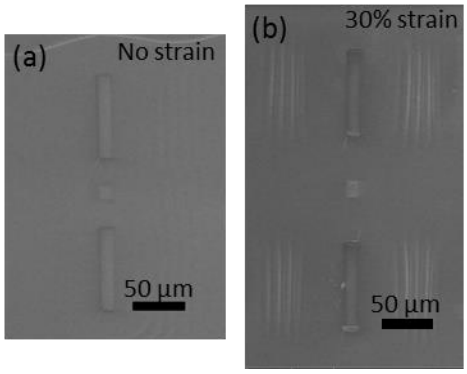

Figure 5-5 SEM images of Au grating sandwiched by two nanobars. The square region in the center of the image contains the grating, and the nanobars are at the top and bottom sides of the grating. (a) Without strain on the PDMS substrate. (b) 30% strain is applied on the PDMS substrate. D is defined as the distance between the edge of the grating to the closest side the nanobar.

Mechanical simulation via finite element modeling is used to analyze the strain distribution for the gratings and nanobars on the PDMS substrate. The displacement of the Au grating in the "sandwich" structures of D = ∞, D = 50 μm, D = 30 μm and D = 20 μm are simulated. As 30% strain is applied on the substrate, the increases of the grating pitch are 20%, 24%, 28% and 33%, respectively [Figure 5-6 (a-d)].

The strain distribution on the PDMS substrate is presented in Figure 5-7 to illustrate why the strain is amplified as D decreases. For the grating without the nanobar [Figure 5-7 (a)] (with the grating located at the center of the figure), the strain on the PDMS substrate is uniform and small. In contrast, for D = 50 μm, D = 30 μm and D = 20

μm [Figure 5-7 (b-d)], the strain distribution has been modified around and underneath the nanobar structures. The strain has been increased to 50%, 60%, and 80% between the two nanobar structures for D = 50 μm, 30 μm, and 20 μm. This is explained as: the area underneath the nanobar is pinned by the nanobars and there is no deformation. As the PDMS substrate is stretched by 30%, the area near the top and the bottom end of the nanobar have to be stretched more to compensate for the zero deformation of the PDMS substrate underneath the nanobar structures. As a result, the strain between the nanobars is enhanced compared to the case without nanobars. As the distance between the nanobars and grating decreases, the strain enhancement becomes more prominent [Figure 5-8].

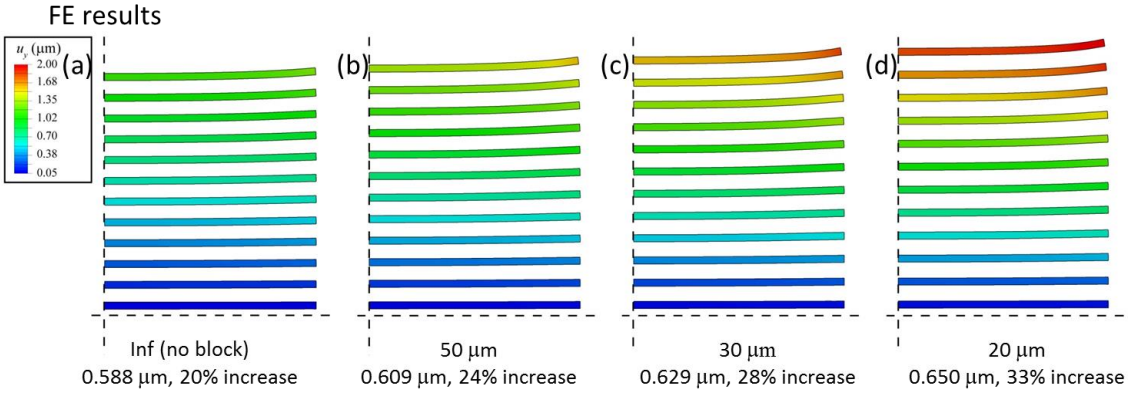

Figure 5-6 Finite element model simulation for D = ∞ (a), D = 50 μm (b), D = 30 μm (c), D = 20 μm (d) grating and nanobar sandwich structures. 30% deformation is applied on the PDMS substrate. The color intensity represents the displacement of the nanoline along the vertical direction. One-quarter of the sandwich structure is shown in the strain

distribution map since symmetric boundary conditions are used along the x and y axes for the simulation.

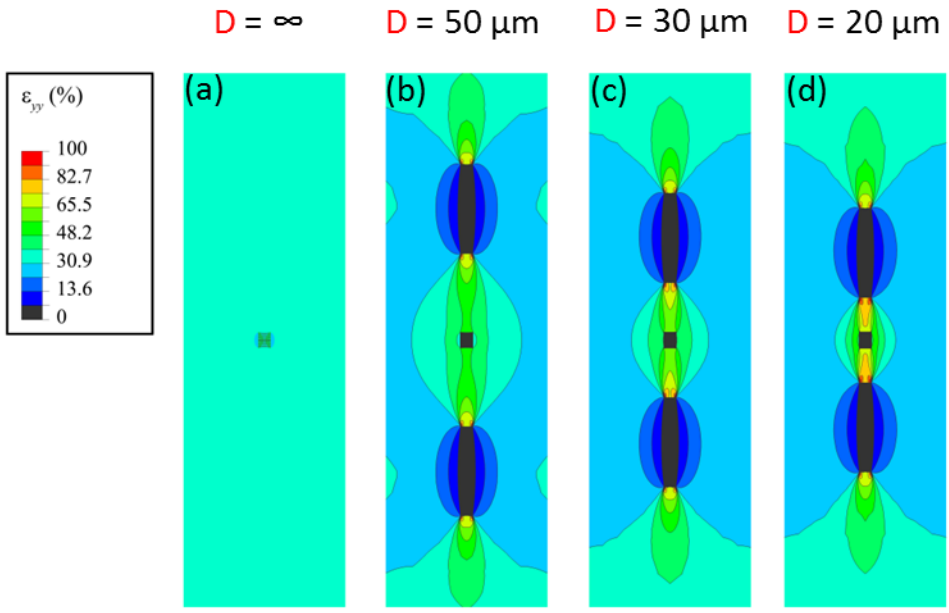

Figure 5-7 The strain distribution for D = ∞ (a), D = 50 µm (b), D = 30 µm (c), D = 20 µm (d) grating and nanobar sandwich structures.

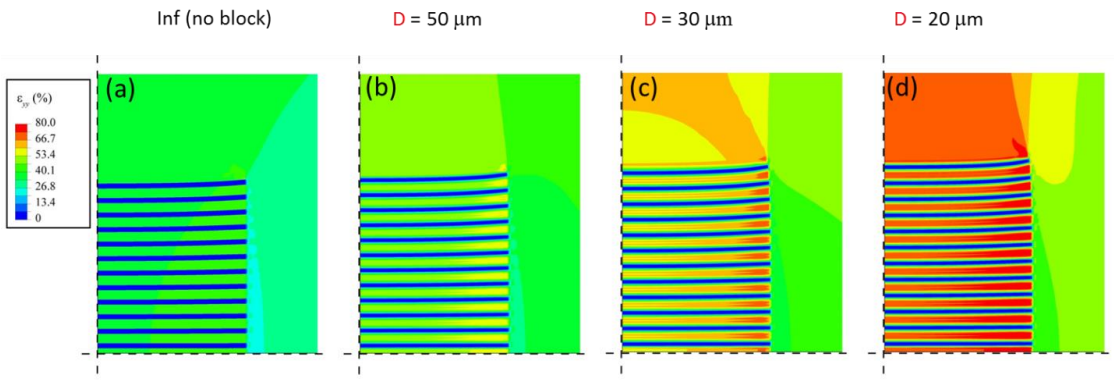

Figure 5-8 The strain distribution near the grating area for D = ∞ (a), D = 50 μm (b), D = 30 μm (c), D = 20 μm (d) grating and nanobar sandwich structures. One-quarter of the grating structure is shown as symmetric boundary conditions are used in the simulations.

5-3 Theoretical simulations and optical characterization of the Au grating under different strain

Theoretical simulations based on the finite domain time difference (FDTD) method are performed to understand the optical response of the Au gratings on the PDMS substrate (n = 1.4). We first study the optical response of a single Au nanoline which has a width of 160 nm and height of 40 nm. The incident light is a plane wave with linear polarization vertical to the nanoline, and it is incident normally on the structure [Figure 5-9]. The simulated scattering cross-section of the nanoline is presented in Figure 5-10, with an LSPR at around 700 nm. The electrical field distribution around the nanoline at 730 nm wavelength supports the existence of the LSPR, as seen by the strongly enhanced electrical field intensity at the edges of the nanoline structure [Figure 5-10].

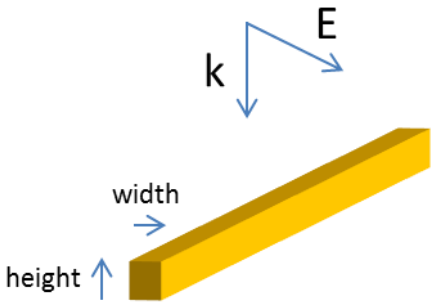

Figure 5-9 Schematic for a single nanoline structure illuminated with linearly polarized light at normal incidence. The dimensions of the nanoline are 160 nm in width and 40 nm in height. The PDMS substrate is not shown in the schematic but is considered in the simulation as a substrate with refractive index n = 1.4.

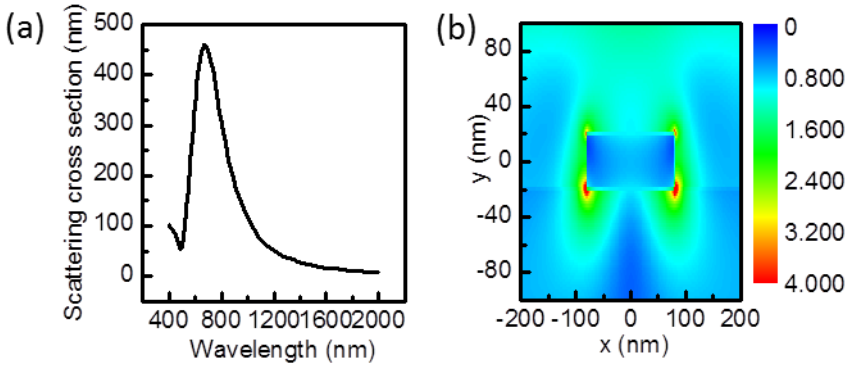

Figure 5-10 FDTD simulations for a single nanoline. The dimensions of the nanoline are 160 nm in width and 32 nm in height. Linear polarization vertical to the single nanoline structure is incident normally from the top. (a) The scattering cross-section of the nanoline is simulated. (b) The electrical field intensity distribution around the nanoline at 730 nm.

We also simulate the optical response for the grating structures [Figure 5-11]. The Au grating pitch size is varied from 400 nm to 600 nm [Figure 5-12]. The resonance peak in the reflectance spectra at a pitch of 400 nm has a large amplitude of about 75%. As the pitch increases to 600 nm, the resonance peak gradually moves to longer wavelengths and its linewidth becomes sharper and weaker. A second resonance peak appears at shorter wavelengths, due to higher-order diffraction modes. For a more comprehensive understanding of the simulated optical response of the Au grating, we plot its reflectance intensity in a contour image as functions of the grating pitch and the incident wavelength of light [Figure 5-13]. There are straight lines in the contour image extending from the bottom left corner of the image to the top right corner, which arise from different order diffraction modes of the Au grating. When the diffraction orders are within the LSPR wavelength range of a single nanoline, they couple with the LSPR and the intensity of the diffraction order peak is greatly enhanced (by about 65% in reflectance). The FWHM of the peak is also narrowed. At the pitch of 490 nm, the FWHM is as small as 50 nm. As the diffraction order moves out of the LSPR wavelength range, the diffraction orders decouple with the LSPR of the single Au nanoline; thus the peak intensity drops very quickly to below 10% and the FWHM of the peak also increases (FWHM = 160 nm at pitch size of 735 nm).

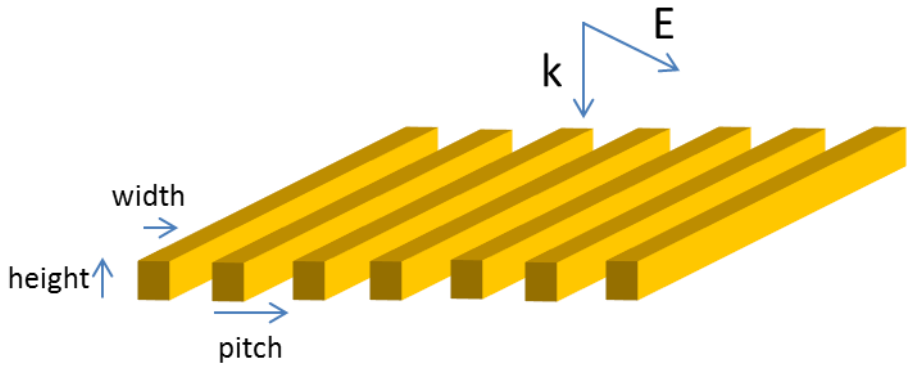

Figure 5-11 Schematic of a Au grating structure illuminated by the linearly polarized light at normal incidence. The PDMS substrate is not shown in the schematic but is considered in the simulation by assuming a substrate with refractive index n = 1.4.

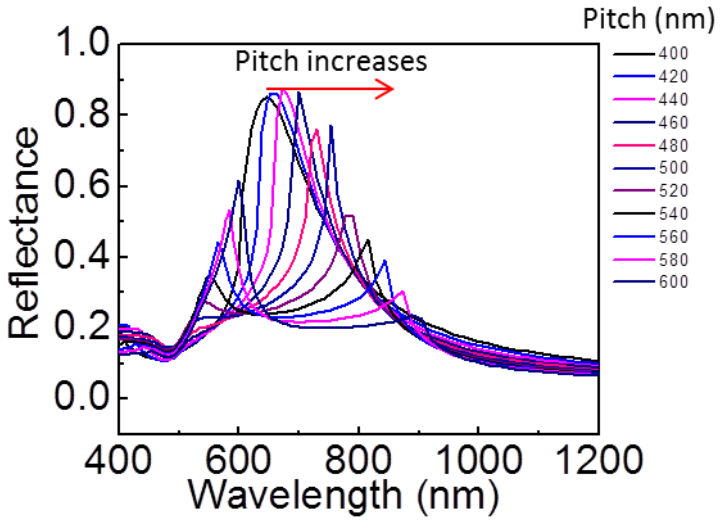

Figure 5-12 Reflectance simulation results for Au grating structures. The simulations are carried out for different grating pitch varying from 400 nm to 600 nm.

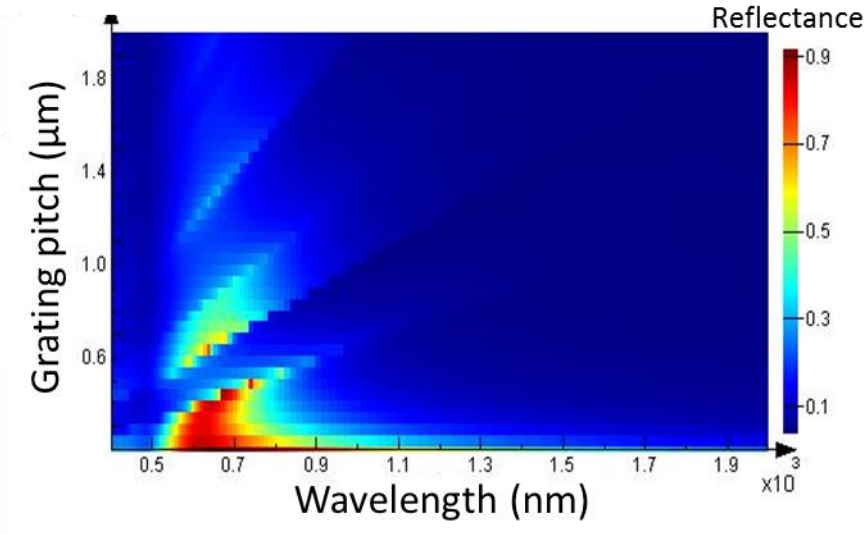

Figure 5-13 Reflectance simulation results for Au grating structures plotted in a contour image. The reflectance intensity of the Au grating is simulated as a function of grating pitch and the wavelength of incident light.

In the experiment, we use an angle-resolved reflectance measurement setup to collect the reflectance spectra of the Au gratings at different reflectance angles [Figure 5-14].[26] The reflectance from different reflectance angles are focused at different spots on the back focal plane (Fourier plane) of the objective. The spectrometer in combination with a CCD camera can collect the light intensity as a function of wavelength and can also record the spatial position of the light at the entrance slit to resolve the reflectance angle. We choose to measure the Au gratings with nanobars at D = 20 μm at different strains varying from 0% to 28% for demonstration. The results are shown in Figure 5-15. The contour images include the reflectance spectra of the Au grating at different reflectance angles from -45°

to 45° (since the numerical aperture of the objective is 0.7). The reflectance spectra at angle 0° are shown at Figure 5-16 (a). As the strain increases from 0% to 28%, the grating pitch increases, and the resonance peak position varies by 92 nm (from 750 nm to 842 nm). For a comparison, at 0% strain the FWHM of the resonance peak is 162 nm. Each resonance peak at different strain levels can be well-resolved from the spectra, due to the high resonance intensity and small FWHM. Finally, the strain is released from the PDMS substrate and the reflectance spectrum of the Au grating is measured again. The resonance peak position [purple curve in Figure 5-16 (a)] moves back to 745 nm which is at about the same resonance position as the 0% strain measurement, which proves that the stretching process is reversible. The shift of the resonance peak is approximately linear with the applied amount of strain, with a rate of 3 nm per 1% strain from the linear fit [Figure 5-17]. The simulation results for Au gratings of pitch size varying from 480 nm to 560 nm are compared with the experiment results [Figure 5-16 (b)]. At 0% strain the pitch of the Au grating is at approximately 480 nm by SEM imaging. We estimate that at 28% strain the pitch is at around 560 nm. However, further SEM images are needed for proving this. In the simulation results, the resonance peak varies from 728 nm to 843 nm, matching well with the experimental results. The peak intensity decreases due to the diffraction order moving away from LSPR of the single Au nanoline.

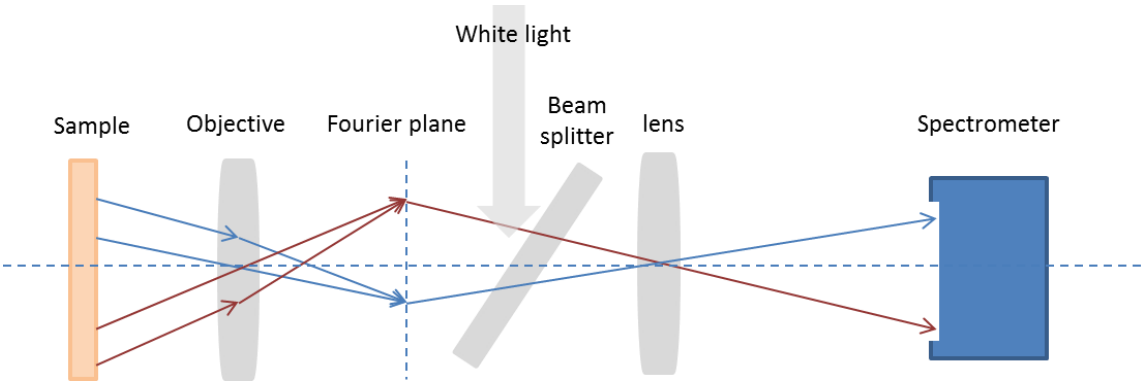

Figure 5-14 Experimental setup for angle-resolved reflectance measurements that allow the collection of samples' reflectance at different angles.

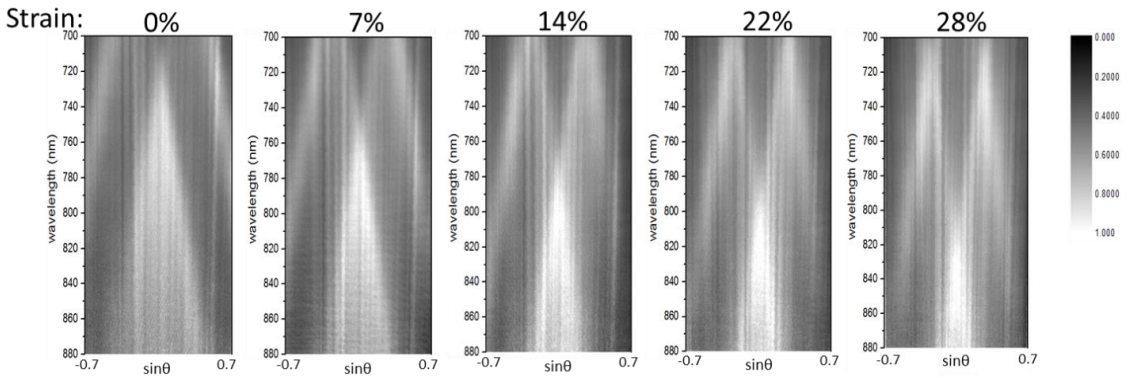

Figure 5-15 Experiment results for the angle-resolved reflectance spectra of the Au grating with nanobars at D = 20 μm on a PDMS substrate. A variety of strains, from 0% to 28%, are applied to the PDMS substrate with a direction perpendicular to the nanolines in the grating.

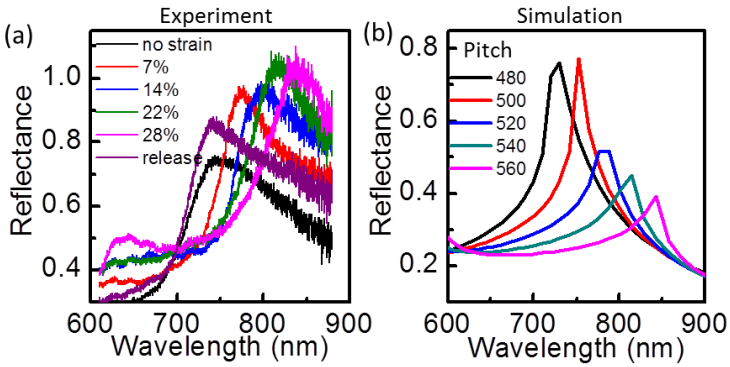

Figure 5-16 Comparison of meausred (a) and simulated (b) reflectance spectra for Au gratings at 0° incident angle at different strains and thus different grating pitches.

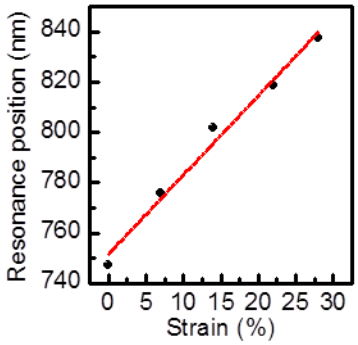

Figure 5-17 The relationship between the Au grating surface lattice resonance position and the strain applied on PDMS substrate. Black dots are experiment data; red line stands for the linear fit for the experiment results (adjusted R-square: 0.98).

5-4 Conclusions

In conclusion, we introduce a direct electron beam lithography method for fabrication of Au gratings on a PDMS substrate. It is fast and convenient for fabrication of nanostructures of different materials from dielectric to metallic. The mechanical tunability of the Au grating pitch on the PDMS substrate is largely enhanced via our designed "sandwich" structures. Benefiting from this design, the narrow line-width, high-amplitude surface lattice resonance of the Au grating is linearly tuned at a rate of 3 nm per 1% strain in the near IR range. The sharp and strong surface lattice resonances are excellent for ultra-sensitive detection of strain on PDMS and are promising for optical sensors of other physical quantities as well.

5-5 References

(1) Soukoulis, C. M.; Wegener, M. Past Achievements and Future Challenges in the Development of Three-Dimensional Photonic Metamaterials. *Nat. Photonics* **2011**, *5*, 523–530.

(2) Shalaev, V. M. Optical Negative-Index Metamaterials. *Nat. Photonics* **2007**, *1*, 41–48.

(3) Zheludev, N. I.; Kivshar, Y. S. From Metamaterials to Metadevices. *Nat. Mater.* **2012**, *11*, 917–924.

(4) Adato, R.; Yanik, A. a; Amsden, J. J.; Kaplan, D. L.; Omenetto, F. G.; Hong, M.

K.; Erramilli, S.; Altug, H. Ultra-Sensitive Vibrational Spectroscopy of Protein Monolayers with Plasmonic Nanoantenna Arrays. *Proc. Natl. Acad. Sci. U. S. A.* **2009**, *106*, 19227–19232.

(5) Stewart, M. E.; Anderton, C. R.; Thompson, L. B.; Maria, J.; Gray, S. K.; Rogers, J. a.; Nuzzo, R. G. Nanostructured Plasmonic Sensors. *Chem. Rev.* **2008**, *108*, 494–521.

(6) Lu, H.; Liu, X.; Mao, D.; Wang, G. Plasmonic Nanosensor Based on Fano Resonance in Waveguide-Coupled Resonators. *Opt. Lett.* **2012**, *37*, 3780–3782.

(7) Knight, M. W.; Sobhani, H.; Nordlander, P.; Halas, N. J. Photodetection with Active Optical Antennas. *Science* **2011**, *332*, 702–704.

(8) Atwater, H. a; Polman, A. Plasmonics for Improved Photovoltaic Devices. *Nat. Mater.* **2010**, *9*, 865–865.

(9) Bai, W.; Gan, Q.; Song, G.; Chen, L.; Kafafi, Z.; Bartoli, F. Broadband Short-Range Surface Plasmon Structures for Absorption Enhancement in Organic Photovoltaics. *Opt. Express* **2010**, *18*, A620–A630.

(10) Ni, X.; Ishii, S.; Kildishev, A. V; Shalaev, V. M. Ultra-Thin, Planar, Babinet-Inverted Plasmonic Metalenses. *Light Sci. Appl.* **2013**, *2*, e72.

(11) Chen, X.; Huang, L.; Mühlenbernd, H.; Li, G.; Bai, B.; Tan, Q.; Jin, G.; Qiu, C.-W.; Zhang, S.; Zentgraf, T. Dual-Polarity Plasmonic Metalens for Visible Light. *Nat. Commun.* **2012**, *3*, 1198.

(12) Aieta, F.; Genevet, P.; Kats, M. a; Yu, N.; Blanchard, R.; Gaburro, Z.; Capasso, F. Aberration-Free Ultrathin Flat Lenses and Axicons at Telecom Wavelengths Based on Plasmonic Metasurfaces. *Nano Lett.* **2012**, *12*, 4932–4936.

(13) Zhao, Y.; Aluì, A. Tailoring the Dispersion of Plasmonic Nanorods to Realize Broadband Optical Meta-Waveplates. *Nano Lett.* **2013**.

(14) Yu, N.; Aieta, F.; Genevet, P.; Kats, M. a; Gaburro, Z.; Capasso, F. A Broadband, Background-Free Quarter-Wave Plate Based on Plasmonic Metasurfaces. *Nano Lett.* **2012**, *12*, 6328–6333.

(15) Ellenbogen, T.; Seo, K.; Crozier, K. B. Chromatic Plasmonic Polarizers for Active Visible Color Filtering and Polarimetry. *Nano Lett.* **2012**, *12*, 1026–1031.

(16) Jiang, Z. H.; Lin, L.; Ma, D.; Yun, S.; Werner, D. H.; Liu, Z.; Mayer, T. S. Broadband and Wide Field-of-View Plasmonic Metasurface-Enabled Waveplates. *Sci. Rep.* **2014**, *4*, 7511.

(17) Huang, L.; Chen, X.; Mühlenbernd, H.; Zhang, H.; Chen, S.; Bai, B.; Tan, Q.; Jin, G.; Cheah, K.-W.; Qiu, C.-W.; *et al.* Three-Dimensional Optical Holography Using a Plasmonic Metasurface. *Nat. Commun.* **2013**, *4*, 2808.

(18) Gutruf, P.; Zou, C.; Withayachumnankul, W.; Bhaskaran, M.; Sriram, S.; Fumeaux, C. Mechanically Tunable Dielectric Resonator Metasurfaces at Visible Frequencies. *ACS Nano* **2016**, *10*, 133–141.

(19) Ee, H.-S.; Agarwal, R. Tunable Metasurface and Flat Optical Zoom Lens on a

Stretchable Substrate. *Nano Lett.* **2016**, *16*, 2818–2823.

(20) Pryce, I. M.; Aydin, K.; Kelaita, Y. A.; Briggs, R. M.; Atwater, H. A. Highly Strained Compliant Optical Metamaterials with Large Frequency Tunability. *Nano Lett.* **2010**, *10*, 4222–4227.

(21) Seo, M.; Kyoung, J.; Park, H.; Koo, S.; Kim, H. S.; Bernien, H.; Kim, B. J.; Choe, J. H.; Ahn, Y. H.; Kim, H. T.; *et al.* Active Terahertz Nanoantennas Based on VO2 Phase Transition. *Nano Lett.* **2010**, *10*, 2064–2068.

(22) Park, J.; Kang, J.-H.; Kim, S. J.; Liu, X.; Brongersma, M. L. Dynamic Reflection Phase and Polarization Control in Metasurfaces. *Nano Lett.* **2017**, *17*, 407–413.

(23) Huang, F.; Baumberg, J. J. Actively Tuned Plasmons on Elastomerically Driven Au Nanoparticle Dimers. *Nano Lett.* **2010**, *10*, 1787–1792.

(24) Zhou, W.; Odom, T. W. Tunable Subradiant Lattice Plasmons by out-of-Plane Dipolar Interactions. *Nat. Nanotechnol.* **2011**, *6*, 423–427.

(25) Zou, S.; Janel, N.; Schatz, G. C. Silver Nanoparticle Array Structures That Produce Remarkably Narrow Plasmon Lineshapes. *J. Chem. Phys.* **2004**, *120*, 10871–10875.

(26) Liu, W.; Lee, B.; Naylor, C. H.; Ee, H.-S.; Park, J.; Johnson, A. T. C.; Agarwal, R. Strong Exciton–Plasmon Coupling in MoS 2 Coupled with Plasmonic Lattice. *Nano Lett.* **2016**, *16*, 1262–1269.

(27) Christ, a; Tikhodeev, S. G.; Gippius, N. a; Kuhl, J.; Giessen, H. Waveguide-

Plasmon Polaritons: Strong Coupling of Photonic and Electronic Resonances in a Metallic Photonic Crystal Slab. *Phys. Rev. Lett.* **2003**, *91*, 183901.

(28) Väkeväinen, A. I.; Moerland, R. J.; Rekola, H. T.; Eskelinen, P.; Martikainen, J.; Kim, D.; Torma, P. Plasmonic Surface Lattice Resonances at the Strong Coupling Regime Plasmonic Surface Lattice Resonances at the Strong Coupling Regime. **2013**.

(29) Yoo, D.; Johnson, T. W.; Cherukulappurath, S.; Norris, D. J.; Oh, S.-H. Template-Stripped Tunable Plasmonic Devices on Stretchable and Rollable Substrates. *ACS Nano* **2015**, *9*, 10647–10654.

(30) Aksu, S.; Yanik, A. a; Adato, R.; Artar, A.; Huang, M.; Altug, H. High-Throughput Nanofabrication of Infrared Plasmonic Nanoantenna Arrays for Vibrational Nanospectroscopy. *Nano Lett.* **2010**, *10*, 2511–2518.

Chapter 6 Future works and conclusions

6-1 Future works

6-1-1 Absorption measurement for colloidal Au nanocrystals

From the permittivity of the colloidal Au nanocrystal solids, we can theoretically calculate the absorption spectrum of colloidal Au nanocrystal thin films of different permittivity and thickness. It is important because high-absorption and heat-generating materials are needed for sensors and bioengineering applications.[8,9] For example, thin films of Au have been used for photo-thermal conversions to accelerate the polymerase chain reaction rate [Figure 6-1]. We can also experimentally measure the absorption of the colloidal Au nanocrystal thin films by measuring the transmittance and reflectance and use the equation: Absorption (%) = 1 – Transmittance (%) – Reflectance (%) to calculate the absorption,[8] and compare it with the theoretical results.

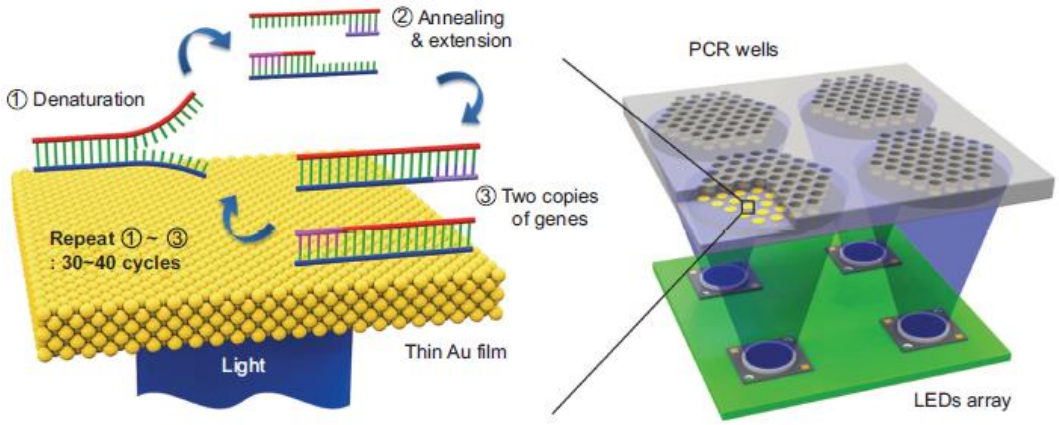

Figure 6-1 Schematics of the ultrafast photonic polymerase chain (PCR) reaction using thin evaporated Au film as a light-to-heat converter and excitation light from the LEDs [Reprinted with permission from: *Light Sci. Appl.* **2015**, *4*, e280].[8]

Besides Au films, Au nanorod arrays or the inverse, a nanoslot nanorod array, are designed to create strong absorbances at desired wavelength [Figure 6-2]. It is very interesting to apply the partially ligand-exchanged Au nanocrystal solids to such nanorod arrays to enhance absorption for devices such as photodetectors, sensors or for other light-to-heat applications. For example, design Au nanorod array that has strong absorbance at certain wavelengths.

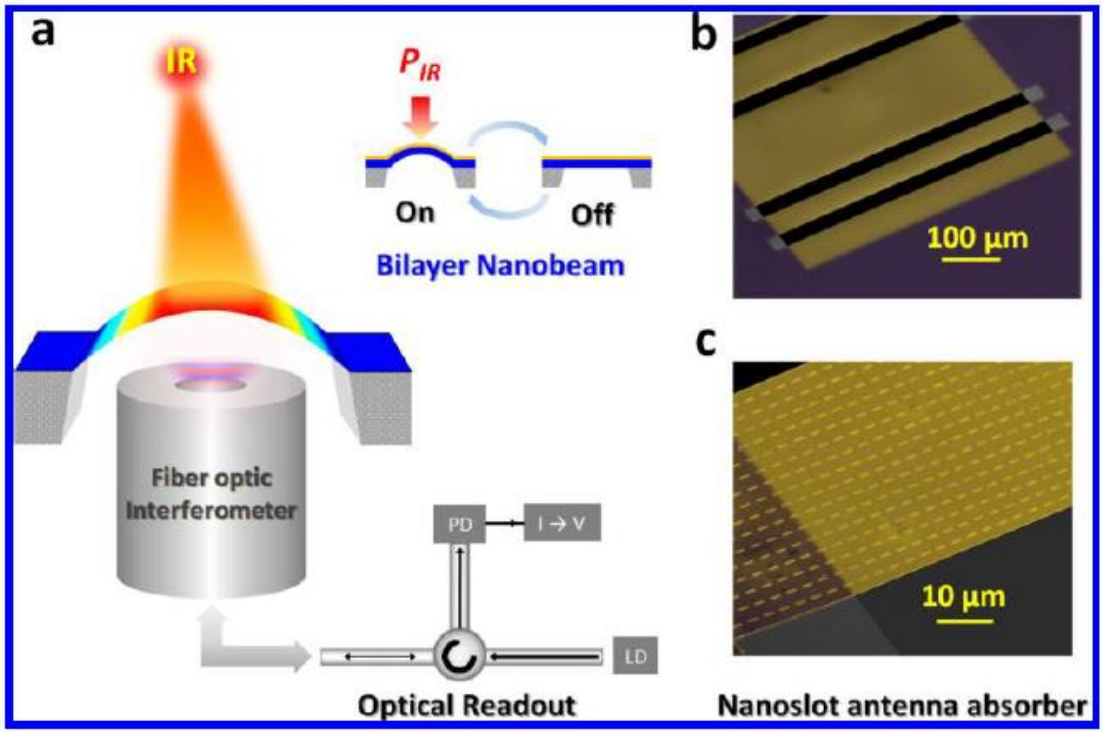

Figure 6-2 Schematics for a plasma-thermomechanical IR detector. (a) The Au nanoslot nanorod array is fabricated on a silicon nitride layer to form a bilayer film. The bilayer film is one of the two reflectors in the fiber optic Fabry-Perot interferometer (FFPI) system. The IR incident light being absorbed by the Au nanoslot nanorod array increases the temperature of the bilayer film, and cause it to bend, which is then be read out by the FFPI system. SEM images for the bilayer film (b) and nanoslot nanorod array (c) [Reprinted with permission from: *Nano Lett.* **2013**, *13*, 1638–1643].[9]

6-1-2 Functional metasurfaces based on colloidal NCs and multifunctional binary NC building blocks

We demonstrated ultrathin metasurface quarter wave-plate based on colloidal Au nanocrystal building blocks. Besides quarter wave-plates, there are many other functional metasurfaces [Figure 6-1] that can take advantage of the large-area, colloidal nanocrystal based fabrication method, such as metasurface polarizers,[1] optical resonator interfaces,[2] metalenses,[3,4] and holography plates.[5,6] An example of the design of a bipolar plasmonic lens is shown in Figure 6-3.

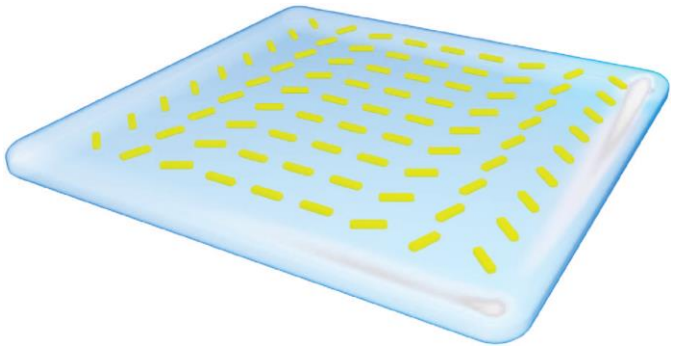

Figure 6-3 Diagram of the bipolar plasmonic lens [Reprinted with permission from *Nat. Commun.* **2012**, *3*, 1198].[3]

Another advantage of colloidal nanocrystal building blocks is that it can be composed of mixutures of nanocrystals which possess functionalities that are different from bulk materials. For example, the mixtures of magnetic and plasmonic nanocrystals

possess superparamagnetism, while bulk ones have ferromagnetism [Figure 6-2].[7] Since applying magnetic field can align magnetic dipoles in certain directions and induces the attractive forces between nanostructures, it would be interesting to fabricate metasurface composed of mixture of nanocrystals on flexible substrate and use the magnetic fields to actively tune its optical responses in amplitude or frequency.

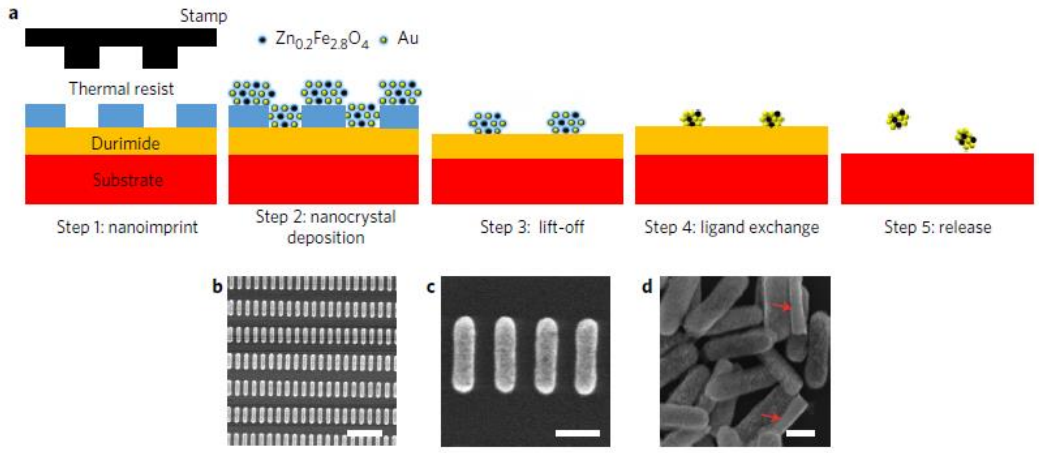

Figure 6-4 Fabrication of hybrid nanorods [Reprinted with permission from *Nat. Nanotechnol.* **2016**, *12*, 228–232].[7]

6-1-3 Oligomers on PDMS substrate

We have demonstrated plasmonic Au nanorods and gratings and photonic Ge and SiO_2 nanodots on PDMS substrates. It would be interesting to consider nanocrystal-based structures on PDMS substrates. Nanocrystals have the unique advantage of self-assembling with interparticle spacing controlled by ligands or shell structures and can be

as small as several nanometers.[10] Taking advantage of our direct electron beam lithography process to pattern plasmonic nanostructures on PDMS, it is possible to assemble complex nanocrystal oligomers on PDMS substrate based on previously reported methods,[11] and study the active optical response of the oligomers to different strain and thus different interparticle spacing.

6-1-4 Multifunctional hydrogel-plasmonic Au nanorod sensors

We demonstrated optical moisture sensors for soil wetness monitoring in agriculture by combining highly hydrophilic hydrogel and plasmonic Au nanorod array. In the future, it is interesting to explore optical sensors integrated with hydrogels of different functional components that are responsive to pH, temperature, minerals and pathogens for agriculture purposes. Integrating multiple functions in one hydrogel-plasmonic Au nanorod array sensor would largely decrease the monitoring cost and improve the efficiency.

6-2 Concluding remarks

The goal of this thesis is to understand and design the optical response of colloidal Au NC materials as building blocks for metamaterials, develop large-area, colloidal Au NC solution-based fabrication methods for nanostructures and metasurfaces, and

integrate metasurfaces with reconfigurable polymers for novel optical sensing applications.

In chapter 2, we design and study the permittivity of colloidal Au nanocrystal solids by tuning the interparticle distance. Two ligands of different lengths are used to cap the colloidal Au nanocrystal solids. By controlling the ratio of the two ligands, the interparticle distance is tuned from 0 to 20 Angstroms, resulting in a continuous variation of permittivity from that characteristic of a metal to that of a dielectric material. Colloidal Au nanocrystal solids with large imaginary permittivity are found, which are promising for high-absorption applications.

In chapter 3, we develop a low-cost, large-area fabrication process using solution-based nanoimprinting and compact ligand exchange of colloidal Au nanocrystals to define anisotropic, subwavelength, plasmonic nanoinclusions for optical metasurfaces. We fabricate metasurfaces from rod-shaped nanoantennas tailored in size and spacing to demonstrate Au nanocrystal-based quarter-wave plates that operate with extreme bandwidths. This fabrication technique can also be applied to other metasurfaces to increase device area and reduce cost.

In chapter 4, we aimed to solve the real world problem of water scarcity, by fabricating plasmonic nanorod moisture sensors for large-area soil moisture monitoring. With the integration of plasmonic nanorod arrays and hydrophilic hydrogels, we report a low-cost, unpowered and environmentally-friendly optical moisture sensor. It operates by transducing refractive index changes of the hydrogel upon exposure to moisture into

spectral shifts. We engineer the dimensions of the nanorods and the thickness of the hydrogel film, to achieve a strong, moisture-sensitive, reflectance signal and fast recovery time. The hydrogel-plasmonic nanorod provides a good platform for detection of different species including pH, ions, temperature, and pathogen.

In chapter 5, we integrate another reconfigurable polymer, PDMS, with Au gratings for mechanically-tunable plasmonic devices. Hybridized, sharp resonance peaks and large grating pitch tunability are demonstrated. Besides, our technique of direct electron beam lithography patterning on PDMS opens up an easy way to fabricate nanostructures based on different types of materials.

Chapter 6 introduces future work including the absorption measurement of partially ligand-exchanged Au NC solids, applying large-area, Au NC solution-based fabrication method to a few more metasurface designs, integrating more functioning polymers into our hydrogel-covered plasmonic Au nanorod array system, and applying our nanostructure-PDMS system for oligomer studies.

I hope this thesis will provide the understanding of the optical properties of plasmonic materials, possible ways for large-area, low-cost, nanoscale structure fabrication, and insight into developing reconfigurable plasmonic systems for sensor applications.

6-3 References

(1) Ellenbogen, T.; Seo, K.; Crozier, K. B. *Nano Lett.* **2012**, *12*, 1026–1031.

(2) Huang, L.; Chen, X.; Mühlenbernd, H.; Li, G.; Bai, B.; Tan, Q.; Jin, G.; Zentgraf, T.; Zhang, S. *Nano Lett.* **2012**.

(3) Chen, X.; Huang, L.; Mühlenbernd, H.; Li, G.; Bai, B.; Tan, Q.; Jin, G.; Qiu, C.-W.; Zhang, S.; Zentgraf, T. *Nat. Commun.* **2012**, *3*, 1198.

(4) Aieta, F.; Genevet, P.; Kats, M. a; Yu, N.; Blanchard, R.; Gaburro, Z.; Capasso, F. *Nano Lett.* **2012**, *12*, 4932–4936.

(5) Huang, L.; Chen, X.; Mühlenbernd, H.; Zhang, H.; Chen, S.; Bai, B.; Tan, Q.; Jin, G.; Cheah, K.-W.; Qiu, C.-W.; Li, J.; Zentgraf, T.; Zhang, S. *Nat. Commun.* **2013**, *4*, 2808.

(6) Ni, X.; Kildishev, A. V.; Shalaev, V. M. *Nat. Commun.* **2013**, *4*, 1–6.

(7) Zhang, M.; Magagnosc, D. J.; Liberal, I.; Yu, Y.; Yun, H.; Yang, H.; Wu, Y.; Guo, J.; Chen, W.; Shin, Y. J.; Stein, A.; Kikkawa, J. M.; Engheta, N.; Gianola, D. S.; Murray, C. B.; Kagan, C. R. *Nat. Nanotechnol.* **2016**, *12*, 228–232.

(8) Son, J. H.; Cho, B.; Hong, S.; Lee, S. H.; Hoxha, O.; Haack, A. J.; Lee, L. P. *Light Sci. Appl.* **2015**, *4*, e280.

(9) Yi, F.; Zhu, H.; Reed, J. C.; Cubukcu, E. *Nano Lett.* **2013**, *13*, 1638–1643.

(10) Fan, J. A.; Wu, C.; Bao, K.; Bao, J.; Bardhan, R.; Halas, N. J.; Manoharan, V. N.; Nordlander, P.; Shvets, G.; Capasso, F. *Science* **2010**, *328*, 1135–1138.

(11) Greybush, N. J.; Liberal, I.; Malassis, L.; Kikkawa, J. M.; Engheta, N.; Murray, C.

B.; Kagan, C. R. *ACS Nano* **2017**, *11*, 2917–2927.